UNIVERSIDADE ESTADUAL DE CAMPINAS
Instituto de Física Gleb Wataghin (IFGW)

Fernando Henrique de Sá

Estudo de Impedâncias e Instabilidades Coletivas aplicadas ao Sirius.

Study of Impedances and Collective Instabilities applied to Sirius.

Campinas

2018

Fernando Henrique de Sá

Estudo de Impedâncias e Instabilidades Coletivas aplicadas ao Sirius.

Tese apresentada ao Instituto de Física Gleb Wataghin (IFGW) da Universidade Estadual de Campinas (UNICAMP) como parte dos requisitos exigidos para a obtenção do título de Doutor em Física, com ênfase em Física de Aceleradores.

Orientador: Prof. Dr. Antônio Rubens Britto de Castro

Co-orientador: Prof. Dr. Silvio Antonio Sachetto Vitiello

Este exemplar corresponde à versão final da tese defendida pelo aluno Fernando Henrique de Sá, e orientada pelo Prof. Dr. Antônio Rubens Britto de Castro

Campinas

2018

Inclua aqui o pdf com a ficha catalográfica fornecida pela BAE.

Inclua aqui a folha de assinaturas.

Dedico esta tese à todo mundo que tiver paciência para lê-la.

ACKNOWLEDGEMENTS

Lorem ipsum dolor sit amet, consectetuer adipiscing elit. Ut purus elit, vestibulum ut, placerat ac, adipiscing vitae, felis. Curabitur dictum gravida mauris. Nam arcu libero, nonummy eget, consectetuer id, vulputate a, magna. Donec vehicula augue eu neque. Pellentesque habitant morbi tristique senectus et netus et malesuada fames ac turpis egestas. Mauris ut leo. Cras viverra metus rhoncus sem. Nulla et lectus vestibulum urna fringilla ultrices. Phasellus eu tellus sit amet tortor gravida placerat. Integer sapien est, iaculis in, pretium quis, viverra ac, nunc. Praesent eget sem vel leo ultrices bibendum. Aenean faucibus. Morbi dolor nulla, malesuada eu, pulvinar at, mollis ac, nulla. Curabitur auctor semper nulla. Donec varius orci eget risus. Duis nibh mi, congue eu, accumsan eleifend, sagittis quis, diam. Duis eget orci sit amet orci dignissim rutrum.

Nam dui ligula, fringilla a, euismod sodales, sollicitudin vel, wisi. Morbi auctor lorem non justo. Nam lacus libero, pretium at, lobortis vitae, ultricies et, tellus. Donec aliquet, tortor sed accumsan bibendum, erat ligula aliquet magna, vitae ornare odio metus a mi. Morbi ac orci et nisl hendrerit mollis. Suspendisse ut massa. Cras nec ante. Pellentesque a nulla. Cum sociis natoque penatibus et magnis dis parturient montes, nascetur ridiculus mus. Aliquam tincidunt urna. Nulla ullamcorper vestibulum turpis. Pellentesque cursus luctus mauris.

Nulla malesuada porttitor diam. Donec felis erat, congue non, volutpat at, tincidunt tristique, libero. Vivamus viverra fermentum felis. Donec nonummy pellentesque ante. Phasellus adipiscing semper elit. Proin fermentum massa ac quam. Sed diam turpis, molestie vitae, placerat a, molestie nec, leo. Maecenas lacinia. Nam ipsum ligula, eleifend at, accumsan nec, suscipit a, ipsum. Morbi blandit ligula feugiat magna. Nunc eleifend consequat lorem. Sed lacinia nulla vitae enim. Pellentesque tincidunt purus vel magna. Integer non enim. Praesent euismod nunc eu purus. Donec bibendum quam in tellus. Nullam cursus pulvinar lectus. Donec et mi. Nam vulputate metus eu enim. Vestibulum pellentesque felis eu massa.

Quisque ullamcorper placerat ipsum. Cras nibh. Morbi vel justo vitae lacus tincidunt ultrices. Lorem ipsum dolor sit amet, consectetuer adipiscing elit. In hac habitasse platea dictumst. Integer tempus convallis augue. Etiam facilisis. Nunc elementum fermentum wisi. Aenean placerat. Ut imperdiet, enim sed gravida sollicitudin, felis odio placerat quam, ac pulvinar elit purus eget enim. Nunc vitae tortor. Proin tempus nibh sit amet nisl. Vivamus quis tortor vitae risus porta vehicula.

"Aqui jazem seis anos da minha vida."
(Fernando Henrique de Sá)

ABSTRACT

Sirius is the new fourth generation synchrotron light source that is being built in Campinas, Brazil, by the Brazilian Synchrotron Light Laboratory (LNLS). With a natural emittance of 250 pm rad, extremely high brightness synchrotron light will be generated by, at most, 18 insertion devices (IDs) installed in the straight sections of the storage ring and by 20 superbends (3.2 T) present in the center of each achromat of the magnetic lattice. The standard vacuum chamber will be round, made of copper, with a radius of 12 mm, which is small compared to third generation light sources chambers, and the first IDs planned will be out of vacuum and will have a very reduced gap, with chambers as small as 2.4 and 3.0 mm, in most cases. Additionaly, the vacuum system will be distributed, through the use of NEG coating in the inner part of the chambers in the whole ring. All these factors intensify the impedance related effects of the machine, which can generate coherent oscillations, compromizing the quality of the light, cause total or partial beam loss and influence the equilibrium dynamics of the electrons. In this work some of the main components of the vacuum chamber were modelled and their wake fields were calculated with semi-analytical and numerical methods and added to the total impedance budget of the machine. With the application of this model to the first phase of operation, it was found that the beam will suffer from transverse coupled bunch resistive wall instability, making it necessary the installation of transverse bunch-by-bunch feedback systems in both planes. It was also predicted stability without feedback action if the ring operates with chromaticity larger than 2.8 in both planes. It was also found that the tune-shifts caused by quadrupolar impedances from the IDs are not negligible and the operation point of the machine will have to be changed as function of the total stored current. The thresholds for intra-bunch instabilities are much above the nominal operation current and will not be a problem in any of the three planes and there will be no longitudinal coupled-bunch motion as long as the ring operates with superconducting RF cavities. The installation of a Landau cavity is planned for the phase two of operation, which will allow higher total current in the machine and even high single-bunch current in the middle of the train. Even though it was not done any calculations for these conditions, the methods and codes developed in this work can be directly applied for those cases.

Keywords: Sirius; impedances; instabilities.

Resumo

Sirius é a nova fonte de luz síncrotron de quarta geração que está sendo construída em Campinas, Brasil, pelo Laboratório Nacional de Luz Síncrotron (LNLS). Com uma emitância natural de 250 pm rad, radiação síncrotron de altíssimo brilho poderá ser gerada por até 18 dispositivos de inserção (DI) instalados nos trechos retos do anel de armazenamento e por 20 dipolos de alto campo (3.2 T) presentes no centro de cada arco acromático da rede magnética. A câmara de vácuo padrão do anel será cilíndrica, feita de cobre e terá 12 mm de raio, que é um valor pequeno comparado com as câmaras de fontes de luz síncrotron de terceira geração, e os primeiros DIs previstos serão fora do vácuo e terão uma abertura bastante reduzida, com câmaras de apenas 2.4 e 3.0 mm de raio, na maioria dos casos. Adicionalmente, o sistema de vácuo do anel será distribuido, através da superposição de NEG na superfície interna das câmaras ao longo de todo o anel. Todos esses fatores intensificam os campos de arraste, ou impedâncias, da máquina, que podem gerar oscilações coerentes, deteriorando a qualidade da luz gerada, e causar perda total ou parcial do feixe, além de influenciar na dinâmica de equilíbrio do elétrons. Neste trabalho alguns dos principais componentes da câmara de vácuo foram modelados e seus campos de arraste calculados por meios semi-analíticos e numéricos e adicionados ao modelo total de impedância do anel. Com a aplicação de tal modelo para a primeira fase de operação, constatou-se que o feixe será instável nos planos transverais devido à oscilações causadas por acoplamento entre pacotes gerados pela impedância de parede resistiva, tornando necessária a instalação de sistemas de retroalimentação pacote por pacote para manter a estabilidade. Também foi previsto que o feixe ficará estável se o anel for operado com uma cromaticidade nominal de 2.8 em ambos os planos transversais. Constatou-se ainda que as mudanças de sintonia causadas por impedâncias quadrupolares dos DIs serão significativas, e o ponto de operação da máquina deverá ser mudado em função da corrente total. Os limiares das instabilidades relacionadas a oscilações intra-pacote estão muito acima da corrente nominal de operação e não serão um problema e não há previsão de instabilidades longitudinais de acoplamento entre pacotes, haja vista que a máquina operará com cavidades de RF supercondutoras. Na segunda fase de operação está prevista a instalação de uma cavidade Landau, que permitirá operação com corrente total mais alta, inclusive com pacotes bastante intensos no meio do trem. Apesar de não terem sido feitos cálculos para esse tipo de operação, os principais métodos e códigos desenvolvidos nesse trabalho podem ser diretamente usados para tal fim.

Palavras-chaves: Sirius; impedâncias; instabilidades.

LIST OF FIGURES

LIST OF TABLES

CONTENTS

1 INTRODUCTION

In scientific facilities commonly known as Synchrotron Light Source (SLS) the interaction between light and matter is used to study properties of a variaty of materials. Through techniques envolving absortion, reflection, refraction and scattering of light of different 'colors' by the materials under study, their atomic structure, composition and chemical activity can be determined.

The frequency of the light used in these facilities ranges from tera-hertz to hard X-rays and its origin is always related to synchrotron emission of radiation by charged particles, hence the name of the facility. The light emitted by centripetal acceleration of ultra-relativistic particles has unique properties for use in scientific investigation: broad spectrum, high total flux and the strong collimation are among them.

1.1 Types of Light Sources

In general we can separate the SLS in two groups, depending on the topology of the accelerators involved: linear and circular. In the linear sources, denominated X-Ray Free Electron Lasers (FEL), it is possible to excite the beam to emit light coherently, hence the name of these facilities. There are several techniques to achieve this and their enumeration or explanation is beyond the scope of this work and a complete review is given by Pellegrini (2016), the idealizer of these machines, and also by McNeil & Thompson (2010). The important fact is that besides the high level of coherence of the light in these facilities, the intensity of the photon beam is increased by orders of magnitude with these techniques because it becomes proportional to the square of the number of particles in the beam, instead of the linear dependency of other sources. The excitation of coherent emission becomes increasingly difficult as the energy of the photons increase, because ever smaller errors in the fields or decoherences in the electron beam destroy the cascade of the stimulated emission. This task is so difficult that only in the last decade coherent X-rays were successfully generated and this achievement represented a revolution in the synchrotron radiation community, opening up exciting new possibilities for scientific research, for example, in cristallography as pointed out by Johansson *et al.* (2017), in molelucar imaging, according to Barty *et al.* (2013), including the possibility of single molecules imaging (BARTY, 2016), in structural biology (MARX, 2017), and some other unique analysis such as the process of liquid explosion induced by the X-Ray pulse, as described by Stan *et al.* (2016).

Among the several types of circular accelerators we highlight the ones based on synchrotron storage rings. There is an abuse of use of the word synchrotron here, so far it meant the nature of emission of the light in these facilities, but when used to describe this type of accelerator it is related to the synchronicity of the revolution time of the electrons with the electromagnetic field that drives their motion, which is the main mechanism behind the operation of these machines. In this type of SLS the electrons are grouped in several bunches that fill the whole storage ring and are confined for hours in close to circular orbits by deflecting and focusing magnetostatic fields. The radiation used in experiments can be generated by the same fields that deflect the beam (dipoles) or by special devices called Insertion Devices (IDs) that are put in empty sections of the ring, called straight sections.

While the experiments in FEL are performed with only one strong single pulse of radiation that can be generated at a repetition rate of a few hundreads of Hertz, in storage rings the emitted light continuously hit the samples under study and the interaction patterns are recorded for as long as needed to achieve the desired resolution for the experiment. Besides, while in FEL it is only possible to have one beamline operating, in storage rings dozens of them can work simultaneously, performing completely different experiments.

Figure 1 shows a generic example of a storage ring based light source. It has three main subsystems: an injector, the storage ring and the beamlines. The injector is the responsible of generating and accelerating the particles up to the energy of the storage ring and in most light sources it is composed of a gun, a LINAC and a booster synchrotron. In the case of electron storage rings the gun extract the electrons from metals, via thermoionic or photoelectric effect, and guide them to the LINAC where they are compressed in bunches and accelerated, generally up to energies of hundreads of MeV. After this, the electrons are transported to the booster synchrotron where they

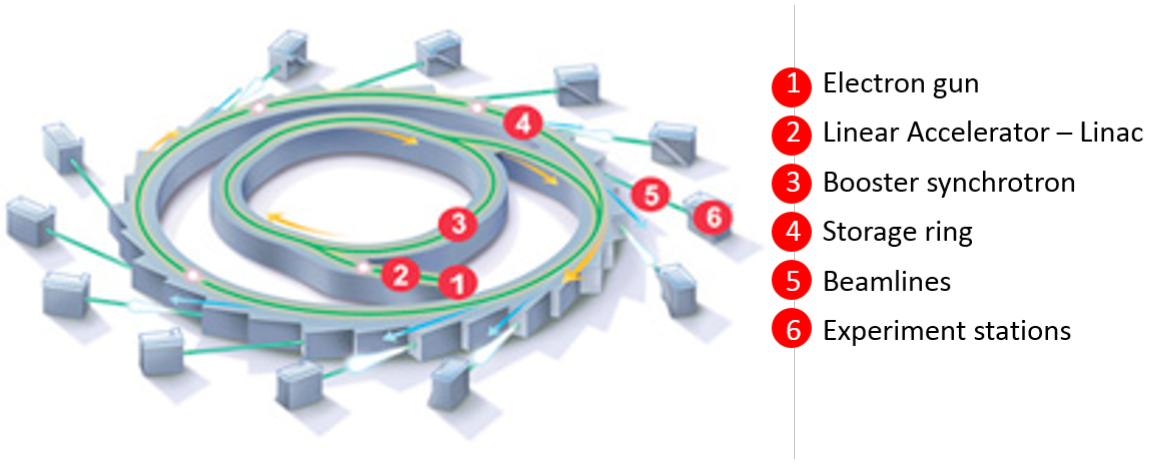

Figure 1 – Schematic of a storage ring based light source. Notice the three main systems: the injection systems, composed of an electron gun, a Linear Accelerator (LINAC) and a booster; the storage ring and the beamlines, with the experiment stations at their end.

are accelerated up to the energy of the storage ring, generally a few GeV, and extracted from it to be injected in the storage ring. In modern light sources this whole process can happen with a repetition rate of a few Hz.

The storage ring is a synchrotron just like the booster that, instead of accelerating the electrons, keeps their average energy fixed while they perform dozens of billions of turns in the few hours they remain there. After the injection, the bunch of electrons oscillate around the ideal orbit of the storage ring, but in a few dozens of thousands of turns they are damped, reaching the storage ring equilibrium values of transverse emittances (size and divergence), longitudinal length and energy spread. In ideal storage rings they stay stable in stationary closed orbits emitting radiation that is collected by the beamlines. The radiation exits the storage ring through holes in the external part of the vacuum chamber and propagate through the beamline in straight trajectories, tangent to the electrons orbit in the point where it was generated. Among all the elements in the beamlines, we highlight the monochromators, used to select a narrow energy bandwidth of the radiation, and the mirrors, which deflect and focus the photon beam to the samples, located at the end of the beamline, together with a complex apparatus to support it and measure its interaction data.

1.2 Storage Ring Main Devices

This work will focus on the study of the dynamics of the particles while they are in their equilibrium regime inside the storage ring, without considering the details of the injection process. For this reason, in this subsection we will present the main subsystems of a storage ring and discuss on their main contributions to the task of keeping particles confined for such long times.

1.2.1 Magnetic Lattice

The magnetic lattice is the name of the series of static magnets that are placed along the beam trajectory that deflect and focus it to keep it circulating the ring. It is composed of a reduced number of different types of magnets that have specific functions for the beam confinement:

Dipoles: or bending magnets are the devices responsible for deflecting the beam in such a way that its net deflection in one turn is 2π rad. They generate an almost constant vertical field, B_y, along the beam path that curves its horizontal trajectory and keeps the vertical unchanged, see Figure 2. At each point of the trajectory inside a dipole the curvature, $G(s)$, is given by:

$$G(s) = \frac{1}{\rho(s)} = \frac{e}{p_0} B_y(s) \approx \frac{ec}{E_0} B_y(s) \tag{1.1}$$

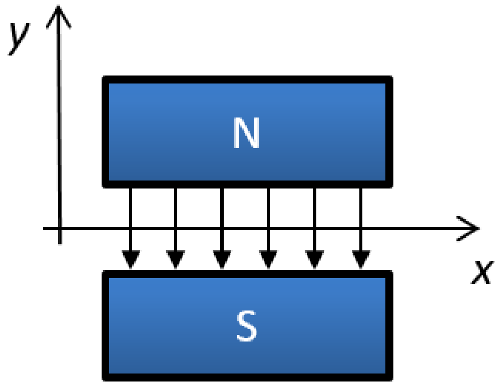

(a) Schematic figure of a dipole magnet, where N and S indicate the North and South poles of the magnet and the vertical down arrows indicate the magnetic field lines

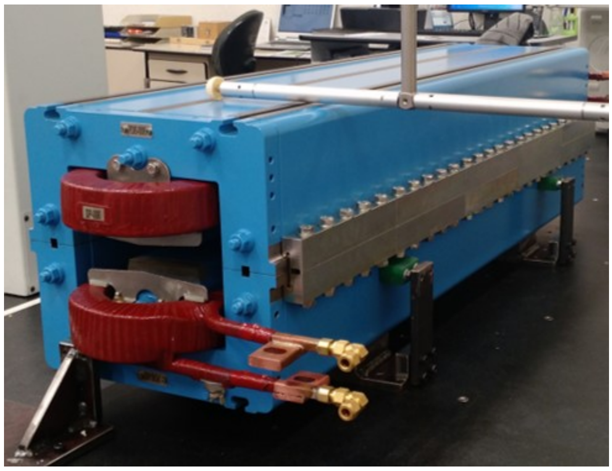

(b) Picture of a real dipole magnet.

Figure 2 – Ilustrations of a dipole magnet.

where s is the longitudinal position along the ring, $\rho(s)$ is the radius of curvature, e is the absolute value of the particle's charge, c is the speed of light, p_0 is the absolute value of the average linear momentum of the beam and E_0 is the average beam energy. Notice in the equation above that dipoles work as spectrometers, if the beam has an energy spread, particles with higher/lower energy will spiral out/in because their total deflection angle will be different than 2π rad, which means eventually all particles will hit the vacuum chamber and be lost;

Quadrupoles: are responsible to focus the beam, keeping the particles that are not in the ideal orbit oscillating around it. They achieve this by creating a field that grows linearly in intensity with the displacement from its center (see Figure 3), in such a way that they work as lenses. They are characterized by their strength, defined by:

$$K(s) = \frac{e}{p_0} \left.\frac{\partial B_y}{\partial x}\right|_{y=0} (s) \tag{1.2}$$

where x is the horizontal displacement from the center of the quadrupole and y is the vertical. The strength defined above is directly related to how much the quadrupole deflect off-centered particles, being its integral along the quadrupole length directly related to the focal distance of the magnet. One intrinsic limitation of quadrupoles imposed by Maxwell Equations (ME) and the Lorentz force is that they cannot focus the beam simultaneously in the horizontal and vertical directions. This means that in a magnetic lattice it is always needed to have two types of quadrupoles, one to focus in the horizontal, called focusing quadrupoles, and one to focus in the vertical, called defocusing quadrupoles, in such a way that net focusing in both planes can be achieved with intelligent positioning of the magnets. Besides, quadrupoles are

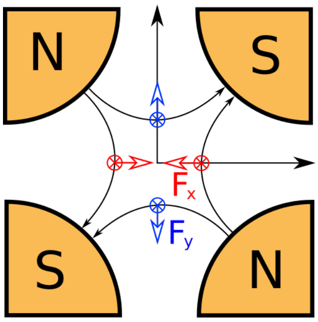

(a) Schematic figure of a quadrupole magnet, where the curved arrows indicate the magnetic field lines and the red/blue arrows indicate the direction of the horizontal/vertical forces felt by an electron entering the sheet. Notice this quadrupole focuses in the horizontal, so it is a focusing quadrupole.

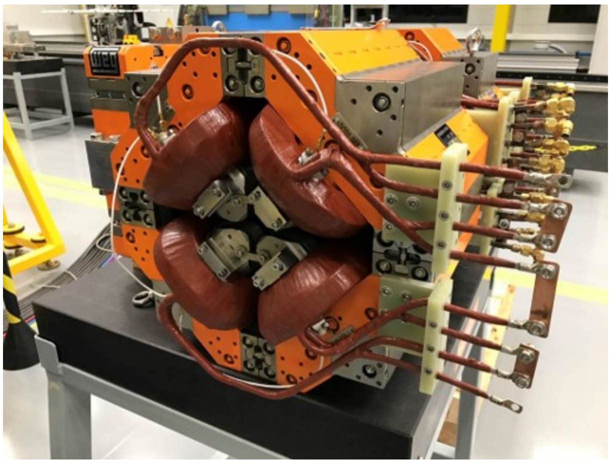

(b) Picture of a real quadrupole magnet, with the coils that generate the magnetic field and the iron core that guide and shape the field lines inside the gap.

Figure 3 – Ilustrations of a quadrupole magnet.

arranged along the ring to correct the intrinsic limitation of the dipoles regarding the energy dispersion, as discussed above, adding/subtracting net deflection in one turn for particles with more/less energy. This causes particles to have different closed orbits depending on their energy, but at least maintains them stable. Quadrupoles and dipoles are the most important multipoles in a storage ring because together they define its main properties, such as the particles average energy, the transverse beam emittance, and beam sizes along the ring, as well as the fundamental frequency of oscillation of the particles, the tune.

Sextupoles: quadrupoles also suffer from chromatic aberrations, focusing more or less the particles depending on their energy. This difference in focusing makes particles oscillate differently around their closed orbit, changing their fundamental resonance frequency. This is not a fundamental problem, but in almost all modern storage rings it is impossible to store particles with only dipoles and quadrupoles. Sextupoles can correct that effect if placed at the right positions along the ring because of their non-linear magnetic field, which grows quadractically with the distance from its center, see Figure 4. Just like quadrupoles, it is needed two types of sextupoles, focusing and defocusing, to correct the horizontal and vertical frequency of oscillation of the particles. Sextupoles are needed, but they introduce several complications for the design of a storage ring, because their non-linear fields introduce chaos in some regions of the particles phase space. More sextupoles or higher order multipoles can be introduced to avoid chaos as much as possible and also to help correcting higher order chromatic effects.

Higher order multipoles, such as octupoles and decapoles, can be used to correct

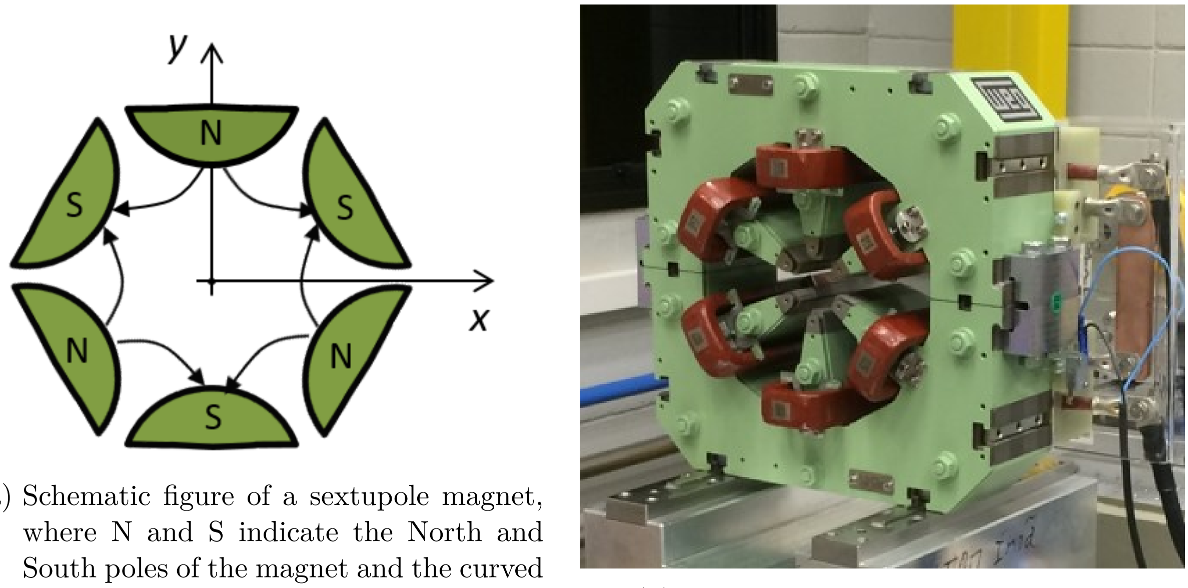

(a) Schematic figure of a sextupole magnet, where N and S indicate the North and South poles of the magnet and the curved arrows indicate the magnetic field lines.

(b) Picture of a real sextupole magnet.

Figure 4 – Ilustrations of a sextupole magnet.

higher order chromatic and geometric aberrations, but their use is not very common in the design of storage ring for light sources as they are in colliders, even though this tendency is changing with the new light sources that are being designed, such as MAX IV (LEEMANN *et al.*, 2009), ESRF upgrade (FARVACQUE *et al.*, 2013), APS-U (SUN; BORLAND, 2013), SLS upgrade (SOUTOME *et al.*, 2016) and Spring-8 upgrade (SOUTOME *et al.*, 2016). Nevertheless, they are always present in storage ring as errors of the main magnets and their effect must be taken into account in detailed single particle dynamics analysis.

Generally lattices have high periodicity, being the repetition of a unit cell along the whole extension of the ring. This periodicity simplifies the design of the ring, the dynamics of the electrons and reduces the number of dangerous resonances that can harm the beam stability. Unit cells generally can be divided in two parts, an arc section, where are placed the dipoles, intervealed by focusing elements to control the dispersion and focus the beam from one dipole to another, and a straight section, with an empty space for the installation of IDs for light generation and some focusing elements to focus the beam in the center of these empty spaces.

1.2.2 RF Cavity

Each turn the electrons lose energy due to synchrotron radiation which must be replenished periodically in order for them to remain in stable orbits, with energy close to the nominal energy of the storage ring. The magnetostatic components described above cannot perform such a task neither any other component or method relying on static electromagnetic fields of any kind, because according to the ME and the Lorentz force, the liquid energy transfered to a charged particle by static fields in one turn over the ring must be zero. This means that the laws of physics constraint it is necessary to rely on time dependent electromagnetic fields to replenish the energy of the electrons. The way this is accomplished in a storage ring is through the use of devices called RF cavities.

RF cavity is a jargon for a cylindrical electromagnetic cavity with the lowest Transverse Magnetic mode (TM010) in the range of radiofrequency. Cavities for use in storage rings must have at least two small holes in its axis for the beam passage and one other hole to couple the cavity with an external source to feed the mode TM010 with energy. This energy is transfered to the particles in the storage ring through the almost homogeneous longitudinal eletric field of this mode when the particles passes through the cavity. The frequency of this particular mode of the cavity is always exactly equal to a multiple, h, of the revolution frequency of the beam along the ring, in such a way that once initially adjusted, the beam will always enter the cavity when the electric field has a phase that replenish the average energy lost by it in one turn. Besides, this synchronicity mechanism, that, by the way, is the responsible for the name of these machines, creates h points in the ring where it is possible to put a bunch of electrons around it and keep it stable.

1.2.3 Vacuum System

The vacuum system is responsible for creating a compact region around the reference orbit in the whole machine with very low pressure, which minimizes collisions of the stored charged particles with gas molecules and, consequently, increases the average time particles can be stored with stable movement. Quantitatively, the average pressure of a storage ring must be lower than 1 nTorr for the average stored time of the particles to be of the order of a few dozens of hours.

The vacuum system is composed of two main subsystems, the vacuum vessel, which defines the boundaries of the electrons atmosphere with the environment, and vacuum pumps to maintain the desired difference in pressure between the two regions. Most of the extension of the vacuum vessel is composed of straight and long chambers with a specific cross section, constant along the extension of the chamber. They are made of metals due to several desirable properties of these materials, such as high heat and electrical conductivity, maleability, high acceptance to welding and brasing and high resistence to pressure. Among them we highlight implications of the high electrical conductivity, due to its importance for this work. Besides the standard vacuum chamber there are several other structures that compose the vacuum vessel, for example:

Bellows: are sanfonated elements that connect two vacuum chambers in order to accommodate longitudinal thermal expansions and transverse misalignments between them;

Valves: devices that are used to isolate the vacuum in different sections of the ring. Generally they remain opened, creating a single vacuum region along the ring, but can be closed automatically in case of accidents, or manually for maintenance;

Flanges: are the components responsible for coupling two different vacuum components together in a leakage-free way;

Dipole Chambers: are special curved chambers used in the regions where there are dipoles. In some cases they also have exit ports for the photon beam passage at its external side;

Radiation Masks: only a small part of the synchrotron radiation generated in a storage ring exits the ports and are used in the beamlines. Most of it hits the vacuum chamber and is transformed in heat that is absorbed and diffused by it. However, some components are sensitive and must be protected from the radiation, which requires the vacuum chamber to have some obtrusions inside it to create shadows for such elements;

Diagnostic: are components that measure the electromagnetic signal generated by the beam to determine its properties, such as intensity, positions and oscillations. They must be inside the chamber because the high frequency components they measure cannot propagate out the chamber;

Transitions: there are some sections of the vessel that have different cross sections than the standard chamber, generally to accomodate special devices such as RF cavity, IDs or some magnets. Transitions are smooth longitudinal variations of cross section from one chamber to the other.

Notice that these are only some examples of the different components of the vacuum vessel of a storage ring. All these components introduce variations in the inner cross sections of the chamber which interact with the electromagnetic fields of the beam, creating other fields, called wake fields, that causes heating of the components, in addition to the radiation heating, and affects the beam dynamics. The study of this last interaction will be the main subject of this work.

1.3 Light Source Generations

The average brightness is the main figure of merit used to characterize a synchrotron light source (HETTEL, 2014b), the larger its value the better the radiation . It is a measure of the intensity and collimation of the radiation at a given frequency or wavelength and can be mathematically defined by the following expression, according to

Huang (2013):

$$B(\omega) = \frac{1}{\Delta\omega} \frac{F(\omega)}{\Sigma_x(\omega)\Sigma_y(\omega)} \tag{1.3}$$

where ω is the photon frequency, $F(\omega)$ is the flux, Σ_x and Σ_y correspond to the volume the photon beam occupies in the horizontal and vertical phase space, respectively, and $\Delta\omega$ is a frequency bandwidth that is proportional to the central frequency (usually 0.1 %). The volume occupied by the photon beam in phase space is the product of the standard deviations in angle and position of the photons distribution, which is the result of a convolution of the electron beam distribution and the single photon distribution. This last term depends on the radiation frenquency and on how it was generated. On the other side, the volume occupied by the electron beam in phase space is called emittance and it depends only on the storage ring properties.

Notice in equation (1.3) that to increase the brightness of a given light source it is necessary to increase the number of stored electrons, which linearly impacts the total photon flux, and minimize the emittance of the electron beam. Consequently, together with the electrons energy, the emittance and the current are the main figures of merit of a storage ring. New machines always try to push the limit of these factors to obtain gains in synchrotron light quality and, from time to time, new ideas and breakthroughs in accelerators technology create large scale advances.

These descontinuities in the otherwise small and incremental improvements of the radiation quality happened three times along the history of storage ring based light sources, creating four generations of machines. The first breakthrough was the creation of machines specialized in the generation of synchrotron radiation, which marked the difference of the first generation of light sources, which were parasitical to particle colliders, to the second generation. With specially designed machines it was possible to optimize the magnetic lattice to achieve smaller emittances, higher currents and always use light particles, such as electrons, as the source.

The second breakthrough was the construction of machines specialized to operate with IDs, which are special devices that are put along the straight trajectory of the beam and generates a transverse magnetostatic field with an amplitude that varies sinusoidally with respect to the longitudinal direction. When the beam passes through this field it wiggles, and synchrotron emission of radiation happens due to its deflection at each wiggle. The light emitted from successive wiggles interferes in such a way that only photons with specific frequencies survive and the resulting radiation has a spectrum where all the energy is concentrated at very thin peaks around multiples of this resonant frequency. The intensity of these peaks is proportional to the number of particles in the beam and the number of wiggles of the Insertion Device (ID) field and their bandwidth is proportional to the inverse of the number of wiggles, hence these devices are built with the maximum number of periods that are technically possible. Additionally, the polarization of the radiation is defined by the direction of the magnetic field of the ID. For example, if the field is vertical in relation to the ground, the electrons will oscilate horizontally and the radiation will be horizontally polarized. Circular and elliptical polarizations can also be achieved by changing not only the intensity of the field but also its direction as a function of the longitudinal position. In a real ID all these properties of the light can be tuned according to the needs of the experiment to be carried out at the experimental station, which makes this devices a very powerful tool for scientific experiments.

Currently another generation of light sources is rising. With much smaller emittances, these machines are being called difraction limited light sources. This term is used when the emittance of the electrons is smaller than the emittance of the single photon distribution up to a few keV. This way, the convolution of the two is mainly determined by the method the radiation is generated, which in turn is defined by the laws of nature and cannot be further optimized. This search for smaller emittance becomes clear when we observe the graph shown in Figure 5 which compares the 3th and 4th GLS. To interpret this figure it is important to know that the emittance of a storage ring roughly scales

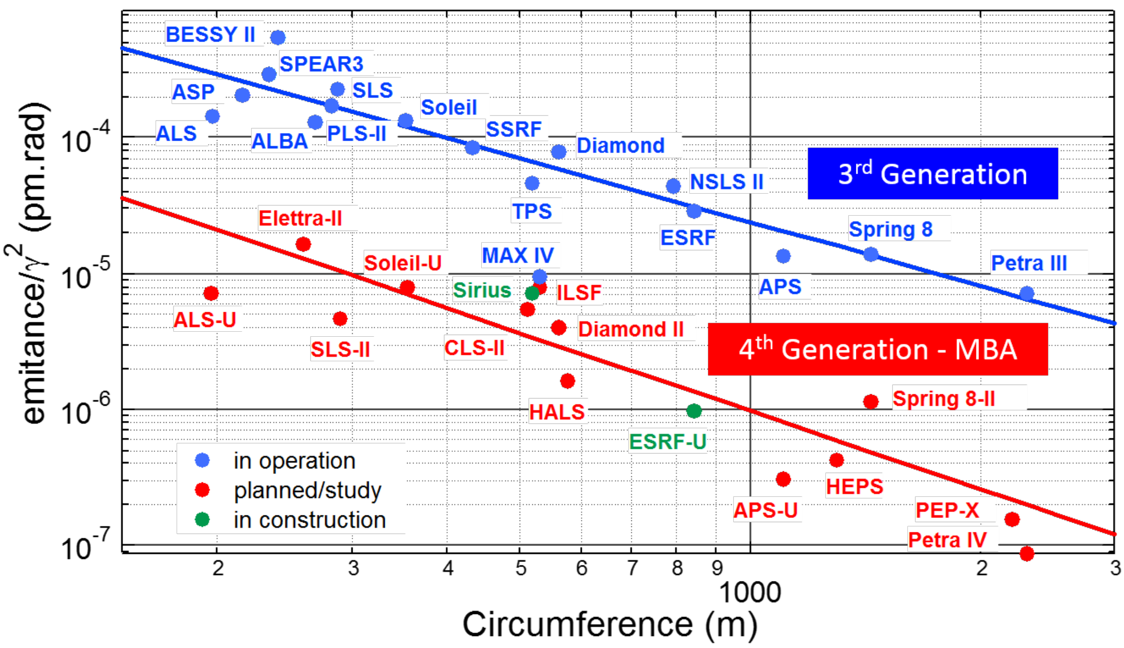

Figure 5 – Natural emittance normalized by relativistic energy square as function of ring circumference for several existing Third Generation Light Sources (3rd GLS) and future Fourth Generation Light Sources (4th GLS). The blue solid line is a fitting among the 3rd GLS and the red solid line is a fitting among the 4th GLS. Notice the only 4th GLS in operation is MAX-IV. Adapted from (LIU; WESTFAHL, 2017).

with, according to Hettel (2014b),

$$\varepsilon \propto \frac{\gamma^2}{N_b^3}, \tag{1.4}$$

where $\gamma = E/m_0c^2$ is the relativistic energy and N_b is the number of dipoles, or bending magnets, of the storage ring. Besides, higher energy storage rings generally imply in larger circumferences and, consequently more dipoles. Given the scaling presented above, it is clear that in general the emittance is reduced with the increase of the ring circumference, as shown by the tendency lines in the figure.

Just like the FEL, the 4$^{\text{th}}$ GLS will enable new science to be made, according to Eriksson *et al.* (2014):"The significant improvement provided by the DLSRs under construction and in the design stage will enlighten our view of the world and allow science which is not possible, or not even thinkable, today.". In section 4 of his article, ERIKSSON *et al.* provides a very good review of the possible scientific studies that will be enabled by such machines. Here we highlight the advances in imaging techniques, such as ptychography (THIBAULT *et al.*, 2014), and diffraction (HITCHCOCK; TONEY, 2014), that will be possible due to the increase in the transverse coherent part of the flux [1].

1.3.1 Multi-Bend-Achromat (MBA)

The main reason for the 4$^{\text{th}}$ GLS to achieve such small emittances is the use of Multi-Bend-Achromat (MBA) lattices. In 3$^{\text{rd}}$ GLS the number of dipoles in one unit cell of the magnetic lattice is two or three depending on the machine, but in 4$^{\text{th}}$ GLS this number is larger than five, hence the name multi-bend. The achromat part of the name MBA is due to the fact that energy dispersion errors introduced by dipoles are corrected locally and do not affect the trajectories and transverse bunch sizes inside the IDs.

Even though this change does not seem to be harmful or difficult in a first analysis, it requires several developments in almost all the areas involved in designing, constructing and operating a light source (ERIKSSON *et al.*, 2014; LIU; WESTFAHL, 2017). The larger number of dipoles in a short space requires strong focusing from the quadrupoles to achieve low emittances. These strong quadrupoles require strong sextupoles to correct their chromatic errors, which, in turn, require other strong sextupoles to increase the stability region around the fixed point of the one turn map (BORLAND *et al.*, 2014). In order to produce all these strong magnets, they need to be closer to the beam, their gap must be smaller (JOHANSSON *et al.*, 2014), which implies the vacuum chambers must be smaller too. The smaller vacuum chamber decreases the vacuum conductance[2], making it necessary to adopt different solutions for vacuum (AL-DMOUR *et al.*, 2014),

[1] For a brief and didactic description of coherence, we recommend the work of Huang (2013).

[2] The vacuum conductance is proportional to the third power of the vacuum chamber radius according to Al-Dmour *et al.* (2014).

generally distributed along the whole ring, such as the use of Non-Evaporable Getter (NEG) coating inside the chambers, first proposed by Benvenuti (1983). The proximity of the vacuum chamber and all the other in-vacuum components to the beam, increase the beam coupling impedance, which leads to higher heating of the components and to instabilities (NAGAOKA; BANE, 2014). The stronger magnets also imply more sensitivity of the lattice to errors, such as construction errors of the magnets, misaligments and multipoles (NEUENSCHWANDER *et al.*, 2015; HETTEL, 2014a), and, together with the very small transverse sizes of the beam, require tight tolerances on ripple from the power supplies and vibration, not only of the magnets, but also of the components of the beamlines, such as the monochromators (SUSINI *et al.*, 2014; SIEWERT *et al.*, 2014) and also for the detectors at the experimental stations (DENES; SCHMITT, 2014). Underlying all these intrincacies is the need of very detailed design, characterization and, in some cases measurement, of all the components that are installed in the light source. Besides, detailed single particle models of the storage ring are fundamental to evaluate the effect of each new design on the global properties of the ring, such as beam lifetime and dynamic aperture. All this requires very detailed simulations and high computational power (BORLAND *et al.*, 2014).

Regarding the beam coupling impedance, the last 3$^{\text{rd}}$ GLS that were built already demonstrated concern to evaluate the budget of the ring, simulating and, more importantly, designing the components to minimize heating and other impedance related issues (NAGAOKA, 2004a; GÜNZEL; PEREZ, 2008; BLEDNYKH; KRINSKY, 2007; BLEDNYKH *et al.*, 2009). For 4$^{\text{th}}$ GLS this approach is practically mandatory because the predictions for thresholds for strong instabilities are much lower for these machines than they were for 3$^{\text{rd}}$ GLS (KLEIN *et al.*, 2013; LINDBERG; BLEDNYKH, 2015; PERSICHELLI *et al.*, 2017; WANG *et al.*, 2017a; WANG *et al.*, 2017b). Besides, the use of NEG technology extended along the whole ring requires more detailed analysis of its effect on the impedance.

1.4 Collective Effects

Collective effects can cause severe deterioration of the brightness of a machine because they can lead to the increase of the effective emittance of the electron beam, through coherent oscillations of the bunches, increase of the energy spread and the beam sizes in all three planes. Besides, they can even cause beam loss, which limits the maximum current that can be stored and consequently the total photon flux of the machine. In this section we will introduce the main mechanisms that drive collective effects in a storage ring.

1.4.1 Interaction Mechanisms

One of the most important interaction for storage rings of light sources is the collision of particles, generally refered to as Coulomb scattering or intrabeam scattering, which is so unpredictable and chaotic that its effects on the beam resembles the properties of the emission of radiation, causing emittance and energy spread increase (PIWINSKI, 1974; BJORKEN; MTINGWA, 1983; KUBO *et al.*, 2001). Additionally, the collision process also leads to particle loss through a mechanism called Touscheck scattering, described in details by Piwinski (1998), where the transverse energy of oscillation is transfered to the longitudinal plane and the particles gain an energy deviation so large that they are lost. All these effects are very detrimental to new light sources, being the Touscheck lifetime their main source of particle loss, according to Nagaoka & Bane (2014).

The direct space charge (DSP) is another type of interaction among the particles, being the result of the action of the cloud of electromagnetic field existent inside the beam on individual particles. Each particle generates an electric and a magnetic field that, when averaged among all particles, result in a net potential dependent on the shape and sizes of the bunch. This potential acts like an external field on the movement of the particles, leading to tune–shifts with amplitude and possible excitation of resonances. However, for ultra-relativistic electron beams such as the ones of a light source storage ring, with energies of the order of a few GeV, this effect is very small and can be neglected. This happens because in this limit the non-radiating field generated by each particle is concentrated in a plane transverse to its movement and the electric and magnetic forces that act on other particles moving parallel to it cancel each other out. In Appendix A a more detailed explanation for this property is given.

The CSR is another type of direct interaction between particles in a beam. The radiation emitted by the particles travels forward with the velocity of light and, due to the fact that the particles are moving on a curved trajectory when they emit light, this radiation catches up with the particles ahead of the emitting particle, as first described by Derbenev *et al.* (1995). If the wavelength of the radiation is of the same order of or larger than the bunch length, the average of this effect is non-zero and the head of the bunch feels a net force. As this effect depends on the radiated field, in contrast to the DSP, it does not tend to zero as the energy of the particles increases and can be very harmful, depending on the bunch length of the beam, causing energy spread increase and bunch lengthening or even microbunching (BYRD *et al.*, 2002). However, this mechanism of interaction suffers from shielding of the vacuum chamber because, depending on the transverse separation of the walls, the low frequency radiation cannot propagate, which mitigates the effect (MURPHY *et al.*, 1997).

All mechanisms described above are examples of direct interactions among the particles, they do not depend on the environment in which they are imersed to happen.

The wake fields and the indirect space charge (ISP) on the other hand, use the vacuum chamber as intermediary of the interaction. The contact of the non-radiating field of the beam with the metallic walls of the chamber induces currents in the surface of the metal that travels with the beam, these surface currents also generate an electromagnetic field that propagates to the center of the vacuum chamber and influences the movement of the particles, as described by Laslett (1963). This electromagnetic field can have properties of non-radiating and radiating field, depending on the characteristics of the vacuum chamber. If we consider the chamber is perfectly conducting and with translational symmetry in the longitudinal direction, then the surface charges travel in straight lines with the beam speed, which means they will produce only non-radiating fields with the same properties of those of the DSP. This is the origin of the ISP, that for the same reasons as the DSP is negligible for high energy storage rings[3].

1.4.2 Wake Fields

If any of the two conditions imposed on the vacuum chamber is broken, then the surface charges also generate radiating fields or fields that are dragged behind the source particle, namely wake fields. For example, if the vacuum chamber has no longitudinal translational symmetry, then the surface charges must follow curved paths, which makes then suffer accelerations and hence, radiate electromagnetic fields. Notice that this is only one of the several possible ways of introducing this mechanism, it would be equivalent to say that the surface of the metal scatter the fields generated by the particles in the beam and when the surface of the vacuum chamber has longitudinal symmetry the refletion is specular but when it has corrugations or transitions, the scattering is difuse. Precisely what happens is that the walls of the vacuum chamber impose boundary conditions (BC) on the fields that exist inside the vacuum vessel, univocally defining its time and spatial dependency.

The wake fields can be very harmful to the beam, changing the properties of the static distribution of particles and creating instabilities above a given current threshold, which can lead to coherent oscillations of the bunches, emittance and energy spread increase and even beam loss. All these effects cause serious deteriorations of the brightness of the radiation, limiting the photon flux and bringing deterioration of its phase space average distribution.

[3] This statement is not true for static (or quasi–static) fields, because the electric and magnetic components of the force decouples and they depend if the boundary is a good electric conductor or a high–μ magnetic material. This problem was first studied by Laslett (1963) and will be addressed later in this work.

1.5 The Sirius Project

The National Center for Research in Energy and Materials (CNPEM) is a brazilian institution located in Campinas-SP that gathers four national laboratories, being the Brazilian Synchrotron Light Laboratory (LNLS) one of them. This laboratory was created in 1987 with the objectives of to project, construct and operate a SLS. Such goals were successfully achieved with UVX, a second generation light source which begun operation with external users in 1997. Since them, the brazilian community of synchrotron users has grown and studies of a new, more competitive machine, started in 2008.

By the end of 2011, Sirius was a well developed project and it consisted on a permanent magnet based 3$^{\text{rd}}$ GLS, with an energy of 3 GeV, an emittance of the order of 2 nm rad and circumference of 480 m, as described by Liu *et al.* (2010) and Liu *et al.* (2011). This scenario changed after the first reunion of the Machine Advisory Committee (MAC), in june of 2012, when the committee inspired the project leaders to follow the example of MAX-IV (LEEMANN *et al.*, 2009) and pursue sub-nanometer emmittances. This challenge was accepted and Sirius became the second project to fit the category of what today is called 4$^{\text{th}}$ GLS[4], with a natural emittance even lower than MAX-IV's (LIU *et al.*, 2013).

After several changes in the magnetic lattice (LIU *et al.*, 2014; LIU *et al.*, 2015; LIU *et al.*, 2016a) to improve the brightness of the light generated by the IDs that are being planned for Sirius (SIRIUS, 2013; VILELA *et al.*, 2017), the current lattice of the storage ring is the one presented in Figure 6 and the current optical functions are presented in

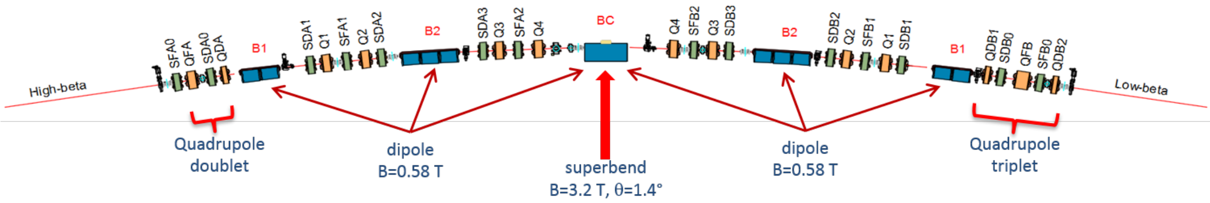

Figure 6 – One fourth of the unit cell of the Sirius storage ring. Dipoles are shown in blue, quadrupoles in orange and sextupoles in green. The vacuum pumps and valves are also shown. Only half of the high-beta (A) and of the low-beta (B) straight sections are shown. The arc and the straight sections are repeated to form the unit cell in the following way: A-B-B-B. The unit cell is then, repeated five times to form the ring.

Figure 7. The arc of the cell, composed of all the elements from the first to the second B1 dipole, inclusive, is repeated twenty times to form the ring. The straight sections alternate in sections with two quadrupoles (A), and sections with three quadrupoles (B),

[4] In the beginning these machines were called "The Ultimate Light Sources". But as the initial excitement of the community faded away the names became more humble and today it seems they have converged to "4th Generation Light Sources" and "Diffraction Limited Light Sources".

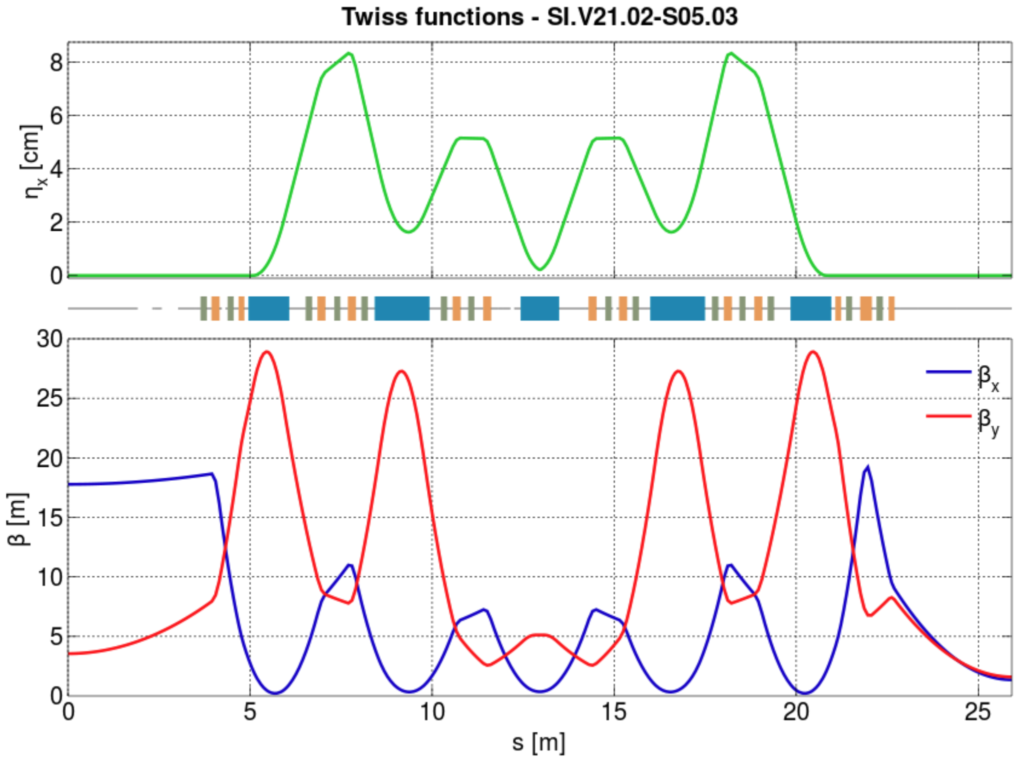

Figure 7 – Optical (twiss) functions for one fourth of a period of the Sirius lattice. In green is shown the dispersion function, in red, the vertical betatron function and in blue the horizontal betatron function. Notice the strong focusing of the betatron functions at the center of the low-beta (B) sections. (copied from Sirius (2013).)

in the following manner: A-B-B-B, in such a way that the ring has five A sections and fifteen B sections. The difference between these two types of sections is that beam is strongly focused in the B sections, to improve the radiation generated by the undulators which will be installed there and the A sections are optimized for the injection from the booster, that will take place in one of them. This way the ring has twenty straight sections, from which eighteen will be available for installation of IDs. However the real symmetry of the ring is only five, which difficults the optimization of the single particle non-linear optics (SÁ *et al.*, 2016; DESTER *et al.*, 2017). In the center of each arc there is a special dipole magnet, with longitudinal gradient and a very strong peak field of 3.2 T in its center that will provide hard x-rays, with critical energy of 19.2 keV, for additional 20 beamlines (LIU *et al.*, 2016a; SIRIUS, 2013).

The whole accelerator complex of the Sirius SLS, shown schematically in Figure 8, will be composed of a 150 MeV LINAC, a full range booster synchrotron, that will ramp the electrons from the LINAC energy to the storage ring nominal energy with a cycling rate of 2 Hz, and the storage ring, as described in Sirius (2013) web page. The injection system will operate in topup mode, where the total current of the storage ring is kept constant along the whole operation shift, because periodic injection cycles along the

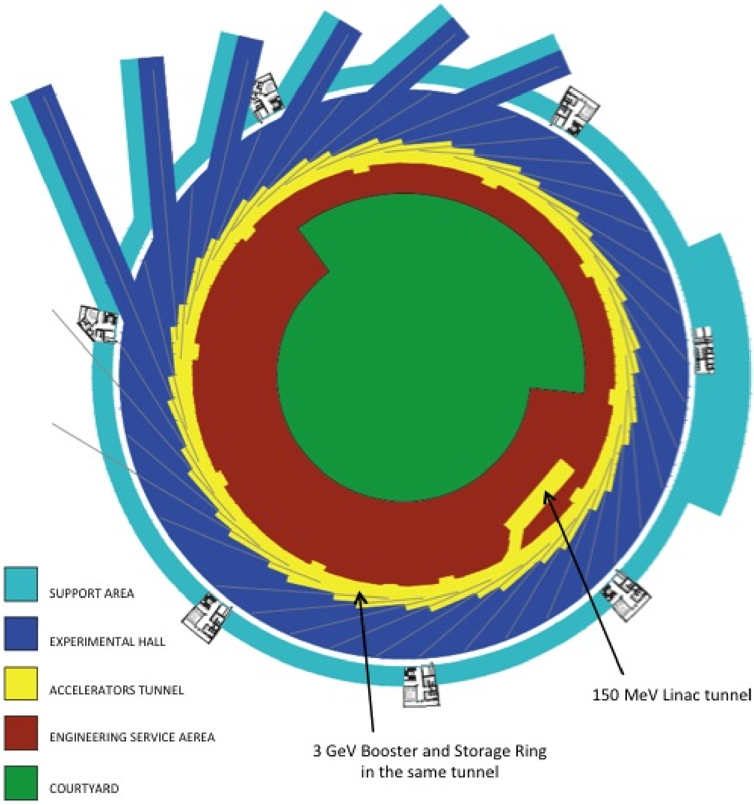

Figure 8 – Sirius building layout, showing all the important areas of the light source, with emphasis to the booster sharing the same tunnel as the storage ring and the 150 MeV LINAC tunnel. The experimental hall will be able to accomodate beamlines up to 100 m long and the requirement for longer beamlines, with possible length up to 450 m, is anticipated. (copied from Sirius (2013).)

day are performed without the need of interrupting the operation of the machine. The booster will be concentric to the storage ring and placed inside the same tunnel, which minimizes costs related to the construction of a separate shielding and helps diminishing its emittance, only 3.5 nm rad at 3 GeV (SÁ *et al.*, 2014), which is important to maximize the injection efficiency in the storage ring (LIU *et al.*, 2016b).

Table 1 shows the main global parameters of the storage ring for the predicted operation phases of the machine along the next years. Even though the commissioning will be performed with a normal conducting PETRA 7-Cell RF cavity, in the users operation phases of the storage ring the RF cavities will be Superconducting RF Cavity (SC-RF). It is predicted the installation of a 3th harmonic passive landau cavity to lengthen the bunches and increase the lifetime, allowing multi-bunch operation with higher currents. There is no prediction of operation with single bunch, but high single bunch current in the middle of the train is foresaw. Even though the expected filling of the machine is the uniform shape, it is possible the need of operating with gaps due to ion instabilities (WANG *et al.*, 2013; NAGAOKA; BANE, 2014).

Table 1 – Main Parameters of the Sirius Storage Ring.

Parameter	Symbol	Operation Phases			Unit
		Commiss.	Phase 1	Phase 2	
Energy	E_0	3.0			GeV
Circumference	L_0	518.4			m
Revolution period	T_0	1.73			µs
Revolution frequency	f_0	578			kHz
Angular rev. freq.	ω_0	3.632			$\mathrm{Mrad\,s^{-1}}$
Harmonic number	h	864			
Momentum compaction	α	1.7×10^{-4}			
Transverse tunes (H/V)	$\nu_{x/y}$	49.11/14.17			
Energy loss per turn	U_0	473			keV
Natural emittance	ε_0	252			pm rad
Natural energy spread	σ_δ	85×10^{-5}			
Damping times (H/V/L)	$\tau_{x/y/z}$	16.9/22.0/12.9			ms
Damping rates (H/V/L)	$\alpha_{x/y/z}$	59.2/45.5/77.5			Hz
Nominal total current	I_0	30	100	350	mA
Current per bunch	I_b	34.7	116	405	µA
RF cavity		1 7-Cell	2 SC-RF		
Voltage gap	V_0	1.8	3.0		MV
Natural bunch length	σ_z	3.2(10.7)	2.5(8.2)		mm (ps)
Synchrotron Tune	ν_z	3.56×10^{-3}	4.6×10^{-3}		

1.6 Description of the work

The first objectives of this work were to study the subject of wake fields and impedances in accelerators and their effects on the beam dynamics of electron storage rings. The following goals were to apply this knowledge gathered from the literature to the Sirius storage ring, building the impedance budget with semi-analytical and numeric calculations of the impedances of the main components[5], with special care to the characterization of the effect of the NEG coating on the total impedance; and to perform calculations to predict the beam instabilities thresholds and study the possible cures for them.

This thesis is organized in the following manner: in Chapter 2 the main concepts of the single particle dynamics, important for the development of the rest of the work, will be introduced; in Chapter 3 the main aspects of the wake field theory will be presented with focus to the physical interpretation of the quantities introduced; in Chapter 4 the methodology for computation of the impedance effects on the beam will be briefly described, with references for more detailed works and explanation of the derivation of the equations; in Chapter 5 the models applied to the impedance calculation of the main components of the storage ring will be presented and justified;

[5] This part of the work was done togheter with other members of the LNLS team.

2 SINGLE PARTICLE DYNAMICS

In this chapter the main concepts of single particle dynamics that will be useful for the rest of the work will be introduced without any intention to be complete or rigorous in the presentation. There are great books, for example the ones written by Lee (1999) and by Wiedemann (2007), and also one outstanding report written by Sands (1970) that cover all the topics presented here, and much more, with incredible didactics. Besides, Borland *et al.* (2014) give a quick overview on all the topics relevant for single particle dynamics.

2.1 Reference System

Connected to the concept of a storage ring is the one of the reference orbit. This special closed orbit is the one that an idealized particle, the synchronous particle, with the storage ring nominal energy would follow if it had the correct initial conditions. Besides, all the components of a storage ring are aligned according to this special orbit in such a way that their center, symmetry points or axis coincide with it and, in practice, the trajectories of all particles stored in the machine will be close to it. For this reason, the reference orbit is chosen to be the origin of the reference frame, defining a curved coordinate system that moves along the ring, with one longitudinal coordinate tangent to the local orbit and two transverse coordinates perpendicular to it. This type of co-moving coordinate system is a particular case of a Frenet-Serret frame (FRENET, 1852; SERRET, 1851; Wikipedia Contributors, 2017d), where the torsion is always zero, due to the fact that storage rings only have dipoles to bend the trajectories in the horizontal plane. Such a coordinate system can be defined in the following way (LEE, 1999, chap. 2):

$$
\begin{aligned}
\hat{\boldsymbol{s}}(s) &= \frac{\mathrm{d}\vec{\boldsymbol{r}}_0(s)}{\mathrm{d}s}, \\
\hat{\boldsymbol{x}}(s) &= -\rho(s)\frac{\mathrm{d}\hat{\boldsymbol{s}}(s)}{\mathrm{d}s}, \\
\hat{\boldsymbol{y}}(s) &= \hat{\boldsymbol{s}}(s) \times \hat{\boldsymbol{x}}(s),
\end{aligned}
\tag{2.1}
$$

where s is the arc length of the reference orbit starting from an arbitrary point, $\vec{\boldsymbol{r}}_0$ is the position of the reference orbit in relation to a static, cartesian reference frame, $\hat{\boldsymbol{s}}$ is the vector tangent to the orbit, standard from the Frenet-Serret description, $\hat{\boldsymbol{x}}$ is the negative of the normal vector, generally called in accelerator physics as radial or horizontal coordinate, $\hat{\boldsymbol{y}}$ is the standard binormal versor, often called as vertical direction in accelerator physics. The scalar ρ is the local radius of curvature of the reference orbit, which is equal to the one introduced by the dipoles, as defined in equation (1.1). This

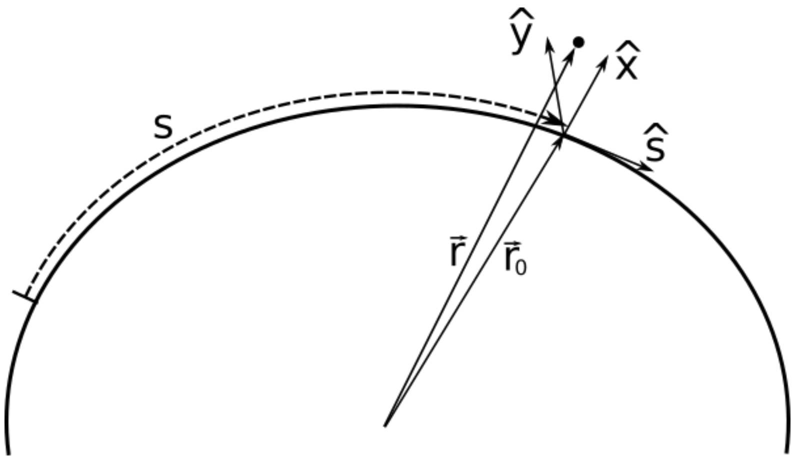

Figure 9 – Frenet-Serret reference frame of a storage ring, with right-handed coordinate system $\{\hat{\boldsymbol{x}}, \hat{\boldsymbol{y}}, \hat{\boldsymbol{s}}\}$. Adapted from (LEE, 1999, pp. 123).

means that the reference frame of an accelerator is piecewise straight with curvature different from zero only at the dipoles.

With the definitions above, the position of an arbitrary particle can be described as small deviations from the reference orbit (see Figure 9)

$$\vec{\boldsymbol{r}}(s) = \vec{\boldsymbol{r}}_0(s) + x\hat{\boldsymbol{x}}(s) + y\hat{\boldsymbol{y}}(s) \tag{2.2}$$

with x and y being the horizontal and vertical displacements of the particles in relation to the reference orbit. In this reference frame, the dynamics of each particle can be represented by its position in the six dimensional phase space defined by:

$$\{x, x', y, y', z, \delta\} \tag{2.3}$$

with

$$x' = \frac{\mathrm{d}x}{\mathrm{d}s} \approx \frac{p_x}{p}, \quad y' = \frac{\mathrm{d}y}{\mathrm{d}s} \approx \frac{p_y}{p}, \quad \delta = \frac{p}{p_0} - 1 \tag{2.4}$$

where p_0 is the storage ring nominal linear momentum, $\delta \approx \Delta E/E_0$ is the energy deviation of the particle in relation to the nominal energy of the storage ring and x' and y' are the normalized transverse components of the linear momentum of the particle. The coordinate z is defined as the relative longitudinal position of the particle in relation to the synchronous particle

$$z(t) = s_{\text{sync}}(t) - s(t) \tag{2.5}$$

where t is the wall-clock time and $s_{\text{sync}}(t)$ is the position of the synchronous particle. Notice if the particle is ahead of the synchronous particle then z will be negative. This convention is very important and will be consistently adopted throughout this work.

2.2 Transverse Dynamics

At this point it is convenient to describe in general terms how is the movement of the stored particles. They are ultra-relativistic electrons with energy of the order of a few GeV, and most of their velocity is always in the direction of the tangent of the ideal orbit. There are approximately hundreds of billions electrons grouped in several bunches along the reference orbit, each bunch having length of a few milimiters and transverse sizes of the order of dozens of microns. Each electron is under the influence of a variaty of electromagnetic fields (gravity can be neglected), coming from the static magnetic fields of the dipoles and multipoles, the radiofrequency field of the RF cavity, the direct fields of other electrons in the same bunch and the fields scattered by the vacuum vessel, generated by other electrons in the same bunch, in other bunches or even by themselves in previous turns. Also, they emit synchrotron radiation which makes them lose energy and perturb their movement with a recoil effect.

The description of the dynamics of the stored particles begin with an approximation that neglect the effects of their self-fields, i.e. their interaction with each other, with the vacuum chamber and with the residual molecules in their atmosphere. In this framework the only forces acting on the particles are the magnetic fields of the dipoles and multipoles and the longitudinal electric field of the RF Cavity and the only way they can lose energy is through synchrotron radiation emission. Under such conditions, the one turn map of the ring defines a fixed point in the phase space defined in equation (2.3) and the particles oscillate around it, being the oscillations in the planes $\{x, x'\}$, $\{y, y'\}$ and $\{z, \delta\}$ practically uncoupled. The oscillations in the first two planes are called transverse oscillations, while the one in the third plane is denominated longidutinal oscillation.

When such calculations are performed for current synchrotrons it is noticeable that the dynamics of the longitudinal motion is much slower than the dynamics of the transverse motion. As an example, in the Sirius storage ring particles take approximately 215 revolutions around the ring to complete one turn around the fixed point in the longitudinal direction while they oscillate 49 times per revolution around the fixed point in the transverse plane. This property makes it possible to separate the study of the longitudinal plane from the transverse one, considering the energy deviation of one particle as a constant parameter in the transverse equations of motion. The effects of the radiation energy loss are even slower than the longidudinal motion, taking a few thousands of turns in the ring to significantly change the transverse motion.

Neglecting the energy variations of the particles, and the randonnes of the radiation emission, the motion of the particles can be described by a hamiltonian in the Frenet-Serret coordinate system defined by the ideal orbit. Procceding in the approximations, considering the paraxial motion of the particles around the closed orbit, this hamiltonian can be simplified to a quadratic form in the momenta coordinates. See, for example, the second chapter of reference (LEE, 1999, pp. 32).

This Hamiltonian generates two second order coupled and non-linear equations of motion for the transverse coordinates that accurately describe the short and mid-term stability of the particles. Most of the non-linearities and coupling in these equations come from the magnetic fields of the magnets along the ring, being the other contributor the curvature of the reference orbit and the energy deviation of each particle. At this stage of the simplification of the problem the dynamics of the electrons still is very complicated, mainly for storage rings such as Sirius, with several and very strong Sextupoles that introduce chaos in the system in regions of the phase-space that are close to the fixed point.

2.2.1 Linear Equations of Motion

With further approximations, considering only the terms of the equations of motion that are linear with the phase-space coordinates and eliminating all coupling between the two transverse directions, the analysis of the dynamics becomes simple enough to allow its complete understanding, with analytical solutions to the equations of motion and physically significant parametrizations, that summarizes and simply describes a given machine. In this regime, the transverse movement of the electron is only dependent on the fields of dipoles and quadrupoles. Under such considerations, the Hamiltonian of an arbitrary particle stored in the ring is given by

$$H \approx \frac{x'^2}{2} + \frac{y'^2}{2} + \frac{G^2(s)}{2}x^2 + \frac{K(s)}{2}\left(x^2 - y^2\right) - G(s)x\delta \tag{2.6}$$

where we notice the Hamiltonian is normalized by the total momentum of the particle, p, and expanded up to second order in the transverse phase space coordinates, in such a way that only dipoles, $G(s)$, and quadrupoles, $K(s)$, contribute to the dynamics. Besides, the independent variable was changed from time to the longitudinal position of the particle along the Frenet-Serret frame, which is possible because s is a monotonic function of the time in storage rings, which allow easy invertion of derivatives. All the steps to get the equation above are described in details in the literature (BENGTSSON, 1997; LEE, 1999; WIEDEMANN, 2007). The equations of motion will be:

$$\begin{aligned} x'' &= -\frac{\partial H}{\partial x} = -\left(K(s) + G^2(s)\right)x + G(s)\delta \\ y'' &= -\frac{\partial H}{\partial y} = K(s)y \end{aligned} \tag{2.7}$$

where the energy deviation dependent term in the horizontal equation of motion is the dispersion generated by the dipole.

Looking back at the beggining of this section and reviewing all the approximations, at first sight it seems that the region of validity of these linear equations is so limited that their understanding is useless. However that is not what is observed in practice, because storage rings are carefully designed to maximize the validity of this linear behavior: the position, number and strength of all magnets are so well tuned that nonlinearities cancel each other. Another important point to justify the study of these linear equations is that, luckly, for synchrotron radiation generation the smaller the transverse size and divergence of the electron beam the better, which means most particles will stay for most of the time in a very small region of approximately hundreads of microns around the fixed point, where only the linear part of the one turn map have a significant effect on the dynamics. Besides, if a particle experience large transverse oscillations and happens not to be lost, damping effects that arise due to synchrotron radiation emission will bring them close to the fixed point in a few dozens of miliseconds.

2.2.2 Betatron Function and Phase Advance

The homegeneous part of the equations of motion presented in equation (2.7) can be cast in the following way:

$$u'' + K_u(s)u = 0 \tag{2.8}$$

where u can be both, x and y and $K_x = K(s) - G^2(s)$ and $K_y = -K(s)$. These equations are known as Hill equations and their solutions can be parametrized in the following form, as showed by Courant & Snyder (1958):

$$u(s) = \sqrt{2J\beta_u(s)}\cos(\mu_u(s) - \phi) \tag{2.9}$$

where $\beta_u(s)$ is called the betatron function and depends only on the magnetic lattice and $\mu_u(s)$ is called phase advance and its relation to the betatron function is given by

$$\mu_u'(s) = \frac{1}{\beta_u(s)}. \tag{2.10}$$

The constants ϕ and J depend on the initial conditions. It can be shown that:

$$J = \gamma_u(s)u^2(s) + 2\alpha_u(s)u(s)u'(s) + \beta_u(s)u'^2(s), \quad \text{with} \tag{2.11}$$

$$\alpha_u(s) = -\frac{\beta_u'(s)}{2} \quad \text{and} \quad \gamma_u(s) = \frac{1+\alpha_u^2(s)}{\beta_u(s)},$$

which represents the equation of an ellipse in phase space with J being the area of such ellipse.

The relevance of this parametrization is that there are several very important practical informations regarding the properties and responses to perturbations of the beam that can be extracted directly from the betatron function. It can be seen from equation (2.9) that the maximum excursion a given particle can experience in a fixed longitudinal point of the ring is proportional to the square root of the betatron function. Analogously, the beam size of a distribution in equilibrium will also be proportional to the square root of the local betatron function. Thus, the ratio between the amplitudes of movement in two different positions is proportional to the ratio of the square root of the betatron functions at the two locations, a property that is fundamental in the process of defining the transverse sizes of the vacuum chamber of a storage ring. For example, lets suppose the maximum betatron function of a lattice is 16 m and at this place the vacuum chamber has an internal dimension of 12 mm. This means that in another place where the betatron function is only 1 m the vacuum chamber can be much smaller, only 3 mm, without affecting the stored beam, which would allow the installation of devices that requires smaller appertures. This strategy of focusing the betatron function is commonly used in storage rings in straight sections where IDs are installed, with smaller gaps they can generate stronger magnetic fields, which is desirable for radiation emission. The name of this curve that defines the minimum apperture the vacuum chamber can have along the ring is calles Beam Stay Clear (BSC).

Another important property that can be infered from the betatron function is the sensitivity of the beam to spurious eletromagnetic fields. It can be shown that the larger the betatron function the larger the effect of such field in the beam dynamics. In the special case of dipolar fields, which are constant in the transverse plane, this dependency goes with $\sqrt{\beta(s_0)}$, for a quadrupolar field it is proportional to $\beta(s_0)$, for a sextupole $\beta^{3/2}(s_0)$ and so on.

Besides the betatron function, another important advantage of the parametrization presented in equation (2.9) is the interpretation of the integral of the phase advance in one turn around the ring. This integral normalized by 2π defines the tune of the machine:

$$\nu_u = \frac{1}{2\pi}\oint \mathrm{d}s \frac{1}{\beta_u(s)}. \tag{2.12}$$

The integer part of this number corresponds to the number of complete oscillations in the phase space the particles make in one turn in the ring. To interpret the fractional part it is important to notice in equation (2.9) that the movement of a particle in a fixed longitudinal position in sucessive turns is a perfect senoid, independently of the parametrization:

$$u_i(s_0) = A_{u,0}\cos(2\pi\nu_u i - \phi_0). \tag{2.13}$$

where $A_{u,0}$ is a constant and the fractionary part of the tune is identified as the natural frequency of oscillation. This means that resonances can be excited by any electromagnetic field along the ring with a frequency equal to the tune times the revolution frequency. This is the main mechanism that drives the collective instabilities that will be studied in this work. The electromagnetic fields generated by a bunch of particles interacts with other bunches and, because they have the same oscillation frequency, which is the tune, a collective oscillation emerges due to resonance. This can even happen in a single bunch, where oscillations of the head of the bunch drives the tail to ever larger oscillations.

Additionally, resonances can even be excited by static fields if the tune is a rational number, as long as these fields have the correct transverse spatial dependency. For example, if the fractionary part of the tune is $1/2$ and there is a spurius constant quadrupolar field in some point of the ring, the kicks received by the particles in successive turns would always sum constructively and a resonance behaviour would be excited. If both transverse planes of motion are considered it can be shown that if the tune satisfies the equation:

$$m\nu_x + n\nu_u = p \tag{2.14}$$

where m, n and p are integers, resonances can be excited depending on the static magnetic field around the ring. The number $r^2 = m^2 + n^2$ is called the order of the resonance, and the lower the order the higher its strength. If both, m and n must be non-zero for the equation (2.14) to be true, then the resonance depends on the existence of coupling fields, where the position of the particle in one direction influences the kick in the other direction.

2.2.3 Dispersion Function

The inhomogeneous solution of the linear equations of motion can be written in the following form:

$$x_\delta(s) = \eta(s)\delta \tag{2.15}$$

where $\eta(s)$ is called dispersion function and, just like the betatron function, depends only on the magnetic lattice. Notice that this is a particular solution of the equation, where periodic conditions were applied. This choice has an advantage over other solutions because of the meaning of the dispersion function: its value along the ring give the shape of the averaged trajectory of a particle with non-zero energy deviation. In other words, this particular solution of the inomogeneus equation gives the closed orbit of off-momentum particles.

The dispersion function is very important to determine the equilibrium emittance of a storage ring (WIEDEMANN, 2007, pp. 304),

$$\varepsilon_0 \propto \oint \mathrm{d}s \frac{\mathscr{H}\left(\eta(s), \eta'(s)\right)}{\rho^3(s)} \tag{2.16}$$

where the minimization of the functional

$$\mathscr{H}(\eta(s), \eta'(s)) = \gamma_x(s)\eta^2(s) + 2\alpha_x(s)\eta(s)\eta'(s) + \beta_x(s)\eta'^2(s) \tag{2.17}$$

in the dipoles of the ring is one of the main goals when designing a storage ring. Besides, the dispersion function is important to calculate the momentum compaction factor, α, which is the relative difference in path length in one turn in the ring per unit of energy deviation:

$$\frac{\Delta L}{L} \approx \delta\alpha := \delta \oint \mathrm{d}s \frac{\eta(s)}{\rho(s)}. \tag{2.18}$$

This parameter, which in general is positive, is of fundamental importance for the longitudinal dynamics, because it couples linearly the time it takes for the particles to complete one turn in the ring with their energy deviation. Notice that the only sections of the ring which contribute to the integral are where the reference orbit is curved (in other places the radius is infinity) and this is because particles with more/less energy generally follow paths with larger/smaller radius in the dipoles, which increases/decreases the path lenth. Negative momentum compaction are possible to be obtained in several storage rings by adjusting the quadrupoles of the lattice, but these modes of operations are rare and in the case of Sirius it will not be possible to operate under such condition.

2.2.4 Action-Angle Variables

Finding the action angle variables for a given Hamiltonian is equivalent to solve the equations of motion, due to the simple time, or s, evolution of such variables. For hamiltonians with one elliptic fixed point, this task is achieved by performing canonical transformations in the phase space variables that brings them to the normal form, where the movement is a simple harmonic oscillator. Then, the radius in phase space is an invariant of motion and is recognized as the action. This procedure can be applied to the Hamiltonian of equation (2.6) by recognizing the dispersion orbit as a canonical transformation that changes the origin of the phase space (BERG, 1996, Appendix A2)

$$x(s) \to \overbrace{x(s) - x_\delta(s)}^{x_\beta}, \tag{2.19}$$

where $x_\delta(s)$ is given by equation (2.15), in such a way that the new Hamiltonian is purely a quadractic form, without the crossed term $x\delta$. This pure betatronic Hamiltonian can than easily be written in action-angle variables in the following way:

$$K = \frac{J_x}{\beta_x(s)} + \frac{J_y}{\beta_y(s)} \tag{2.20}$$

where J_x and J_y, defined by equation (2.11) are recognized as horizontal and vertical actions and the equation of motion shows that the angle variable, θ, is the phase advance, defined in equation (2.10):

$$J_u' = \frac{\partial K}{\partial \theta_u} = 0 \quad \text{and} \quad \theta_u' = \frac{\partial K}{\partial J_u} = \frac{1}{\beta(s)} = \mu_u' \tag{2.21}$$

These variables will be very important for this work, because the wake-fields will be included in the electron dynamics as perturbations to the Hamiltonian presented above.

2.2.5 Linear Map Formulation: Matrix Theory

An alternative way to describe the linear dynamics of a storage ring is via symplectic transfer matrices, where the evolution of the coordinates in phase space can be always written in the following form

$$\overrightarrow{\boldsymbol{u}}(s) = \overleftrightarrow{\boldsymbol{M}}_{s_0 \to s} \overrightarrow{\boldsymbol{u}}(s_0) \tag{2.22}$$

where $\overrightarrow{\boldsymbol{u}}(s) = (u(s), u'(s))$ is the coordinates in phase space and $\overleftrightarrow{\boldsymbol{M}}_{s_0 \to s}$ is the transfer matrix from points s_0 to s. This form of the time evolution of the coordinates can be obtained from equation (2.9) by derivation with respect to s and substitution of J and ϕ by the initial conditions $\overrightarrow{\boldsymbol{u}}(s_0)$. After this procedure, it can verified that $\overleftrightarrow{\boldsymbol{M}}$ can be written in normal form (BENGTSSON, 1997)

$$\overleftrightarrow{\boldsymbol{M}}_{s_0 \to s} = \overleftrightarrow{\boldsymbol{A}}(s) \cdot \overleftrightarrow{\boldsymbol{R}}(\mu_{s_0 \to s}) \cdot \overleftrightarrow{\boldsymbol{A}}^{-1}(s_0) \tag{2.23}$$

where R is a rotation matrix and A^{-1} is a transformation matrix to the normalized coordinates, given by

$$\overleftrightarrow{\boldsymbol{R}}(\theta) = \begin{bmatrix} \cos(\theta) & \sin(\theta) \\ -\sin(\theta) & \cos(\theta) \end{bmatrix} \quad \text{and} \quad \overleftrightarrow{\boldsymbol{A}}(\mu) = \begin{bmatrix} \sqrt{\beta_u} & 0 \\ -\frac{\alpha}{\sqrt{\beta_u}} & \frac{1}{\sqrt{\beta_u}} \end{bmatrix}, \tag{2.24}$$

and also satisfy the composition rule

$$\overleftrightarrow{\boldsymbol{M}}_{s_0 \to s_2} = \overleftrightarrow{\boldsymbol{M}}_{s_1 \to s_2} \cdot \overleftrightarrow{\boldsymbol{M}}_{s_0 \to s_1} \tag{2.25}$$

where $\{s_0, s_1, s_2\}$ in this order are sequential positions along the ring. Besides, successive turns around the ring at some position s_0 are completely described by the one turn matrix, $\overleftrightarrow{\boldsymbol{M}}(s_0)$:

$$\overrightarrow{\boldsymbol{x}}_n = \overleftrightarrow{\boldsymbol{M}}^n \cdot \overrightarrow{\boldsymbol{x}}_0, \quad \text{with} \quad \overleftrightarrow{\boldsymbol{M}}^n = \overleftrightarrow{\boldsymbol{A}} \cdot \overleftrightarrow{\boldsymbol{R}}^n(2\pi\nu) \cdot \overleftrightarrow{\boldsymbol{A}}^{-1} = \overleftrightarrow{\boldsymbol{A}} \cdot \overleftrightarrow{\boldsymbol{R}}(2\pi n\nu) \cdot \overleftrightarrow{\boldsymbol{A}}^{-1}. \tag{2.26}$$

This formulation of the linear transverse motion is very usefull for numeric calculation of the evolution of the particles.

2.2.6 Chromaticity and Action Dependent Tune-shift

The quadrupoles correct the chromatic effects in the orbit of the beam that are generated in the dipoles and the result of such a correction is the finite value of the dispersion function. However the quadrupoles also are dispersive components, which means their focusing strength depends on the energy of the particles. This dependency comes from higher order terms of the Hamiltonian, not shown in equation (2.6), and causes an effect on the beam where particles with different relative energy offset have different tunes.

The linear part of this dependency is called linear chromaticity, which, if not corrected, reduces the lifetime of the beam to a few seconds in most storage rings. For example, for the case of Sirius the chromaticity of the ring without sextupoles is ≈ -130 for the horizontal direction. This means that particles with an energy deviation of only $0.15\,\%$ would have a tune that is 0.2 smaller than the tune of a particle with zero energy deviation. As the energy deviation oscillates in the scale of hundreds of turns, this particle would almost certainly cross a resonance that would induce its loss. Considering the equilibrium energy spread of the Sirius storage ring is only half of this value, $\approx 0.09\,\%$, without chromaticity correction all particles with energy deviation above two sigma of this distribution would be lost.

The sextupoles are introduced in the machine to correct the linear chromaticity to values close to zero. In this processes of minimization they change the higher-order chromatic terms and also introduce geometric aberrations, non-linearities in the dynamics of all particles that reduces the region around the fixed point where the beam is stable. The main contribution of this effect for the dynamics in the vicinity of the fixed point is the generation of a linear dependency of the tune of each particle with its action variable, J_u. Writting the linear expansion of the tune as a function of the energy deviation and the action we get:

$$\begin{aligned}\nu_x(\delta, J_x, J_y) &\approx \nu_{x,0} + \xi_x\delta + A_{xx}J_x + A_{xy}J_y \\ \nu_y(\delta, J_y, J_x) &\approx \nu_{y,0} + \xi_y\delta + A_{yy}J_y + A_{yx}J_x\end{aligned} \tag{2.27}$$

where ξ_x and ξ_y are the horizontal and vertical chromaticities, and A_{xx}, A_{yy} and $A_{xy} = A_{yx}$ are the action dependent tune–shifts.

These are the most important one turn effects that affect the mid and long term dynamics of the electrons at small oscillation amplitudes, in such a way that if we average the Hamiltonian of equation (2.20) in one turn,

$$H_t(J_x, J_y) = \frac{1}{L_0}\oint \mathrm{d}s K(s) = \frac{\omega_0}{c}\left(\nu_x J_x + \nu_y J_y\right), \tag{2.28}$$

they can be added to it simply by writting

$$\begin{aligned}H_t(J_x, J_y, \delta) = \frac{\omega_0}{c}\Bigg(&(\nu_{x,0} + \xi_x\delta)J_x + (\nu_{y,0} + \xi_y\delta)J_y + \\ &A_{xx}\frac{J_x^2}{2} + A_{xy}J_yJ_x + A_{yy}\frac{J_y^2}{2}\Bigg).\end{aligned} \tag{2.29}$$

2.3 Longitudinal Dynamics

In the study of the transverse dynamics the time scale involved was of a few turns in the storare ring, which allowed us to treat the energy deviation of the particles as another constant of motion. In this section the dynamics of the electrons in a few hundreads of turns will be analysed. In this scale the transverse betatron oscillations are averaged out and the longitudinal dynamics, which describes the path length and energy oscillations around the fixed point, has its natural frequency. The main factors that influence the movement in this scale are the small unballances between the energy loss of the particles and their energy gain in the RF cavity in one turn and the revolution time variation due to the energy offset of the particles.

2.3.1 Changes in Revolution Time

When the energy of a particle changes, its velocity is also modified, which contributes to the change of the revolution time. For most storage rings of SLSs this effect is negligible when compared to the change in path length described by equation (2.18), due to the ultra-relativistic regime in which these machines operate. This allows us to approximate the left hand side (l.h.s.) of equation (2.18) to the relative change in revolution time. Then, from one turn to another, the relative position of a particle will change by:

$$z_{n+1} = z_n + \delta_n \alpha L_0 \tag{2.30}$$

where n refers to the current turn and $n+1$ to the next and L_0 is the nominal circumference of the ring.

2.3.2 The Energy Balance

It can be shown that the rate of energy loss of a particle due to synchrotron radiation emission is proportial to the inverse of square of the local curvature radius of the particle times the fourth power of its total energy (JACKSON, 1962, pp. 661: eq. 14.31). Translating this dependency to a storage ring, the energy loss in one turn depends on the magnetic fields of the lattice and on the energy deviation of the particle. For the ideal particle the average energy loss depends only on the magnetic field of the dipoles, but as the closed orbit for particles with non-zero energy deviation is different, its energy loss is also different, not only because of the intrinsic dependence of the emission, but also because of the slightly different magnetic fields it will experience in one turn. The combination of these effects can be modeled in the following linear approximation:

$$\Delta E_{\mathrm{Rad}} \approx -U_0 - E_0 L_0 \alpha_z \delta_n \tag{2.31}$$

where U_0 is the energy loss of the ideal particle in one turn, E_0 is the nominal energy of the storage ring and the coefficient α_z includes both effects, the intrinsic dependence on the energy and the different orbit fields.

The energy gain of a particle in the RF cavity is given by the integral of the longitudinal electric field, $E_\parallel$, along the path of the particle and depends only on the initial phase of the field when it enters the cavity:

$$\Delta E = V(t_0) = q \int_0^{L_c} \mathrm{d}s E_{\parallel}(s,t)|_{t=s/c+t_0} \tag{2.32}$$

where $V(t_0)$ is called the gap voltage of the cavity and L_c is its length.

Now lets assume the frequency of oscillation of the electromagnetic field inside the cavity, ω_{RF}, is exactly a multiple of the revolution frequency of the synchronous particle, ω_0:

$$\omega_{RF} = h\omega_0 \tag{2.33}$$

where h is called harmonic number. With this assumption, even though the fields are time dependent, the synchronous particle will always see the same conditions as it enters in the cavity. Now lets make a further assumption that the synchronous particle reaches the cavity in the exact time where it gains U_0 energy of the cavity:

$$V(0) = U_0 \tag{2.34}$$

where the time reference on l.h.s. is relative to the position of the synchronous particle. Considering both assumptions and combining the energy gain in the cavity with the energy loss in one turn, given by equation (2.31), we get the following one turn energy balance for a storage ring:

$$\delta_{n+1} = \delta_n - L_0\alpha_z\delta_n + \frac{V(z_{n+1}) - U_0}{E_0}. \tag{2.35}$$

where the subscript $n+1$ in the particle position means that it will go around the ring first and then pass through the cavity.

2.3.3 Phase Stability Principle

Combining equations (2.30) and (2.35) we get the one turn map for the longitudinal plane for which the synchronous position and the nominal energy defines a fixed point. To analyse the stability of this fixed point let's linearize the map in its vicinity:

$$\begin{bmatrix} z_{n+1} \\ \delta_{n+1} \end{bmatrix} = \overbrace{\begin{bmatrix} 1 & \alpha L_0 \\ -V_0' & 1 - L_0\alpha_z - V_0'\alpha L_0 \end{bmatrix}}^{M} \begin{bmatrix} z_n \\ \delta_n \end{bmatrix}. \tag{2.36}$$

where V_0' is the derivative of the voltage gap in relation to the arrival time of the particles at the synchronous position normalized by the nominal energy of the ring, E_0. It can be shown that the eigenvalues of the matrix M are given by the solution of the characteristic equation

$$\lambda^2 - \mathrm{Tr}\,(M)\,\lambda + \mathrm{Det}\,(M) = 0 \tag{2.37}$$

with $\mathrm{Tr}\,(M) = 2 - L_0\,(\alpha_z - V_0'\alpha)$ and $\mathrm{Det}\,(M) = 1 - L_0\alpha_z \approx 1$. This means that for the matrix to be stable, $\mathrm{Tr}\,(M) <= 2$ (COURANT; SNYDER, 1958), the derivative of the gap voltage must be positive/negative if α is positive/negative. To ilustrate this condition, consider that initially a particle arrives at the cavity ahead of the synchronous particle, the positive derivative means it will gain more energy, which makes it take longer to go around the ring, if the momentum compaction is positive, diminishing the difference of its arrival time to the synchronous particle for the next turn. This way all particles remain in an oscillatory movement around the fixed point with frequency given by

$$\mathrm{Tr}(M) = 2\cos(2\pi\nu_s) \approx 2 - (2\pi\nu_s)^2 \implies \nu_s \approx \frac{1}{2\pi}\sqrt{L_0\alpha_z + V_0'\alpha L_0}, \tag{2.38}$$

where ν_s is called synchrotron tune in analogy to the betatron tunes defined in subsection 2.2.2.

Additionally, the determinant of the one turn matrix is $(1 - L_0\alpha_z)$, which implies the oscillations are damped, with α_z being the damping factor. In most storage rings this effect is small compared to the oscillation time, requiring thousands of turns to influence the dynamics.

The voltage gap has the same harmonic composition as function of the arrival time as the electric field as a function of time. This means that the condition imposed in equation (2.33) implies that there are at least h stable fixed point along the ring and, as in general the voltage is a pure senoid, these are the only stable points. This means that it is possible to store up to h aglomerations of electrons, called bunches, in a storage ring.

2.3.4 The Potential Well

There is an important approximation to the map equations derived in the previous sections that consists in considering the turn by turn iterations as inifinitesimal transformations and taking the limit to the continuum, considering differences between turns as derivatives. With this considerations, the equations of motion becomes:

$$\begin{aligned} \frac{\mathrm{d}z}{\mathrm{d}s} &= \alpha\delta(s) \\ \frac{\mathrm{d}\delta}{\mathrm{d}s} &= \alpha_z\delta(s) + \frac{V(z(s)) - U_0}{L_0E_0}. \end{aligned} \tag{2.39}$$

If the damping term is not considered, the equations of motion can be derived from a static Hamiltonian, given by:

$$H_{\parallel} = \frac{\alpha}{2}\delta^2 \quad \overbrace{- \int_0^z \mathrm{d}w \frac{V(w) - U_0}{L_0E_0}}^{U(z)} \tag{2.40}$$

where the first term of the right hand side (r.h.s.) is the kinetic term and $U(z)$ is called the potential well, in an analogy with a potential energy. When the oscillations are small the potential well can be expandend in power series of the longitudinal position. Generally the RF cavity of storage rings are adjusted with each other in such a way that their potentials always sum constructively, creating a practically linear potential $V(z)$ around the fixed point, which implies the Hamiltonian can often be approximated by

$$H_{\parallel} = \frac{\alpha}{2}\delta^2 + \frac{V'}{2L_0}z^2 \tag{2.41}$$

which is an harmonic oscillator, equivalent to the linear map of equation (2.36), if the damping is not considered. This harmonic Hamiltonian is often used for analytical treatments of instabilities because it is a good approximation for most RF systems and also due to the simple expressions of its action-angle variables.

2.4 Radiation Damping and Equilibrium Parameters

The synchrotron radiation emission is a quantum process that happens uncorrelatedly among all the electrons in the beam. While the average emission has a well defined and smooth behavior, such as the spectra that are calculated with classical electrodynamics for dipoles and IDs, a closer look into the individual emissions reveals the random nature of these events. As expected the effect this process generates on the beam is also dual, the average emission is responsible for energy loss and damping of the longitudinal and transverse oscillations, while the single emission events generates uncorrelated motion in all planes that heat up the beam.

Both effects have very different dependency on the parameters of the particles. For example, in the last section we used the fact that the energy loss depends linealy with the energy deviation of the particles, which caused an exponential damping of the oscillations, i.e. a damping proportional to the amplitude of the oscillation, while the heating in the longitudinal plane happens because the emissions are instantaneous and uncorrelated among electrons or in time, having no short term dependency on any parameter of the electrons, which generates random walks for the energy deviations. Because these effects have such different dependencies they always compete with each other, if the amplitude of oscillation is large the damping dominates, if it is small there is a blow up. It is this competition that generates the equilibrium energy distribution of the beam and consequently, due to the potential well, the longitudinal distribution. While the amplitude of oscillation of each electron is in an endless variation, the average of all electrons in a bunch remains stationary, with both effects cancelling each other out.

In the transverse plane the effect of the radiation emission on the dynamics is not as direct as in the longitudinal plane. Damping in the transverse plane is a two fold effect: first the electrons lose transverse momentum due to radiation emission because the emission is mostly on the direction of motion. This does not change the normalized momentum of the electron, because the longitudinal momentum is also affected by this emission. In a second moment the electron passes through the RF cavity, where the longitudinal momentum is replenished but the transverse momentum is unchanged, which means the normalized transverse momentum is decreased. The liquid effect is an exponential damping of the transverse oscillations, proportional to the betatron action of the movement.

The excitations of oscillations happen in the horizontal plane because of the dispersion function in the dipoles. When an electron emits radiation its closed orbit abruptly changes, because its energy deviation has changed, however, as the position of the electron is the same as before, a betatron oscillation around the new closed orbit is excited. Again, both effects cancel out in the equilibrium, defining a distribution and consequently the natural emittance of the storage ring. In the vertical plane, as the dispersion is ideally zero, the excitations are created by a much weaker mechanism and the natural vertical emittance is practically zero. This mechanism is related to the fact that the photon emission is not exactly in the direction of the momentum of the electrons, but with an angle apperture around it proportional to $1/\gamma$, which slightly changes the vertical momentum of the electron, exciting betatron oscillations. In real storage rings, residual vertical dispersion function from magnet errors and coupling fields that transfer part of the horizontal emittance to the vertical plane completely dominate this process and define the vertical emittance of the beam.

2.4.1 Fokker-Planck Equation

All the arguments described in the last section can be mathematically described by modeling the evolution of the beam distribution in terms of the Fokker-Planck equation. In this framework we can consider the interaction of the electrons with the radiation they emit as large particles subjected to a weak random and Markovian force, with an approximately white spectrum. These are the conditions imposed on a system by the kinect theory in order for the distribution function to be described by such equation, according to Landau & Lifshitz (1981), Wang & Uhlenbeck (1945), Zwanzig (2001).

There are several works that explain the use of the Fokker-Planck equation in storage rings (LINDBERG, 2016; SUZUKI, 1983; SUZUKI, 1986; LEE, 1999; WIEDEMANN, 2007). Here, only the main results will be presented:

$$\frac{\partial \Psi}{\partial s} + \{\Psi, H\} = \mathscr{F}(\Psi) \tag{2.42}$$

where $\Psi = \Psi\left(\vec{\boldsymbol{q}}, \vec{\boldsymbol{p}}, s\right)$ is the beam distribution in phase space, $\vec{\boldsymbol{q}} = (x, y, z)$ and $\vec{\boldsymbol{p}} = (x', y', \delta)$ are the position and momentum vectors,

$$\{\Psi, H\} = \frac{\partial \Psi}{\partial \vec{\boldsymbol{q}}} \cdot \frac{\partial H}{\partial \vec{\boldsymbol{p}}} - \frac{\partial \Psi}{\partial \vec{\boldsymbol{p}}} \cdot \frac{\partial H}{\partial \vec{\boldsymbol{q}}} \tag{2.43}$$

is the Poison bracket between the Hamiltonian and the particle distribution, where the operators $\frac{\partial}{\partial \vec{\boldsymbol{q}}}$ and $\frac{\partial}{\partial \vec{\boldsymbol{p}}}$ are the gradients in relation to the positions and momenta of the phase space, and $\mathscr{F}(\cdot)$ is the Fokker-Planck operator for the accelerator, explicitly given by (LINDBERG, 2016, eq. 33)

$$\begin{aligned}\mathscr{F}\left(\Psi\right) =& \frac{2\alpha_z}{c}\left(\Psi + \delta\frac{\partial\Psi}{\partial\delta}\right) + D_z\frac{\partial^2\Psi}{\partial\delta^2} + \\ & \frac{2\alpha_x}{c}\left(\Psi + J_x\frac{\partial\Psi}{\partial J_x}\right) + D_x\left(J_x\frac{\partial^2\Psi}{\partial J_x^2} + \frac{\partial\Psi}{\partial J_x} + \frac{1}{4J_x}\frac{\partial^2\Psi}{\partial\theta_x^2}\right) + \\ & \frac{2\alpha_y}{c}\left(\Psi + J_y\frac{\partial\Psi}{\partial J_y}\right) + D_y\left(J_y\frac{\partial^2\Psi}{\partial J_y^2} + \frac{\partial\Psi}{\partial J_y} + \frac{1}{4J_y}\frac{\partial^2\Psi}{\partial\theta_y^2}\right)\end{aligned} \tag{2.44}$$

where c is the speed of light, $\{J_x, \theta_x\}$ and $\{J_y, \theta_y\}$ are the action-angle variables of the horizontal and vertical planes, as defined in equation (2.11), and α_u and D_u are the damping and diffusion terms introduced by the radiation emission in the three planes of motion, for which Sands (1970) and Wiedemann (2007) derive explict expressions.

Notice that equation (2.42) separates the hamiltonian forces in the l.h.s. and the dissipative and random forces in the r.h.s.. If the effect of radiation emission were not taken into account, the r.h.s. of would be zero and the l.h.s. would be a statement of the Liuville Theorem for Hamiltonian flow, which in the accelerators physics community is also known as Vlasov Equation. For machines that operate with heavy particles, such as the colliders that use protons or ions, this is approximately true and the beam never reaches the equilibrium, but for storage rings of synchrotron light sources, which mostly employ electrons, the Fokker-Planck terms are very important to describe the behaviour of the beam in time scales of the order of ms or higher, which are the scales where impedance related collective instabilities happen.

The Fokker-Planck equation can be used to calculate the equilibrium distribution of the beam. Considering the total Hamiltonian of the ring is given by the sum of equations (2.40) and (2.20),

$$H = \frac{J_x}{\beta_x} + \frac{J_y}{\beta_x} + \frac{\alpha}{2}\delta^2 + U(z), \tag{2.45}$$

the equilibrium distribution is a separable function in the three planes of motion because the H does not couple them. Besides, the horizontal distribution must be a function only of the invariant J_x, the vertical of J_y and the longitudinal of $H_{\|}$, because they are the invariants of motion:

$$\Psi(\vec{\boldsymbol{q}}, \vec{\boldsymbol{p}}) = f_x(x, x')f_y(y, y')f_z(z, \delta) = f_x(J_x)f_y(J_y)f_z(H_{\|}). \tag{2.46}$$

With these considerations the distribution commutes with the total Hamiltonian and the l.h.s. of the Fokker-Planck equation, (2.42), is zero. From the r.h.s. it can be shown that

$$\Psi(\vec{\boldsymbol{q}}, \vec{\boldsymbol{p}}) = \overbrace{\frac{\exp\left(-J_x/\varepsilon_x\right)}{2\pi\varepsilon_x}}^{f_x} \cdot \overbrace{\frac{\exp\left(-J_y/\varepsilon_y\right)}{2\pi\varepsilon_y}}^{f_y} \cdot \overbrace{\frac{\exp\left(-\frac{\delta^2}{2\sigma_\delta^2}\right)}{\sqrt{2\pi}\sigma_\delta}}^{f_\delta} \cdot \overbrace{\frac{\exp\left(-\frac{1}{2\sigma_\delta^2}\frac{2}{\alpha}U(z)\right)}{A}}^{\lambda} \tag{2.47}$$

with

$$\varepsilon_x = \frac{cD_x}{2\alpha_x}, \quad \varepsilon_y = \frac{cD_y}{2\alpha_y}, \quad \sigma_\delta = \frac{cD_z}{2\alpha_z}, \tag{2.48}$$

where ε_x and ε_y are the horizontal and vertical emittances, σ_δ is the energy spread of the beam and A is a normalization constant such that

$$\int \mathrm{d}z' \lambda(z') = 1 \tag{2.49}$$

It easy to see that the beam vertical size is given by

$$\sigma_y^2(s) = \left\langle y^2 \right\rangle = 2\beta_y(s) \int \mathrm{d}\theta_y \cos^2(\theta_y) \int \mathrm{d}J_y f_y(J_y) J_y = \beta_y \varepsilon_y \tag{2.50}$$

and that for the horizontal plane the canonical transformation that shifted the off-momentum fixed point, represented by equation (2.19), must be taken in account:

$$\sigma_x^2 = \left\langle (x+\eta\delta)^2 \right\rangle = \left\langle x^2 \right\rangle + \langle 2x\eta\delta \rangle + \eta^2 \left\langle \delta^2 \right\rangle = \beta_x \varepsilon_x + \eta^2 \sigma_\delta^2. \tag{2.51}$$

For the longitudinal plane, in the simple case of a quadractic potential well, as described by equation (2.41), we have

$$\sigma_z^2 = \int \mathrm{d}z' \lambda\left(z'\right) z'^2 = \frac{1}{A} \int \mathrm{d}z' \exp\left(-\frac{V'}{2L_0\alpha\sigma_\delta^2} z'^2\right) z'^2 = \sigma_\delta^2 \frac{L_0\alpha}{V'} = \sigma_\delta^2 \frac{c^2\alpha^2}{\omega_s^2}, \tag{2.52}$$

where $\omega_s = \omega_0 \nu_s$ is the synchrotron frequency.

3 WAKES AND IMPEDANCES

In the last chapter the main aspects of the single particle dynamics, governed by the guiding electromagnetic fields generated by the magnets and the RF cavity were analysed. The effects of the radiation emission on the particle that generated this radiation were also considered, and concepts such as equilibrium distribution of particles, emittance and energy spread were introduced, however no interaction among the particles in this distribution was considered. Besides the external fields, the self-fields, fields induced by the stored particles, are important to characterize the dynamics when the intensity of the beam becomes large. These fields have different effects on the beam depending on how the interaction happens. In this chapter we will study the theory of wake fields, analysing its main definitions and approximations.

3.1 Wake Fields

As described in sub-section 1.4.2, even though the mechanism behind the interaction among the stored particles through wake fields is very simple to describe qualitatively, a quantitative self-consistent description of this effect is practically impossible. The main difficulty comes from the fact that ME should be solved using the vacuum chamber of the whole ring being subjected to a source, the beam, that is varying due to the external fields and also due to the effect of the own fields that we want to find. In order to tackle this problem self-consistency must be forgotten and approximations must be done.

The first approximation is to consider that all the properties of the materials that compose the vacuum chamber are linear in relation to the intensity of the fields. This linearity combined with the linearity of the ME allow us to solve the electromagnetic fields for a single source particle and sum over the beam to get the desired result. Another approximation consists in breaking the storage ring in several small parts that do not interact with each other, which allow us to solve ME for each part independently. This approximation is valid for storage rings because generally the irregulaties or transitions in the vacuum chamber are far from each other in such a way that the fields generated in one of them cannot propagate to the other.

The two approximations described above already greatly simplifies the problem, but in order to make it tractable other two are needed: the rigid beam and the impulse approximations. The rigid beam approximation consists in considering that when the particles are passing through a component that generates wake fields they always move in straight lines parallel to each other with constant and equal speeds. Applying this approximation to the particles that generates the wake fields creates a simple algorithm to solve the ME for any structure, because it defines that the source of the fields is a particle moving straight in the logitudinal direction with constant speed. As the boundary conditions are imposed by the walls of the chamber, the whole problem becomes well defined. The impulse approximation consists in saying that the effect of the wake fields of a structure on the particles is only to change their momentum after the whole process and this change in momentum is given by the integral from minus infinity to infinity of the Lorentz Force on the unperturbed trajectory of the particle. Combining this approximation with the rigid beam, we see that the integral must be performed parallel to the source particle at a fixed distance from it.

To clarify these approximations, lets express them mathematically. First lets consider a particle with charge Q and velocity v moving in the vacuum chamber. The ME for the fields generated by this particle are given by:

$$\begin{aligned}
\vec{\boldsymbol{\nabla}} \cdot \vec{\boldsymbol{D}} &= Q\delta(x-x_0)\delta(y-y_0)\delta(s-vt) \\
\vec{\boldsymbol{\nabla}} \cdot \vec{\boldsymbol{B}} &= 0 \\
\vec{\boldsymbol{\nabla}} \times \vec{\boldsymbol{E}} &= -\frac{\partial \vec{\boldsymbol{B}}}{\partial t} \\
\vec{\boldsymbol{\nabla}} \times \vec{\boldsymbol{H}} &= Qv\hat{\boldsymbol{s}}\delta(x-x_0)\delta(y-y_0)\delta(s-vt) + \frac{\partial \vec{\boldsymbol{D}}}{\partial t}
\end{aligned} \tag{3.1}$$

where $\delta(\cdot)$ is the Dirac's Delta function, x_0 and y_0 defines the transverse displacement of the source particle, $\hat{\boldsymbol{s}}$ is the unitary vector that defines the longitudinal direction and

$$\vec{\boldsymbol{D}}(t) = \int_{-\infty}^{\infty} \mathrm{d}t' \varepsilon(t-t') \vec{\boldsymbol{E}}(t') \tag{3.2}$$

$$\vec{\boldsymbol{B}}(t) = \int_{-\infty}^{\infty} \mathrm{d}t' \mu(t-t') \vec{\boldsymbol{H}}(t'), \tag{3.3}$$

where ε and μ simplifies to the electric permittivity and magnetic permeability of the vacuum in the region inside the vacuum chamber where the source particle is, but can be any causal function that describes the dynamics of the material of the wall. Combining these equations with the BC of continuity of the perpendicular components of $\vec{\boldsymbol{D}}$ and $\vec{\boldsymbol{B}}$ and of the tangential components of $\vec{\boldsymbol{H}}$ and $\vec{\boldsymbol{E}}$, the problem is well defined and there is an unique solution for $\vec{\boldsymbol{E}}$ and $\vec{\boldsymbol{B}}$ inside the vacuum chamber. For the case when the chamber is considered as a Perfect Electric Conductor (PEC), the Fields inside the wall are zeroed by surface charge and currents in the inner wall, as described by Jackson (1962, sec. I.5).

Now, lets consider that there is a witness particle with charge q that feels the action of these fields in accordance to the approximations made before. We can express the variation in momentum of this particle in the following form:

$$\Delta \vec{\boldsymbol{p}}(\vec{\boldsymbol{\rho}}_s, \vec{\boldsymbol{\rho}}_w, z) = \int_{-\infty}^{\infty} \mathrm{d}t \; \vec{\boldsymbol{F}}(\vec{\boldsymbol{\rho}}_s, \vec{\boldsymbol{\rho}}_w, s, t)\Big|_{s=vt-z} \tag{3.4}$$

where $\vec{\boldsymbol{\rho}}_w$ and $\vec{\boldsymbol{\rho}}_s$ are the transverse positions of the witness and source particles, respectively, and z is the distance the witness particle is behind the source. The Lorentz force in this case is given by

$$\overrightarrow{\boldsymbol{F}} = q\left(E_s\hat{\boldsymbol{s}} + (E_x + vB_y)\hat{\boldsymbol{x}} + (E_y - vB_x)\hat{\boldsymbol{y}}\right). \tag{3.5}$$

All the conditions imposed above to simplify the problem are refered as zeroth order approximations by reference (STUPAKOV, 2000), which indeed they are in the sense that they define the minimum level of complexity the analysis of wake fields must contain to explain the behavior of the beam. However most of the considerations are well justified, for example, the assumption of linearity of the materials is justified by the fact that the intensities of the fields involved are not large compared to the saturation curves of the materials, in such a way that linearization of the responses is always possible. For example, the magnetic field of in-vacuum IDs is generated by ferromagnetic blocks placed with alternating magnetization direction along the beam trajectory. Generally there is a very thin copper foil between the blocks and the beam enviroment shielding the blocks from the self-fields of the beam, however very low frequency fields can penetrate the foil and reach the blocks, which makes them important for the determination of such fields and the effects on the beam. This was the case presented on reference (BLEDNYKH *et al.*, 2016) where a model for the wakes was built from the linearization of the response of such materials and a good agreement with beam measurements was achieved.

The approximation of breaking the ring in several small parts that contribute independently to the whole budget of wake in the machine is always revisited by people responsible for simulating the components of new machines. In several ocasions where elements that introduce variations in the vacuum chamber transverse profile are close they are simulated together to check if there is interference of one to another, but, apart from some cases where the elements have resonances with similar frequencies, the results show that one simulation with both components is equal the sum of them simulated separately.

The impulse approximation is also justified by the small effect these fields have on the dynamics of the beam. Actually this approximation is recurent in accelerator physics simulations; it is very common to create models for IDs and multipoles, such as quadrupoles and sextupoles, under this assumption. Even for these components, which are stronger than wake fields, the results are a good approximation to the more detailed simulation with thick components.

There are two different aspects of the rigid beam approximation that must be analyzed separately in order to justify it. The first is the consideration that the witness particle is always at a fixed distance z behind the source particle. This approximation is very good for any storage ring because as the particles are ultra-relativistic, their velocity is close to the light speed and even with a considerable energy difference between the particles, their velocity difference would be negligible. Additionaly, the typical energy variation inside a bunch is very small, of the order of 0.1 %.

The second aspect is related to the consideration that the particles traverse the structure parallel to the axis, because, in principle, sloping straight trajectories could also be considered and the momentum gain would be dependent on the angles x' and y' of the source and the witness particle. An inclined trajectory of the source particle could generate different electromagnetic fields in the structure, because the coupling between the two would be affected. Besides, an inclined trajectory of the witness particle would make it sample different fields yielding to a different momentum change. There is one study in literature made by Danilov (2000) where the author calculates the angular wake for a stripline and one experimental work of the same author (DANILOV *et al.*, 1993) where a current dependent damping of the oscillations is measured at the injection energy, 120 MeV, of the BEP electron storage ring. There are also some other related studies in literature (JONES *et al.*, 1998), however, there is no strong experimental evidence of the importance of such effect in the total impedance budget of a storage ring, maybe because of the paraxial nature of the movement of the particles.

One interesting feature of the impulse approximation is that, even though the interaction between two particles via wake fields does not respect Newton's third law of motion (action-reaction law) and, consequently, cannot be cast into an Hamiltonian formulation, the mean-field interaction, where the degrees of freedom of all the source particles of the beam are averaged out, does respect the Hamilton equations, because, as can be seen in equation (3.4), the change in momentum of the witness particle depends only on its position.

3.2 Wake Functions

The approximations performed in the last section led to a formula to describe the change in momentum of the witness particle and to a method of how to include this momentum change in the dynamics of this particle. In summary, everything we need to know in order to compute the effect of the wake fields are already defined, we just need to compute the total momentum variation for each particle due to the action of all the other particles. In this process it useful to define functions that are independent of the charge of the particles involved, being dependent only on the structure that generates the wake fields. These functions are called wake functions or simply wakes and are defined by

$$(w_x, w_y, w_s) = \frac{v}{qQ}\left(\Delta p_x, \Delta p_y, -\Delta p_s\right) \tag{3.6}$$

where the components of $\overrightarrow{\boldsymbol{\Delta p}}$ are given by equation (3.4). The factor v/qQ gives a unit of energy per unit of charge square to the wake function, which in SI unit system is $\mathrm{V\,C^{-1}}$. The minus sign in the definition of the longitudinal wake is introduced to give positive values a intepretation of energy loss when both charges, the witness and the source, have the same sign.

3.3 The Wake Potential

With the approximations performed in the section 3.1 together with the restrictions imposed on the electromagnetic fields by the ME it is possible to show that the wake functions can be derived from a scalar potential function, called wake potential. To show this, we will use the same approach of reference (STUPAKOV, 2000), that is credited to Alex Chao. Lets consider the Lagrangian of the witness particle:

$$L = -mc^2\sqrt{1-\frac{v^2}{c^2}} + q\overrightarrow{\boldsymbol{A}}\cdot\overrightarrow{\boldsymbol{v}} - q\phi \tag{3.7}$$

where $\overrightarrow{\boldsymbol{A}}$ is the potential vector of the electromagnetic fields defined in equation (3.1) and ϕ is the scalar potential of the same fields. Inputing this Lagrangian into the Euler Lagrange equation we get

$$\frac{\mathrm{d}}{\mathrm{d}t}\left(\overrightarrow{\boldsymbol{p}} + q\overrightarrow{\boldsymbol{A}}\right) = q\overrightarrow{\boldsymbol{\nabla}}\left(\overrightarrow{\boldsymbol{A}}\cdot\overrightarrow{\boldsymbol{v}} - \phi\right). \tag{3.8}$$

where $\overrightarrow{\boldsymbol{\nabla}}$ denotes derivation in relation to the witness particle position. Integrating the equation above with the considerations made in section 3.1 we get

$$\overrightarrow{\boldsymbol{\Delta p}} = q\int_{-\infty}^{\infty}\mathrm{d}t\overrightarrow{\boldsymbol{\nabla}}\left(vA_s - \phi\right) = \frac{qQ}{c}\overrightarrow{\boldsymbol{\nabla}}_R W. \tag{3.9}$$

where $\overrightarrow{\boldsymbol{R}} = (x_w, y_w, -z)$ and $W = W(\overrightarrow{\boldsymbol{\rho}}_s, \overrightarrow{\boldsymbol{\rho}}_w, z)$ is the wake potential and it was used that the velocity of the particle is in the longitudinal direction. It was also considered that the fields go to zero at infinity. It can be checked[1] that the wake functions as defined in equation (3.6) are obtained from the wake potential by

$$w_s = -\frac{\partial W}{\partial(-z)} = \frac{\partial W}{\partial z}, \qquad \overrightarrow{\boldsymbol{w}}_\perp = \overrightarrow{\boldsymbol{\nabla}}_{w,\perp}W, \tag{3.10}$$

and, as $W \in C^\infty$, we have the following equality

$$\frac{\partial\overrightarrow{\boldsymbol{w}}_\perp}{\partial z} = \overrightarrow{\boldsymbol{\nabla}}_{w,\perp}w_s. \tag{3.11}$$

which is known as Panofsky-Wenzel theorem. It is also possible to show that in the ultra-relativistic limit, $v \to c$, the wake potential is an harmonic function of the transverse coordinates of the witness particle (STUPAKOV, 2000)

$$\nabla^2_{w,\perp}W = \frac{\partial^2 W}{\partial x_w^2} + \frac{\partial^2 W}{\partial y_w^2} = 0, \tag{3.12}$$

[1] In Appendix D there is a demonstration of the equalities in equations (3.10).

and, if perfect conducting walls are assumed at the ends of the structure, it is also an harmonic function in relation to the transverse coordinates of the source particle (ZAGORODNOV *et al.*, 2015)

$$\nabla^2_{s,\perp} W = \frac{\partial^2 W}{\partial x_s^2} + \frac{\partial^2 W}{\partial y_s^2} = 0. \tag{3.13}$$

These properties are very important for calculating the wake functions numerically and will be used later in this work. The Panofsky-Wenzel theorem, for example, is very important in three dimensional simulations because all wake-functions can be obtained only from the longitudinal electric field, because the longitudinal wake function depends only on the longitudinal electric field as pointed out by equation (3.5). Then, from equation (3.11) we have:

$$\vec{\boldsymbol{w}}_\perp = \int_{-\infty}^{z} \mathrm{d}z' \vec{\boldsymbol{\nabla}}_\perp \left(\frac{c}{qQ} \int_{-\infty}^{\infty} \mathrm{d}t E_s|_{s=ct-z'} \right). \tag{3.14}$$

3.4 The "Causality" Principle

When we take the ultra-relativistic limit, $v \to c$, all the wake fields generated by a particle can only influence particles that are behind it, no particle ahead will suffer its influence. This is equivalent to say that the wake potential must satisfy the condition

$$W(\vec{\boldsymbol{\rho}}_s, \vec{\boldsymbol{\rho}}_w, z) = 0, \ \forall \ z < 0, \tag{3.15}$$

which also directly applies to the wake functions. This condition is known in literature as causality principle and, even though it is only an approximation for the real machine, most calculations of wake functions for the ring components are performed under this assumption, including all the refined results obtained of the solutions of the ME by numeric solvers.

In appendix C we will discuss this approximation in more detail, but the general idea is that due to the fact that the direct field of an ultra-relativistic particle is in the same plane as the particle itself, the wake-fields generated by an imperfection in the vacuum chamber are created at the exact same time this particle passes through the longitudinal position where this imperfection is located. Since the particle and wake-field wave front have the same speed, the latter cannot catch up with the first.

Even though this is a good approximation for real beams stored in SLS storage rings and it generally simplifies the calculations and even possibilitates the use of specific algorithms to compute the effects on the beam[2], in this work we will not assume this approximation for any of the wakes used and all the algorithms used will work with

[2] An example is the algorithm to find the beam equilibrium longitudinal distribution developed by Bane & Ruth (1989)

causal and non-causal wakes. The main reason for this consideration is that all the raw wakes that results from the time domain solvers of the ME do not respect the causality condition[3] and there are some ocasions where their use instead of the refined results is interesting for many reasons that will be discussed in section 3.9.3. Besides, this formalism of wake functions is more general than the wake fields subject and can be applied for other sources of collective effects, such as the interaction of the beam with ions in the vacuum chamber (WANG *et al.*, 2013) or to model the effect of CSR on the beam. While the wakes of the first also respect the causality, the second is completely the opposite, being zero for particles behind the source and non-zero for particles ahead (DERBENEV *et al.*, 1995).

3.5 Expansion of the wakes

For most applications we are interested in knowing the wake-functions only very close the center of the vacuum chamber, with $\vec{\boldsymbol{\rho}}_s$ and $\vec{\boldsymbol{\rho}}_w$ much smaller than the characteristic transverse dimension of the vacuum chamber, which allow us to expand the wake potential in its transverse coordinates and keep only the low order terms

$$W(\vec{\boldsymbol{\rho}}_s, \vec{\boldsymbol{\rho}}_w, z) \approx W_0 + \vec{\boldsymbol{M}}_s \cdot \vec{\boldsymbol{\rho}}_s + \vec{\boldsymbol{M}}_w \cdot \vec{\boldsymbol{\rho}}_w + \vec{\boldsymbol{\rho}}_w^T \cdot \overleftrightarrow{\boldsymbol{D}} \cdot \vec{\boldsymbol{\rho}}_s + \vec{\boldsymbol{\rho}}_w^T \cdot \overleftrightarrow{\boldsymbol{Q}} \cdot \vec{\boldsymbol{\rho}}_w \tag{3.16}$$

where W_0, $\vec{\boldsymbol{M}}_s$, $\vec{\boldsymbol{M}}_w$, $\overleftrightarrow{\boldsymbol{D}}$ and $\overleftrightarrow{\boldsymbol{Q}}$ are coefficients of the expansion that depend only on the longitudinal position z, being $\overleftrightarrow{\boldsymbol{Q}}$ and $\overleftrightarrow{\boldsymbol{D}}$ symmetric tensors and $Q_{11} = -Q_{22}$ due to equation (3.12). Expanding the wake functions in first order we get

$$w_s \approx W_0' + \overrightarrow{\boldsymbol{M}'}_s \cdot \vec{\boldsymbol{\rho}}_s + \overrightarrow{\boldsymbol{M}'}_w \cdot \vec{\boldsymbol{\rho}}_w \tag{3.17}$$

$$\vec{\boldsymbol{w}}_\perp \approx \vec{\boldsymbol{M}}_w + \overleftrightarrow{\boldsymbol{D}} \cdot \vec{\boldsymbol{\rho}}_s + \overleftrightarrow{\boldsymbol{Q}} \cdot \vec{\boldsymbol{\rho}}_w \tag{3.18}$$

where the prime indicates derivation in respect to z.

All these components have different effects on the beam and some of them are more important than others. The component W_0' generally is the only term of the expansion of w_s that is considered in calculations because it dominates the rest of the expansion. So this term is the responsible for all the longitudinal effects on the beam, including average energy loss, potential well-distortion, hence bunch-lengthening and bunch-shortening, coupled bunch oscillations, and even energy spread increase in some cases. For this reasons, from now on, the term longitudinal wake will always refer to W_0' unless otherwise specified.

The vectors $\vec{\boldsymbol{M}}_s$ and $\vec{\boldsymbol{M}}_w$ are generally refered to as monopolar wakes, because they generate a transverse wake that is independent of the transverse displacement of the particles. The effect these wakes can cause on the beam are changes in the closed orbit as a function of the current of the ring which is a static effect and cannot lead to

[3] The motive will be discussed in the section 3.9.3

instabilities. In addition, for most practical cases these terms are zero due to symmetries in the vacuum chamber, as can be seen in appendix E.

The terms of the tensor $\overleftrightarrow{\boldsymbol{D}}$ are refered to as dipole wakes, because they are generated due to dipole displacements of the source particle. Especifically the terms D_{11} and D_{22} are called horizontal and vertical dipole wakes, respectively. They are the responsible for all the transverse instabilities that leads to coupled oscillations of the bunches, emittance deterioration and even beam loss. Besides, they can also induce coherent tune–shifts, a concept that will be studied later. These terms are dangerous because they create a mechanism for the oscillations of the source particles to induce oscillations on the witness particle and this force is always resonant because both particles have approximately the same tune. The term $D_{12} = D_{21}$ is zero in most cases due to symmetries in the vacuum chamber, but even when it is non-zero it does not induce any significant effect on the beam because, as generally the fractionary part of the horizontal and vertical tunes are different, oscillations in one plane do not drive oscillations in the other.

The coefficients Q_{11} and Q_{22} are called detuning or quadrupolar wakes because the force they induce has the same characteristics of a quadrupole. In the ultra-relativistic limit $Q_{11} = -Q_{22}$ which is the basic property of the quadrupole strengthes in the horizontal and vertical plane and, as expected from a quadrupole, they generate tune–shifts in the beam as a function of the current. The same analysis made for the coefficient D_{12} applies for the term Q_{12}.

As mentioned above, some componentes of the wake expansions are zero depending on the properties of the vacuum chamber. This is a consequence of the fact that the wake potential must preserve all the symmetries of the vacuum chamber[4]. For example, the standard vacuum chamber used in the Sirius storage ring is made of a round straight tube, which is a particular case of a cylindrical symmetry. For this type of symmetry all the components of $\overrightarrow{\boldsymbol{M}}_s$, $\overrightarrow{\boldsymbol{M}}_w$ and $\overleftrightarrow{\boldsymbol{Q}}$ must be zero and the only components of $\overleftrightarrow{\boldsymbol{D}}$ different from zero are the horizontal and vertical dipole wakes and they must be equal to each other. Thus we conclude that most of the resistive wall of the Sirius storage ring will not induce quadrupolar wakes nor any type of skew effect and that there will be no significant orbit distortions as a function of the current. Besides, considering that most of the components installed in the ring, such as bellows and Beam Position Monitors (BPMs) only slightly break this symmetry, we can expect that the behavior of the beam in the horizontal and vertical plane will be very similar, where the differences will mostly be due to assymetries in the single particle dynamics.

Taking into consideration what was discussed above, we can rewrite the expansion

[4] In appendix E there is a demonstration of how the wake potential simplifies under the most common types of symmetries of the components of accelerators.

of the wakes made in equations (3.16) and (3.17) keeping only the most important terms:

$$W(\vec{\boldsymbol{\rho}}_s, \vec{\boldsymbol{\rho}}_w, z) = W_0(z) + x_w\left(W_X^D(z)x_s - W^Q(z)x_w\right) + y_w\left(W_Y^D(z)y_s + W^Q(z)y_w\right) \tag{3.19}$$

and, consequently

$$\begin{aligned} w_s(z) &= W_0'(z) \\ w_x(x_s, x_w, z) &= W_X^D(z)x_s - W^Q(z)x_w \\ w_y(y_s, y_w, z) &= W_Y^D(z)y_s + W^Q(z)y_w \end{aligned} \tag{3.20}$$

where $W_X^D = D_{11}$, $W_Y^D = D_{22}$ and $W^Q = -Q_{22}$ and the ultra-relativistic approximation was considered.

3.6 Impedances

As already mentioned in the beginning of section 3.2 all the tools needed to model the effect of the wake fields on the beam are described in section 3.1, however it is useful to define some other concepts such as the wake functions or the wake potential because they facilitate and uniformize the process of dealing with the subject. The impedance is other one of these concepts, introduced by (VACCARO, 1966) to explain instabilities in the ISR ring at European Organization for Nuclear Research (CERN), it is proportional to the Fourier Transform of the wake functions in relation to the longitudinal coordinate, z, and is very useful in any kind of analytic calculations of instabilities or even in the determination of the wake functions. Besides due to the fact that we are interested in the effects of wake fields for storage rings which are intrinsecally periodic, the impedance reveal properties that are difficult to infer looking to the wake itself.

There are several different definitions of impedances in the literature. In this work we will adopt the definitions of the references (CHAO, 1993; STUPAKOV, 2000; HEIFETS; KHEIFETS, 1991):

$$\begin{aligned} Z_{\parallel}(\omega) &= \frac{1}{c}\int_{-\infty}^{\infty} \mathrm{d}z W_0'(z) e^{i\omega z/c} \\ Z_X^D(\omega) &= -\frac{i}{c}\int_{-\infty}^{\infty} \mathrm{d}z W_X^D(z) e^{i\omega z/c} \\ Z_Y^D(\omega) &= -\frac{i}{c}\int_{-\infty}^{\infty} \mathrm{d}z W_Y^D(z) e^{i\omega z/c} \\ Z^Q(\omega) &= -\frac{i}{c}\int_{-\infty}^{\infty} \mathrm{d}z W^Q(z) e^{i\omega z/c} \end{aligned} \tag{3.21}$$

where $Z_{\parallel} \equiv Z_s \equiv Z_L$ is the longitudinal impedance, Z_X^D and Z_Y^D are the horizontal and vertical dipole impedances and Z^Q is the quadrupole, or detuning, impedance. In other references, such as in the book of Zotter & Kheifets (1998), the impedance is the conjugate complex of the definitions presented here. The wakes can be obtained back from the impedances by the inverse transform

$$\begin{aligned} W_0'(z) &= \frac{1}{2\pi}\int_{-\infty}^{\infty} \mathrm{d}\omega Z_\parallel e^{-i\omega z/c} \\ W_t(z) &= \frac{i}{2\pi}\int_{-\infty}^{\infty} \mathrm{d}\omega Z_t e^{-i\omega z/c} \end{aligned} \tag{3.22}$$

where W_t and Z_t denotes any of the transverse wakes and impedances. Considering that the wakes are real functions, the impedances must satisfy

$$Z_\parallel(\omega) = Z_\parallel^*(-\omega) \tag{3.23a}$$

$$Z_t(\omega) = -Z_t^*(-\omega) \tag{3.23b}$$

or simply, the real part of the longitudinal impedance must be an even function of the frequency and the imaginary part must be an odd function, while for the transverses impedances the opposite is valid, the real part is odd and the imaginary part is even. Impedances have several other interesting mathematical properties, as presented in reference (CHAO, 1993). For example, when the wakes satisfy the causality condition the real and imaginary parts of the impedance are related by the Kramers-Kronig relations (KRONIG, 1926), also known as Hilbert Transforms. These other properties will be covered later in this work if they be deemed necessary for the development of the analysis.

It is interesting to note that instead of defining the impedances by the set of equations (3.21) we could have defined one generalized impedance from the wake potential

$$Z(\vec{\boldsymbol{\rho}}_s, \vec{\boldsymbol{\rho}}_w, \omega) = -\frac{i}{c}\int_{-\infty}^{\infty} \mathrm{d}z W(\vec{\boldsymbol{\rho}}_s, \vec{\boldsymbol{\rho}}_w, z) e^{i\omega z/c} \tag{3.24}$$

and the imdedances could be get from it simply by considering its expansion in the transverse coordinates:

$$Z(\vec{\boldsymbol{\rho}}_s, \vec{\boldsymbol{\rho}}_w, \omega) = \frac{c}{\omega} Z_\parallel + x_w\left(Z_X^D x_s - Z^Q x_w\right) + y_w\left(Z_Y^D y_s + Z^Q y_w\right). \tag{3.25}$$

3.7 Potential of bunches of particles

Now that all the important tools for describing the wake field effects were introduced we will calculate the change in momentum that a specific particle inside a bunch will feel due to the action of all the other particles. To do that we will assume that in the whole ring there is only one source of impedance, localized at a given point of the accelerator, and that the vacuum chamber is perfectly aligned with reference orbit of the storage ring in such a way that a particle that is on the reference orbit also is at the origin of the expansion made in equation (3.16). Regarding the longitudinal position the synchronous position will be adopted as the origin and the positions of the particles will be measured in relation to it in accordance to the definitions made in section 2.3.1, specifically in accordance with equation 2.5, where particles behind the synchronous particle have positive deviations. Under such assumptions we get:

$$V(\vec{\boldsymbol{\rho}}_i, z_i) = \sum_j W(\vec{\boldsymbol{\rho}}_j, \vec{\boldsymbol{\rho}}_i, z_i - z_j) \tag{3.26}$$

where $V(\vec{\boldsymbol{\rho}}_i, z_i)$ is denominated effective wake potential, because it is the net effect of the average of the Green wake potential over the bunch and the indices i and j are related to the witness and the source particles respectively. Notice the summation above is very difficult to evaluate for a real beam, because in every bunch there are dozens of billions of electrons, besides this sum does not evidenciate properties of the beam such as time dependency. If the beam is in equilibrium or is slowly varying the l.h.s. of equation 3.26 is approximately the same for successives turns in the ring, or over several passages by the impedance source, but each term of the r.h.s. can be very different from turn to turn which means the sum must always be carried out. For all these reasons it is important to make an approximation and consider that the effective wake potential that any particle feels is an integral over the beam distribution:

$$V(\vec{\boldsymbol{\rho}}, z, s) = \int \mathrm{d}\vec{\boldsymbol{p}} \int \mathrm{d}\vec{\boldsymbol{\rho}}' \int \mathrm{d}z' \Psi(\vec{\boldsymbol{p}}, \vec{\boldsymbol{\rho}}', z'; s) W(\vec{\boldsymbol{\rho}}', \vec{\boldsymbol{\rho}}, z - z') \tag{3.27}$$

where $\vec{\boldsymbol{p}} = (x', y', \delta)$ and $\mathrm{d}\vec{\boldsymbol{p}} = \mathrm{d}x'\mathrm{d}y'\mathrm{d}\delta$ represents the momentum coordinates and Ψ is beam density distribution function in phase space, which is time dependent in the general case.

3.7.1 Multi-turn and multi-munch effects

The equation (3.27) is not general enough to take into account all the wake field forces on the particles. In some cases the wakes persist for so long that they last for a time equivalent to several turns in the ring, acting on the same particles that generate it in successive turns. Generally these wakes are generated by cavity-like structures in the vacuum chamber that trap their electromagnetic eigen-modes for long times. In this situation we must add a sum over the distribution in previous turns

$$\begin{aligned} V(\vec{\boldsymbol{\rho}}, z, s) = \sum_{k=-\infty}^{\infty} \int \mathrm{d}\vec{\boldsymbol{p}} \int \mathrm{d}\vec{\boldsymbol{\rho}}' \int \mathrm{d}z' \Psi(\vec{\boldsymbol{p}}, \vec{\boldsymbol{\rho}}', z'; s - kL_0) \times \\ W(\vec{\boldsymbol{\rho}}', \vec{\boldsymbol{\rho}}, z - z' + kcL_0) \end{aligned} \tag{3.28}$$

where the sum can be extended to infinity because the wake-potential is zero for relative positions between the source and the witness when there is no interaction between them. For example it would not make sense for a particle feel the wake field it will generate in the next turn, this means the wake potential must be zero for large negative values of

$z - z'$. Yet, in the most general case there is more than one bunch stored in the ring, which means it is also necessary to take the influence of other bunches into account

$$V_n(\vec{\boldsymbol{\rho}}, z, s) = \sum_{l\in\mathscr{B}} \frac{I_l}{\langle I\rangle} \sum_{k=-\infty}^{\infty} \int \mathrm{d}\vec{\boldsymbol{p}} \int \mathrm{d}\vec{\boldsymbol{\rho}}' \int \mathrm{d}z' \Psi_l(\vec{\boldsymbol{p}}, \vec{\boldsymbol{\rho}}', z'; s - s_r) \times \\ W(\vec{\boldsymbol{\rho}}', \vec{\boldsymbol{\rho}}, z - z' + s_r) \tag{3.29}$$

where

$$s_r = kL_0 - (s_l - s_n) \tag{3.30}$$

is the retarded position defining when the wakes were generated, I_l is the current and s_l is the synchrotron position of the l-th bunch in the ring, $\langle I\rangle = \sum_{l\in\mathscr{B}} I_l/M$ is the average current per bunch and $\mathscr{B}$ is a set of integer numbers to identify which bunchs are filled with particles. For example, if the bunches $1, 10, 500$ and 735 are filled and the rest is empty, then $\mathscr{B} = \{1, 10, 500, 735\}$ and for sure $n \in \mathscr{B}$. Also V_n needs the subscript n in order to identify it as the wake potential felt by the n-th bunch in the ring.

Combining equation (3.29) with the expansion of equation (3.20) we can derive expressions for each component of the effective wake functions of the beam

$$(V_0)_n(z, s) = \sum_{l\in\mathscr{B}} \frac{I_l}{\langle I\rangle} \sum_{k=-\infty}^{\infty} \int \mathrm{d}z' \lambda_l(z'; s - s_r) W_0'(z - z' + s_r) \tag{3.31a}$$

$$(V_X^Q)_n(x, z, s) = x \sum_{l\in\mathscr{B}} \frac{I_l}{\langle I\rangle} \sum_{k=-\infty}^{\infty} \int \mathrm{d}z' \lambda_l(z'; s - s_r) W^Q(z - z' + s_r) \tag{3.31b}$$

$$(V_X^D)_n(z, s) = \sum_{l\in\mathscr{B}} \frac{I_l}{\langle I\rangle} \sum_{k=-\infty}^{\infty} \int \mathrm{d}z' d_l(z'; s - s_r) W_X^D(z - z' + s_r) \tag{3.31c}$$

where λ_l is the longitudinal line distribution and d_l is the horizontal dipole moment of the l-th bunch defined by

$$\lambda_l(z; s) = \int \mathrm{d}\vec{\boldsymbol{p}} \int \mathrm{d}\vec{\boldsymbol{\rho}}' \Psi_l(\vec{\boldsymbol{p}}, \vec{\boldsymbol{\rho}}', z; s) \tag{3.32}$$

$$d_l(z; s) = \int \mathrm{d}\vec{\boldsymbol{p}} \int \mathrm{d}\vec{\boldsymbol{\rho}}' x \Psi_l(\vec{\boldsymbol{p}}, \vec{\boldsymbol{\rho}}', z; s) \tag{3.33}$$

and V_0, V_X^D and V_X^Q are the effective longitudinal, horizontal dipole and horizontal detuning wake functions of the bunch. The expressions for the vertical effective wakes V_Y^D and V_Y^Q are very similar to the horizontal ones, just changing x for y.

3.7.2 Relation with Impedance

In order to demonstrate how the concept of impedance is useful in the calculations of beam dynamics and its interpretation lets consider the beam is stationary, which means the distribution does not depend on time, and that all bunches in the ring are identical and equally spaced. When we apply the last assumption to equation (3.31a) we notice the double sum can be replaced by a single one, if we define a variable

$$j = kM + l - n$$

where M is the number of bunches stored in the ring. This way the sum reads

$$V_0(z) = \sum_{j=-\infty}^{\infty} \int \mathrm{d}z' \lambda(z') W_0'(z - z' + jc\frac{T_0}{M}). \tag{3.34}$$

where the symbols l and n can be dropped due to the symmetry among bunches and the potential is time-independent. Additionally, if we substitute the wake function by its representation in terms of the impedace given in equation (3.22) the equation above becomes

$$V_0(z) = \frac{1}{2\pi} \sum_{j=-\infty}^{\infty} \int \mathrm{d}\omega \tilde{\lambda}(\omega) Z_{\parallel}(\omega) e^{-i\omega(z/c + j\frac{T_0}{M})} \tag{3.35}$$

where the line density $\lambda(z')$ was also substituted by its Fourier Transform, defined as

$$\tilde{\lambda}(\omega) = \int_{-\infty}^{\infty} \mathrm{d}z \lambda(z) e^{i\omega z/c}. \tag{3.36}$$

Finally, using the Fourier Series expansion of the delta combo:

$$\sum_{p=-\infty}^{\infty} \delta(\omega - pM\omega_0) = \frac{1}{M\omega_0} \sum_{j=-\infty}^{\infty} e^{-i2\pi j \frac{\omega}{M\omega_0}} = \frac{1}{M\omega_0} \sum_{j=-\infty}^{\infty} e^{-i\omega(j\frac{T_0}{M})}, \tag{3.37}$$

where $\omega_0 = {}^{2\pi}\!/_{T_0}$ is the angular revolution frequency of the ring, equation (3.35) can be written as

$$V_0(z) = \frac{M\omega_0}{2\pi} \sum_{p=-\infty}^{\infty} \tilde{\lambda}(pM\omega_0) Z_{\parallel}(pM\omega_0) e^{-ipM\omega_0 z/c}. \tag{3.38}$$

where we notice the beam will only sample the impedance at multiples of the revolution frequency. Similar expressions can be obtained for the dipole and quadrupole effective wake functions:

$$V_X^D(z) = -\frac{iM\omega_0}{2\pi} \sum_{p=-\infty}^{\infty} \tilde{d}(pM\omega_0) Z_X^D(pM\omega_0) e^{-ipM\omega_0 z/c} \tag{3.39a}$$

$$V_X^Q(x, z) = -x\frac{iM\omega_0}{2\pi} \sum_{p=-\infty}^{\infty} \tilde{\lambda}(pM\omega_0) Z^Q(pM\omega_0) e^{-ipM\omega_0 z/c} \tag{3.39b}$$

and analogously to the vertical plane. Notice in the equations above that the dipole impedance does not generate any effective wake function if the beam is stable and well centered in the vacuum chamber, because in this condition the dipole moment of the beam is zero. This is the main characteristic of a coherent mechanism, it depends on the values of specific properties of the beam, in this case the longitudinal distribution of the dipole moment, and its effects are only visible through averages on the distribution.

On the other hand, the detuning wake generates a z-dependent quadrupole strength on individual particles of the beam even if the beam is stationary, which is a the characterist of an incoherent effect, it affects the intra-bunch dynamics but not necessarely is reflected in the averages on the distribution.

Equation (3.38) describes the meaning behind the concept of impedance and its analogy with an electric circuit impedance. Notice that the equation can be interpreted as the Fourier expansion of the wake in the interval T_0/M and the coefficient that multiplies the exponential in the sum is the Fourier component of this expansion

$$\tilde{V}_0 = \tilde{\lambda} Z_{\|}, \tag{3.40}$$

where $\tilde{\lambda}$ is the analog of the current in a circuit and $\tilde{V}_0$ is the voltage induced by this current. The same analogy can be extended to the impedance in other planes. Actually, the modeling of the vaccum chamber as a circuit is a resource widely used to model the low frequency part of the impedance (SESSLER; VACCARO, 1967; ZOTTER; KHEIFETS, 1998; DAVINO; HAHN, 2003).

3.8 Models for Impedances and Wakes

Even though the impedances and wake functions of each component in the ring is a result of a complex interaction between a particle and its environment, they often can be represented by simple physical models. A good example that is widely used, either to model the interaction of the beam with a trapped mode of a RF cavity, as described by Zotter & Kheifets (1998, Appendix 1.B), or to represent the whole impedance budget of a storage ring, is the resonator impedance, given by the RLC circuit in parallel

$$\frac{1}{Z_{\|}} = \frac{1}{R_s} + \frac{i}{\omega L} - i\omega C \Rightarrow Z_{\|} = \frac{R_s}{1 + Q\left(\frac{\omega_R}{\omega} - \frac{\omega}{\omega_R}\right)} \tag{3.41}$$

where R_s is called the shunt resistence of the cavity, $Q = R_s\sqrt{C/L}$ is the quality factor, $\omega_R = 1/\sqrt{LC}$ is the resonant frequency and L and C are the inductance and the capacitance. The wake function associated with this impedance is given by the damped harmonic oscillator

$$W_0'(z) = \begin{cases} 0 & z > 0 \\ \alpha R_s & z = 0 \\ 2\alpha R_s e^{-\alpha z/c}\left(\cos\left(\frac{\bar{\omega}_R z}{c}\right) - \frac{\alpha}{\bar{\omega}_R}\sin\left(\frac{\bar{\omega}_R z}{c}\right)\right) & z > 0 \end{cases}, \tag{3.42}$$

where $\alpha = \omega_R/2Q$ is the damping factor and $\bar{\omega}_R = \sqrt{\omega_R^2 - \alpha^2}$. Note that when Q is large the damping factor is small and the wake rings for several periods, extending to large distances z behind the source particle. Such type of wakes are called narrow–band, because in the frequency domain the impedance has a sharp peak around the resonant frequency, with maximum amplitude equal to R_s. In the context of a storage ring, where several bunches are stored in the machine, wakes like this, generated by one bunch can last long enough to influence other bunches behind it or even itself in the next turns, if the resonance condition between the spacing between sequential bunches and the wake period is approximately met. On the other hand, if Q is small, generally close to one, the damping factor is large and the wake goes to zero fast. This type of resonator is called broad band resonator (BBR), because its impedance has a very wide spectrum.

Considering the calculations made in section 3.7.1, which considered the periodicity of the ring in the effective wakes calculation, expressed by the infinite sum in equations (3.31), the narrow–band wakes sample only a few of those lines, being negligible for the rest of the sum. This is a result of the multi–turn build up of the electromagnetic fields in the device that generates the impedance. When the wake is broad–band, the impedance does not change much from successive lines in the summation, in such a way that the sum can be replaced by an integral, and the whole information regarding the periodicity of the system is lost, because the interaction is only monentarely. The reasonings above suggest the definition of narrow and broad–band depend on the size of the ring and, more specifically on the bunch spacing.

3.8.1 circuit components

3.8.1.1 Inductive

3.8.1.2 Capacitive

3.8.1.3 Resistive

3.9 Impedance Calculation

For most practical cases, determining the impedance of a given component of the storage ring is a very difficult task because of the complexity of the boundary conditions involved. The exact analytic solution of the ME can only be performed for a limited number of cases, and even in this cases some idealizations of the real system must be performed. In order to tackle this problem the accelerator physics community resorts to all possible ways of finding approximate results and all these efforts can be grouped in two categories, the analytic treatments and the numeric solutions.

An adequate description of the analytic methods for finding such solutions is far beyond the current competencies of the author and the scope of this work. At this point we strongly recommend the book written by Zotter & Kheifets (1998) and the report written by Gluckstern (2000) for the interested reader. Besides, Chao (1993) and Palumbo *et al.* (1994) also discuss some of the approximate methods in a very intuitive way; and Ng

& Bane (2010) presents a table with some of the most important results for common types of accelerator structures. Not covered in any of these references is the explanation of the use of the parabolic equation, which is a paraxial approximation of the ME, to the impedances calculation, presented by Stupakov (2006). From these equations it can be shown that the wakes must satisfy a very interesting scaling feature that is very useful for numeric simulations (STUPAKOV *et al.*, 2011).

Most analytic methods are employed in frequency domain, which means the result of the calculation is an expression for the impedance, not the wake. This expression generally is valid for a certain range of frequencies and the most common type of approximations consider frequencies much lower than the cutoff frequency[5] of the pipe ($\omega \sim 2.4c/b$) or very high frequencies. While the first kind of approximations are valid for bunches longer than the characteristic transverse dimension of structure, the latter is a good approximation for very short bunches.

In the case of Sirius, the standard vacuum chamber has a radius of 12 mm while the bunch will have approximately 3 mm. This combination of dimensions is delicate because the bunch is not long enough for the low frequency approximations to be valid nor short enough for the high frequency regime to dominate, which means we cannot rely only on these methods to compose the Sirius Impedance budget.

Bellow we will describe two cases of analytical calculation of impedances of fundamental importance to this work: the first is the tapered transition, which is an example of the arguments presented above, which indicates that numerical solvers are the most accurate way of calculating impedances, and the other is the resistive wall, which is a big exception to this rule. Finally, we will introduce the main concepts important for numerical simulations.

3.9.1 Tapered Transitions

Some components in a storage ring require transverse apertures that are different from the standard vacuum chamber. For example, undulators need narrower chambers because their magnetic gap is small to achieve larger fields and improve the radiation quality. The beam ports of the RF cavities, on the other hand, are larger than the standard pipe. These two types of structures in the vacuum chamber are called collimators[6] and cavities, respectively, and have a strong impact on the total impedance budget of a storage ring, mainly in the transverse plane. See for example a paper by Günzel (2006) which describes the impedance budget of the ESRF storage ring or another work of the same author, Günzel & Perez (2008), where the impedance budget of ALBA is analysed.

[5] Cutoff frequency is the frequency of the lowest eigen-mode of the pipe, above which the fields can propagate through the tube.

[6] Actually there is a device called collimator which have the same concave geometry of the pairs of transtions defined with this name here. Their function is to screen the transverse tail of the beam.

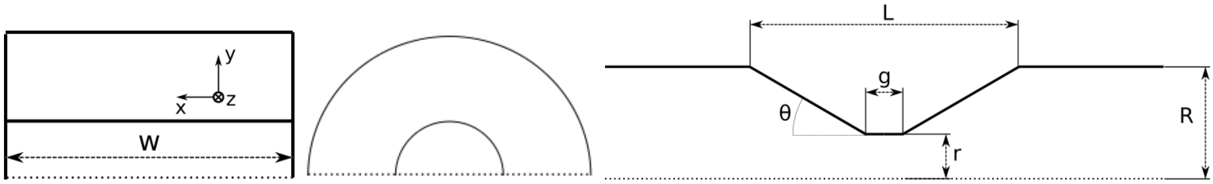

(a) Flat transition. (b) Round transition. (c) Scheme of a tapered transition.

Figure 10 – When $r > R$ the element is called cavity and when $r < R$ it is called collimator. The tapers are the slow transitions of the chamber, region where the radius varys. When the transition has no tapers it are called step–in or step–out, depending on the relation between the initial and final radius.

Figure 10c shows a scheme of such type of geometry, with the important parameters for the impedance calculation. Such geometry can be separated in two independent contributions from the two cross section variations if the gap, g, is large, according to Bane *et al.* (2007). As discussed by Heifets & Kheifets (1991), when the beam passes through the transitions two forces act on it: one from the change of the energy stored in the synchronous component of the field that travels with the beam, Z_s, originated due to the difference in the cross sections, and another one due to the radiation emitted by the image charges on the wall, Z_r,

$$Z_0^{\text{out}} = Z_r + Z_s \tag{3.43a}$$

$$Z_0^{\text{in}} = Z_r - Z_s \tag{3.43b}$$

where Z_0^{out} is the total impedance of the transition where the beam goes from a smaller chamber to a larger one (step–out), Z_0^{in} is the impedance from a larger chamber to a smaller one (step–in) and the equality of the terms Z_r in both cases is a consequence of the beautiful theorem of directional symmetry of the impedance, demonstrated by Heifets (1990). The term Z_s is constant regardless of the frequency and tapering of the transition, and causes energy gain in the step–in case and energy loss for the step–out. For a transition with round cross–section this contribution to the impedance is given, according to Palumbo *et al.* (1994), by

$$Z_s \approx \frac{Z_0}{2\pi} \ln\left(\frac{r_1}{r_2}\right), \tag{3.44}$$

where $Z_0 = 120\pi\ \Omega$ is the impedance of free space and r_1 and r_2 are the radia of the chamber before and after the transition, respectively. Besides, for the step–in case the total energy loss by the beam must be approximately zero, $Z_0^{\text{in}} \approx 0$, because the radiation emitted propagates in the opposite direction of the beam. This means that all the energy of the radiation must be taken from the synchronous field, which yelds that in the high frequency limit $Z_r = Z_s$.

Notice that the average influence of the source term, Z_s, on the impedance in one turn around the ring is zero, because of the periodicity of the vacuum chamber.

Thus, the term that really matters is the contribution of the radiation, which depends on the characteristics of the transition, such as the tapering. Analytical studies of this component were carried out by Yokoya (1990) for a round geometry (Figure 10b), where the author derived expressions for the low frequency range of smoothly varying tapered transitions. Later Stupakov (1996) corrected the upper frequency limit of the validity of these expressions and extended the lower limit to zero frequency. The result is the follwing:

$$\frac{\omega r^2}{cl} \ll 1: \qquad Z_{\parallel} = -\frac{i\omega Z_0}{4\pi c}\int_{-\infty}^{\infty} \mathrm{d}z\,(r')^2, \qquad Z_t = -\frac{iZ_0}{2\pi}\int_{-\infty}^{\infty} \mathrm{d}z \left(\frac{r'}{r}\right)^2, \tag{3.45}$$

where $r = r(z)$ is the radius of the chamber, $r' = r'(z)$ is the derivative of the radius and $l = (L - g)/2$ is the taper length. Note that this impedance is imaginary while the the one from the high frequency limit is real. This happens because below the cutoff frequency of the chamber, no radiation can propagate, what suggests that above this threshold a real part of the impedance will arise and, after a complex frequency range where the transition between the two limiting behaviors dominates, the imaginary part will tend to zero and the real one will approach the high frequency limit. Another feature of the equation above is that we notice the impedance tends to zero with the taper length. For example, for a linear taper the formulas above simplifies to

$$\frac{\omega r^2}{cl} \ll 1: \qquad Z_{\parallel} = -\frac{i\omega Z_0}{4\pi c}\frac{|r_1 - r_2|}{t}, \qquad Z_t = -\frac{iZ_0}{2\pi}\frac{|r_1 - r_2|}{t r_1 r_2}, \tag{3.46}$$

where $t = \tan^{-1}\theta = l/|r_1 - r_2|$ is the transition factor of the taper.

Stupakov (2007) developed a method to find the low frequency impedance of tapers with general cross sections and derived explicit formulas for a flat taper, consisting on a rectangular geometry with varying vertical gap and constant horizontal apperture, as shown in Figure 10a. His results were:

$$\frac{\omega w^2}{2cth} \ll 1 \text{ and } h \ll w \ll l: \quad \begin{aligned} Z_{\parallel} &= -0.43\frac{i\omega Z_0}{\pi c}\int_{-\infty}^{\infty}\mathrm{d}z(h')^2 \\ Z_y &= -\frac{iZ_0 w}{4}\int_{-\infty}^{\infty}\mathrm{d}z\frac{(h')^2}{h^3} \\ Z_x^D &= -Z_x^Q = -\frac{iZ_0}{4\pi}\int_{-\infty}^{\infty}\mathrm{d}z\left(\frac{h'}{h}\right)^2 \end{aligned} \quad , \tag{3.47a}$$

where w is the chamber half–width and $h(z)$ is the half–gap. It is worth noting that the dipole horizontal and the quadrupolar impedances are equal to each other and a factor of 2 smaller than the transverse impedance in a conical taper, while the longitudinal impedance is $\approx 7/4$ of its counterpart. The most interesting result, however, is the linear dependence of the vertical dipole impedance with the width of the chamber, which makes this impedance $\approx \pi/2w/\langle h\rangle_{\mathrm{harm}}$ larger than the round chamber one. For example, for a linear taper these expressions become

$$\frac{\omega w^2}{2cth} \ll 1 \text{ and } h \ll w \ll l: \quad \begin{aligned} Z_\parallel &= -0.43\frac{i\omega Z_0}{\pi c}\frac{|h_1-h_2|}{t}, \\ Z_y &= -\frac{iZ_0}{2}\frac{w}{t}\frac{(h_1+h_2)|h_1-h_2|}{h_1^2h_2^2}, \\ Z_x^D = -Z_x^Q &= -\frac{iZ_0}{4\pi}\frac{|h_1-h_2|}{th_1h_2}, \end{aligned} \tag{3.48}$$

where we note that $Z_y^{\text{flat}}/Z_y^{\text{round}} = \pi w(h_1+h_2)/(h_1h_2)$.

Podobedov & Krinsky (2007) studied the low frequency limit of confocal[7] elliptical transitions and found results very similar than the expressions above for the flat geometry, which gives some confidence in trying to extend the qualitative results discussed here for approximated geometries.

Even though the low frequency impedance of long and short collimators and cavities are the same, because the equations showed above can be applied on both limits, Heifets (1990) found different limits for the high frequency impedances of a round cavity, depending on the length of their gap. Besides, Stupakov *et al.* (2007) found equal limit values for the longitudinal impedance, but different for the transverse dipole impedance in a round collimator. While for the longitudinal limit the value is two times the quantity in equation (3.44), for the transverse plane they found

$$\text{short:} \qquad Z_x^D = \frac{Z_0 c}{2\pi\omega r^2}\left(1-\frac{r^4}{R^4}\right) \text{long:} \qquad Z_x^D = \frac{Z_0 c}{\pi\omega R^2}\left(1-\frac{R^4}{r^4}\right) \tag{3.49}$$

where the notation of Figure 10c was used. Besides, there is a very large frequency gap between the two limiting cases that are of great importance, mainly for storage rings such as Sirius, which have bunches with length that samples these frequencies. For the round collimator, Stupakov & Podobedov (2010) used the parabolic equation to calculate the impedance from a few dozens of GHz up to a few THz, with excellent agreement with ECHO results. However for other geometries, or even the detailed behavior of the impedance for the round transitions can only be accessed with the aid of numerical solvers.

For example, Blednykh (2006) studied the impedance of the collimator–type flat chamber of a mini–gap undulator and found very intense narrow–band mode just above the cutoff of the pipe, that depended very strongly on the width of the cross–section. For all these reasons the formulas studied here, even though are very useful to the study of this type of impedance and qualitative analysis of the relevant parameters for impedance optimization, will not be used to quantitatively for any device of the impedance budget.

[7] Confocal ellipses means they have the same foci. In the case of the transition cited here, the equation $a^2(z_1) - b^2(z_1) = a^2(z_2) - b^2(z_2)$ is valid for any longitudinal position z_1 and z_2, where a and b are the larger and smaller axes of the ellipse.

3.9.2 Multi-Layer Resistive Wall

The standard resistive wall effect is known for a long time, being first observed to generate coherent oscillations in electron streams coupled to circuits by Pierce (1951) and then used to create a resistive-wall amplifier by Birdsall *et al.* (1953). This idea was first applied to the study of collective effects in accelerators by Neil & Sessler (1965) and Laslett *et al.* (1965) to explain longitudinal and transverse coherent oscillations of coasting beams and then by Courant & Sessler (1966) to describe instabilities of bunched beams. Since then the theory for calculation of the now called resistive-wall impedance evolved (CHAO, 1993), being exactly solved by Bane (1991) for a round and infinitely thick and long vacuum chamber, where the author provided analytic formulas for the short-range wake-fields, and for an arbitrary transverse cross section by Yokoya (1993), who based its work on a formalism developed by Gluckstern *et al.* (1993). In his work, YOKOYA also showed that the spectral dependency of the longitudinal and transverse dipole and quadrupole impedances of elliptic chambers with different eccentricities but equal smaller radius are identical, in such a way that their wake functions differ from each other only by a constant factor. In the special cases of a round and a flat chamber, which are the limiting cases of an ellipse, with eccentricities equal to 0 and 1 respectively, the so called YOKOYA factors are given by

$$\left(Z_\parallel\right)_{\text{flat}} = \left(Z_\parallel\right)_{\text{round}} \tag{3.50}$$

$$\left(Z_x^D\right)_{\text{flat}} = \frac{\pi^2}{24}\left(Z_x^D\right)_{\text{round}} \tag{3.51}$$

$$\left(Z_y^D\right)_{\text{flat}} = \frac{\pi^2}{12}\left(Z_x^D\right)_{\text{round}} \tag{3.52}$$

$$\left(Z^Q\right)_{\text{flat}} = \frac{\pi^2}{24}\left(Z_x^D\right)_{\text{round}}, \tag{3.53}$$

where we notice the net horizontal force felt by the witness particle with the same horizontal position as the source particle is zero. Actually, this is a particular case of the general result that the wake potential of this structure must not depend individually on the horizontal positions of the source and witness particles, but only on their difference

$$W_{\text{flat}}(x_s, y_s, x_w, y_w, z) = W_{\text{flat}}(y_s, y_w, x_s - x_w, z),$$

to respect the condition of translational symmetry in the horizontal direction.

It is very recurrent in accelerators to have chambers that are composed of different laminar layers of materials. For example, the chambers of fast time-varying magnets, such as the injection kickers of a storage ring, must be made of a bad conductor, generally a ceramic. To avoid discontinuities in the path of the image current of the beam[8], which could lead to excessive heating and consequent melting or burning of the magnet components and the accumulation of static charges in the ceramic, a thin layer of metal is

[8] This is equivalent to say: "to decrease the impedance of the beam".

deposited, coated, in the inner surface of the chamber. The thickness of the coating must be of a few microns: thin enough to not distort the external field as it penetrates the walls, which has frequencies of the order of hundreds of kilo Hertz, and thick enough to shield most of the frequencies of the beam, which extend to a few dozens of giga Hertz. Especifically for the kicker magnet, outside the ceramic vacuum chamber there is a layer of ferrite, which is used to guide the external field of the kicker. In the low frequency part of the spectrum, all these different layers of materials are seen by the self fields of the beam and contribute to the impedance.

Besides, the multi-layer chamber also appear in the simple case of a standard vacuum chamber of an accelerator, where the finite thickness of wall can be interpreted as a multi-layer chamber composed of metal and air. This finite thickness of the metal strongly influences the low frequency part of the impedance because the skin depth of the fields becomes much larger than the thickness of the chamber and the losses diminishe, which causes the real part of the impedance to go to zero and the imaginary part to a constant value as the frequency tends to zero, while the infinitely thick formula predicts that both impedances diverge to plus and minus infinity, respectively, when the same limit is taken. This low frequency of the resistive wall has a very narrow band nature and influences the long range wake fields, which are directly related to the coupled bunch resistive wall instability and the incoherent tune–shifts caused by chambers without circular symmetry, as explained by Chao *et al.* (2002).

The multi-layer chambers problem was first tackled by Zotter (1969a), who created an algorithm that solved the problem for an arbitrary number of layers of materials with arbitrary electric and magnetic properties, as long as they were linear, homogeneous and isotropic (ZOTTER, 1969a; ZOTTER, 1969b; ZOTTER, 1970). Even though his method was general enough to be applied to any azimuthal mode m of the source, he only calculated the fields for the azimuthal modes $m = 0$ and $m = 1$[9]. This allowed him to derive explicit analytical formulas, under some approximations, for the longitudinal impedance of simplified configurations, such as a single wall with finite thickness, and a metallized ceramic chamber sorrounded by a PEC, where the author noticed the effectiveness of the coating in the inner wall was much higher than what is intuitively thought by comparing the thickness of the coating with the skin depth of the fields for a given frequency.

Later Piwinski (1977) calculated the impedance generated by a gaussian bunch in a four-layer round chamber composed of metal, ceramic, ferrite and PEC, respectively, and confirmed what Zotter (1970) had previously found, that for this type of multi-layer

[9] It is remarkable that his method goes beyond the rigid beam approximation, considering the source of the wake fields as an infinitely long beam oscilating in the transverse plane to calculate the mode $m = 1$.

chambers, the fields will not penetrate through the coating if its thickness, t, satisfies

$$t > \frac{\delta^2}{d}, \quad \text{with} \quad \delta = \sqrt{\frac{2}{\mu_0 \omega \sigma_c}} \tag{3.54}$$

where δ is the skin depth and σ_c is the conductivity of the coating, μ_0 is the magnetic permeability of vacuum, ω is the angular frequency of the fields and d is the thickness of the ceramic. This means that, since generally $d \gg t$, the coating is efficient down to frequencies much lower than what is intuitively thought.

In a more recent work, Zotter (2005) rederived his formalism for a point like charge, which was used by Mounet & Métral (2009) to derive formulas for the electromagnetic fields and impedances for any azimuthal mode m, under the assumption of a rigid beam. Later, the same authors also derived expressions for a multi-layer flat chamber with possible different layers in the top and bottom plates (MOUNET; MÉTRAL, 2010a) which allowed them to generalize the YOKOYA factors (MOUNET; MÉTRAL, 2010b). Then, in his PhD thesis, Mounet (2012) developed a general method to compute Fourier Integrals which allowed him to compute the exact wake functions for short and long range using the impedances. All these developments in 2D impedance theory were implemented by MOUNET in a code called ImpedanceWake2D that is available free-of-charge for the accelerators community. It is important to mention that other authors also solved the problem of multi-layer impedances using different methods, for example Hahn (2008) and Al-Khateeb *et al.* (2005) also derived general methods valid for arbitrary energies and frequencies in round chambers and Burov & Lebedev (2002a), Burov & Lebedev (2002b) also solved the problem under the assumption of long wavelengths, $c/\omega \ll a$, for round and flat geometries.

In summary, the theory of smooth multi-layer infinitely long round chambers is completely solved. In this work we implemented MOUNET; MÉTRAL formulas to calculate the impedances for round chambers for the azimuthal modes $m = 0$ and $m = 1$ in Matlab®and Python3 and the wake functions were obtained using the code ImpedanceWake2D. In cases where the eccentricity of the chamber is large, the YOKOYA Factors are applied to the round chamber results.

3.9.3 Numeric Methods

The numerical solvers can be grouped in two categories, the frequency domain codes, that are more indicated for calculation of resonant modes below the cutoff of the chamber, and the time domain solvers. While the first class computes the eigen-values and eigen-modes of the structures and the user must identify which ones can be excited by the beam passage, the latter solves ME computing directly the fields that are generated by the beam. In this type of solvers the beam is modeled by a line density of charge, λ, that traverses the structure at the speed of light with a constant transverse displacement,

$\vec{\boldsymbol{\rho}}'_0$, and then, by discretization of the space-time in grids and approximations of the derivatives by linear operators on the fields in the vertices and faces of each grid, the electromagnetic field can be calculated up to the desired distance behind the source, so the integral defined in equation (3.4) can be carried out. Depending on the methods employed in the discretization and the properties of the linear operators in each grid, different convergencies of the solutions in relation to the number and size of the grids can be achieved. There are several different methods and codes in the literature dedicated to this purpose. For a good review on numeric methods it is recommended Niedermayer & Gjonaj (2016) and its references.

3.9.3.1 Finite Line Density Issue

This procedure employed to find the impedances has an intrinsic limitation: the line density used as source particle in simulations must allways spread over a few grids, which means a delta-like function can never be used and the wake functions, or wake potential, cannot be obtained. Instead, the effective wake potencial, given by

$$V(\vec{\boldsymbol{\rho}}'_0, \vec{\boldsymbol{\rho}}, z) = \int \mathrm{d}z' \lambda(z') W(\vec{\boldsymbol{\rho}}'_0, \vec{\boldsymbol{\rho}}, z - z'), \tag{3.55}$$

is the result of the simulations. In principle this equation could be inverted with the aid of the convolution theorem (Wikipedia Contributors, 2017c), where after the Fourier Transform on both sides of the equation one could get

$$\tilde{W} = \frac{\tilde{V}}{\tilde{\lambda}}. \tag{3.56}$$

However, this procedure fails to give the values of the impedance at large frequencies due to two effects: the most obvious is the limitations imposed by the Nyquist theorem applied to the grid length of the simulation and the other comes from the fact that the line density Fourier transform has a tail at large frequencies that makes the denominator of equation (3.56) very small, which, in turn, increases the effect of the noise of the simulations for this frequency range. This limitation on the knowledge of the impedance for high frequencies makes it not possible to obtain the wake function accurately for short distances from the source.

The line density generally used for such calculations is the Gaussian distribution:

$$\lambda(z) = \frac{1}{\sigma\sqrt{2\pi}} \exp\left(-\frac{(z - n\sigma)^2}{2\sigma^2}\right) \tag{3.57}$$

due to its minimal duration-bandwidth product (NIEDERMAYER; GJONAJ, 2016). A rule of thumb for these calculations is to consider the impedance only up to frequencies $\omega <= 2\sigma/c$ to avoid strong influences of the numerical noises as discussed above, which is much more limiting that the Nyquist requirement, given that in simulations the bunch length must be at least five times larger than the grid size.

The authors Podobedov & Stupakov (2013) found a way to overcome this problem, as long as the bunch length used in the simulation is short enough. However, a more practical approach comes from the fact that a real bunch also has a finite length and cannot excite wakes with arbitrarely large frequencies, which means if the line density used to obtain the wakes is smaller than the smallest longitudinal structure in the bunch expected to generate any macroscopic significant effect we want to study, than the impedance extracted from that simulation is enough. Notice this method is intrinsically non-consistent, because we must know *a priori* how the beam will behave to compute the impedance that will drive this behavior. However, the knowlegde gathered by the accelerator physics community in the last fifty years, through several experiments and confrontation of these results with simulated and analytic calculated beam dynamics, led to some rules of thumb that determines the maximum frequency can be expected to influence the dynamics of a bunch, given its natural bunch length.

This approach may be conflicting in some situations when the high frequency content of the wake is desired but the structure being analysed has strong resonant modes that take hundreads of meters behind the source to damp. Running a simulation with a short line density will drastically increase the time of the simulation because of the smaller mesh size. The solution for these cases is to run two simulations, one with a short bunch and small wake length and other with a longer bunch and long wake length, to characterize the resonant mode. Another approach would be to simulate the resonant modes with a frequency domain code.

3.9.3.2 ECHO Code

There are some solvers in the literature that were developed specifically for rotationally symmetric geometries, such as ABCI (CHIN, 1994), due to the high recurrency of this type of structure in accelerators. In this type of systems the wake potential in the ultra-relativistic approximation can be partially solved without the need of specifying the BC, only by the application of the Panofsky-Wenzel theorem and equation (3.12). It can be shown (STUPAKOV, 2000) that the most general form for the wake potential in such conditions is:

$$W(\rho_s, \rho_w, \theta, z) = \sum_{m=0}^{\infty} W_m(z)\rho_w^m \rho_s^m \cos(m\theta) \tag{3.58}$$

where $\rho = |\vec{\boldsymbol{\rho}}|$ is the distance of the particles to the center of the chamber, θ is the angle between the the source and the witness particles and it was assumed the source particle is in the $\hat{\boldsymbol{x}}$ direction. The wake functions can be obtained from the gradient of the wake potential. Expanding the wake functions in the leading order we notice

$$w_s(z) \approx W_0'(z) \tag{3.59}$$

$$\vec{\boldsymbol{w}}_t(x_s, z) \approx W_1\rho_s(\hat{\boldsymbol{r}}\cos(\theta) - \hat{\boldsymbol{\theta}}\sin(\theta)) = W_1 x\hat{\boldsymbol{x}} \tag{3.60}$$

where we notice the force is in the same direction of the displacement of the source particle.

This partial solution of the wake potential allow us to solve each azimuthal component of the wake potential separatelly, which implies the numerical solution can be found for a single plane of the structure, for example, the plane $x-s$, or $y = 0$. This bidimensional mesh drastically reduces the simulation time for such components and this class of codes are called 2D solvers. Among such codes we highlight ECHOz1 and ECHOz2 (ZAGORODNOV *et al.*, 2003; ZAGORODNOV; WEILAND, 2005; ZAGORODNOV, 2006), which are distributed free of charge by the author. While ECHOz1 calculates only the azimuthal mode $m = 0$, ECHOz2 provides the longitudinal and transverse wake functions for an arbitrary mode m. This code employes several solutions to common problems of numeric simulations that makes it the state of the art for impedances calculation. Among the advantages of this code we highlight:

- zero dispersion in the longitudinal plane, which is a numeric effect that introduces a non-physical dependency of the phase velocity of the electromagnetic waves with their frequency, which deteriorates the precision of the wakes;
- fast convergence of the relation bunch size over grid length, σ/h: in other codes this ratio must be one order of magnitude larger than ECHO's for the results to have the same precision. In ECHO a ratio of 5 already gives convergent results, which greatly reduces the simulation time for a given frequency requirement on the knowlegde of the impedance;
- moving mesh: instead of discretize the whole structure, the grids move with the source and this region extends behind it only down to the desired length of the wake. This approach helps reducing the simulation time in cases where the structure is larger than the wake length and is applied in other codes too, such as GdfidL;
- indirect integration: for the wake calculation, the infinite integral in the longitudinal direction can be substituted by finite integrals in closed contorns that spans the structure longitudinally. The first method proposed by Weiland (1983) was valid only for cavity-like structures, but then it was generalized for any rotationally symmetric structure by Napoly *et al.* (1993) and finally generalized for any 3D structure by Zagorodnov (2006). This procedure greatly reduces the computational time because otherwise it would be necessary to propagate the beam for a very long distance only for the integral to converge. Besides, it improves the precision of the results, because the long integral in the direct method suffers from numerical errors accumulation.

There is another code provided by the same author, ECHOzR, that calculates the wakes for structures with rectangular cross sections (ZAGORODNOV *et al.*, 2015). The conditions imposed on the geometry are that the lateral walls are composed of infinite vertical and perfectly conducting parallel plates displaced one from another by a distance w and that the horizontal walls that define the vertical gap has an arbitrary longitudinal profile and electrical conductivity. Employing the conditions of harmonicity of the wake potencial on the transverse coordinates of the source and witness particles, presented in equations (3.12) and (3.13), the author solves partially the wake potential by expanding it in trigonometric functions that automatically satisfy the BC in the vertical plates. This way, similarly to the rotationally symmetric case, the numerical computation is reduced to a bidimensional problem that is solved independently for each term of the expansion. All the advantages presented for ECHOz2 regarding the precision of the results and simulation time also applies for ECHOzR. The main difference between the two codes is that for the recangular code significant post-processing of the results is needed, because the lowest order longitudinal and transverse wake functions are an infinite sum of the modes of the expansion. However, close to center of the chamber, convergence can be achieved by summation of approximately the first ten modes. In Appendix G we discuss on the post processing necessary to retrieve the wakes from the simulation data.

There is also a generic version of the ECHO code, called ECHO3D, that can be used to compute the wakes for an arbitrary geometry. This code has all the advantages of the bidimensional codes, but lacks a key feature: it is not parallelized. For 3D structures this limitation imposes great restrictions on the type of simulation that can be performed, due to the extremelly large computational time.

3.9.3.3 GdfidL Code

When the components of the vacuum chamber do not respect the symmetries required by the 2D solvers or cannot be approximated by one that does, 3D codes must be used. They are also used when a detailed simulation is needed to compute not only the wake potential but also the distribution of the electromagnetic field density in the structure, to calculate heating effects and also the transmission of the fields through ports. The most well-known platforms for this type of simulations are GdfidL (BRUNS, 1997; BRUNS, 2017) and CST Particle Studio (CST, 2017), being the first the code used for Sirius components design and simulation. In Appendix F we discuss on the post-processing of GdfidL computation data.

4 COLLECTIVE EFFECTS

In the previous chapter the mechanism of interation between particles was modeled and formulas for the momentum change of an arbitrary particle due to the action of all the other particles in the beam were derived. In this chapter we will try to include these interactions in the dynamic model of the particles and analyze how the beam will behave as whole.

4.1 Sum of the Wakes

With the theory developed so far it is formally possible to calculate the wake potential for all the structures of the ring and include their effects on the beam dynamics assuming the impulse approximation, which considers the variation of the particle momentum must be applied at the position in the ring equivalent to the center of the impedance source. However, a further approximation is usually done for the calculation of the effect of wake-fields in global parameters of the machine, such as tune–shifts, energy loss and even instabilities. This approximation considers all the impedances sources are located at a single point of ring, in other words, it neglects the phase advances between each wake source. This way the total longitudinal wake of a machine can be given by:

$$W_0'(z) = \sum_i \left(W_0'(z)\right)_i \tag{4.1}$$

where i refers to the i-th impedance source of the ring.

For the transverse plane it is important to remember that the transverse amplitude of the displacements of the source and witness particles varies along the ring, which means the transverse components of the wake potential must be scaled according to the local betatron functions at their positions

$$\begin{aligned} W_u^D &= \frac{1}{(\beta_u)_T} \sum_i \sqrt{(\beta_u)_i^s \, (\beta_u)_i^w} \left(W_u^D(z)\right)_i \\ W_u^Q &= \frac{1}{(\beta_u)_T} \sum_i (\beta_u)_i^w \left(W_u^Q(z)\right)_i \end{aligned} \tag{4.2}$$

where u represents x or y, $(\beta_u)_T$ refers to the value of the betatron function at the position where all the impedances are being lumped, $(\beta_u)_i^w$ is the value of the betatron function at the location where the witness particle feels the kick and $(\beta_u)_i^s$ is the beta function at the location where the source particle generated the wake.

This scaling can be easily understood by the analysis of the wake potential terms of the quadrupolar and dipolar wakes. For example, the horizontal dipole term of the wake potential corresponds to $x_s x_w W_x^D(z)$, which means it depends linearly on the displacement x_s at the point a where it induces the wake fields. If we want to dislocate the position where we want to consider this wake was generated from positions a to b and, on average, keep its value unchanged, it is necessary to consider that the amplitude of movement of the source particle were $\sqrt{\beta_x^a/\beta_x^b}$ larger when it excited the fields and we have to multiply our equivalent wake function by this value. In the same way, the witness particle felt the fields generated by the source at a position c downstream from the point where they were generated and, if we want to consider the position of the witness particle in b, it is important to multiply the effective wake by $\sqrt{\beta_x^c/\beta_x^b}$, to keep the average strength unchanged.

All references in literature consider that the position where the wake is generated and the position where the particles feel these wakes are the same, so in this work we will consider it too. Under such condition, the equations (4.3) reduce to

$$\begin{aligned} W_u^D &= \frac{1}{(\beta_u)_T}\sum_i (\beta_u)_i \left(W_u^D(z)\right)_i \\ W_u^Q &= \frac{1}{(\beta_u)_T}\sum_i (\beta_u)_i \left(W_u^Q(z)\right)_i \end{aligned} \tag{4.3}$$

where $(\beta_u)_i$ is the value of the betatron function at the position of the wake source. However, as seen in Appendix C, depending on the transverse sizes of the chamber the fields can only catch up with the witness at distances of the order of centimeters away from the point where the fields were generated. For 4^{th} GLS, where the focusing is very strong, such a distance is enough for the betatron function to have changed considerably. The effect of this consideration can be a study topic for future studies.

4.2 Energy Loss

One of the most important effects is the energy loss by the beam. It can be computed considering only the leading order term in the momentum change expansion

$$\Delta E \approx c\Delta p \approx c\left(\frac{p_s}{p}\Delta p_s + x'\Delta p_x + y'\Delta p_y\right) \approx c\Delta p_s. \tag{4.4}$$

This way the energy variation of a given particle due to wake-fields depends on which bunch it is and on its longitudinal deviation from the synchronous particle and is given, in the most general form, by the equation (3.31a) multiplied by the average charge of the bunches and the charge of the particle. If we consider the distributions are stationary and the ring is uniformly filled with charge, then the expression for the wake-potential is reduced to equation (3.38).

Under this approximation, the energy variation of a particle after passing througth the impedance source would be given by:

$$\Delta E\,(z) = -eI_bT_0V_0(z) = -eI_bT_0\frac{M\omega_0}{2\pi}\sum_{p=-\infty}^{\infty}\tilde{\lambda}(pM\omega_0)Z_{\parallel}(pM\omega_0)e^{-ipM\omega_0 z/c}. \tag{4.5}$$

where $I_b = Q_b/T_0 = N_be/T_0$ is the current per bunch, T_0 is the revoluton time, N is the number of particles per bunch and e is the absolute value of the elemetary charge of the electron. The average total energy lost by one bunch is given by

$$\left\langle \Delta E\right\rangle_b = N_b\int_{-\infty}^{\infty}\mathrm{d}z\lambda\,(z)\,\Delta E\,(z) = -\left(I_bT_0\right)^2\overbrace{\frac{M\omega_0}{2\pi}\sum_{p=-\infty}^{\infty}|\tilde{\lambda}(pM\omega_0)|^2\Re\left\{Z_{\parallel}(pM\omega_0)\right\}}^{\kappa_{\parallel}} \tag{4.6}$$

where $\kappa_{\parallel}$ is called the longitudinal loss factor, $|\lambda\,(\tilde{\omega})|^2 = \tilde{\lambda}\,(\omega)\,\tilde{\lambda}^*\,(\omega)$ must be an even function of the frequency, given that λ is real. Notice that only the real part of the impedance contributes to the energy loss, because the imaginary part is an odd function of the frequency. The average energy loss per particle can be defined as

$$\left\langle \Delta E\right\rangle_p = \frac{\left\langle \Delta E\right\rangle_b}{N_b} = -eI_bT_0\kappa_{\parallel}. \tag{4.7}$$

For impedances that varys smoothly with the frequency compared to the interval $M\omega_0$, the sum in the definition of the loss factor can be replaced by an integral

$$\kappa_{\parallel} = \frac{1}{2\pi}\int_{-\infty}^{\infty}\mathrm{d}\omega|\tilde{\lambda}(\omega)|^2\Re\left\{Z_{\parallel}(pM\omega_0)\right\} = \frac{1}{\pi}\int_{0}^{\infty}\mathrm{d}\omega|\tilde{\lambda}(\omega)|^2\Re\left\{Z_{\parallel}(pM\omega_0)\right\}. \tag{4.8}$$

The sum of the energy loss in each impedance source of the ring results in and additional energy loss per turn for the particles. This means the new fixed point of the longitudinal one turn map is not given by equation (2.34), but by

$$V(z_0) = U_0 + \left\langle \Delta E\right\rangle_p \tag{4.9}$$

instead, where z_0 is the new synchronous position, measured in relation to the zero current one.

Another important parameter to consider in the design of several components of the vacuum chamber is the power deposited in the wall per unit of area by the beam due to wake fields. To calculate such quantity we need the power loss of the whole beam, which is obtained from equation (4.6) by multiplying it by the number of bunches and dividing by the revolution time of the ring,

$$P_w = \frac{\left\langle \Delta E\right\rangle_T}{T_0} = \frac{M}{T_0}\left\langle \Delta E\right\rangle_b = T_0\frac{I_0^2}{M}\kappa_{\parallel} \tag{4.10}$$

where $I_0 = MI_b$ is the total current stored. Now, to compute the power density one needs to know the distribution of the tangential component of the electric field on the walls of the geometry. For complex geometries simulated in numerical solvers, this is done automatically by the codes, through the computation of the tangential magnetic field and application of the Leontovich boundary conditions (LANDAU; LIFSHITZ, 1960, pp. 280) to get the tangential electric field. When the calculation is performed analytically, not only the impedance, but also the fields in all regions of space must be known. For the round chamber, the symmetry helps and the power per unit of area, D_s, can be get simply by

$$(D_s)_{\text{circle}} = \frac{P_w}{2\pi b L} \tag{4.11}$$

where L and b are the length and radius of the chamber. For flat chambers, which can be approximated by two infinitely large parallel plates, this problem was solved by Piwinski (1992), whose results were used by Nagaoka (2006) to derive a formula that relates the power density of the parallel plates, at a distance b from the particle, with the one from the round chamber,

$$D_s(x) = \frac{\pi^2}{4\cosh^2\left(\frac{\pi x}{2b}\right)} (D_s)_{\text{circle}}\,, \tag{4.12}$$

where x is the transverse position on the plate from the point of minimum distance between the particle and the plate. This function has a maximum value of 2.5 at $x = 0$ and decays to negligible values above $x \approx 4b$.

4.3 Current dependent Hamiltonian

The usual approach to calculate the effects of the wakes on the beam is by introducing the total wake potential of the machine on the one turn averaged Hamiltonian of the ring (BERG, 1996; LINDBERG, 2016). This is justified by the fact that the wake forces are weak and its effects on the beam are very slow, in such a way that the evolution of its parameters are counted in a turn by turn basis. In section 4.1 it was defined a method to sum all the wakes on the machine and the average transverse Hamiltonian was defined in section 2.2.6, especifically in equation (2.29), and the average longitudinal Hamiltonian was defined in subsection 2.3.4, by equation (2.40).

Besides, the coupling between both transverse planes is very small in normal conditions of operation of the machine. On the other side, the wakes strongly couples the evolution of the transverse dynamics with the longitudinal plane. For this reason, the transverse analysis of transverse collective effects usually deal with the Hamiltonians of one transverse and the longitudinal planes togheter. The analysis of the longitudinal motion is again simplified, without the need of considering the transverse degrees of freedom of the particles. With these considerations, the total one turn Hamiltonian of the particles is

$$H_n = J_u \left(\nu_u + \xi_u \delta + J_u \frac{A_{xx}}{2}\right) + H_\parallel - \frac{\langle I \rangle T_0 V_n(u,z,s)}{(E_0/e) L_0} \tag{4.13}$$

where $\langle I \rangle T_0$ is the average charge per bunch, the subscript n in the Hamiltonian indicates that it is related to the n–th bunch of the machine and the effective wake potential is given according to the ideas developed in section 3.7, specifically by equations (3.31),

$$\begin{aligned} V_n(u,z,s) = \sum_{l \in \mathscr{B}} \frac{I_l}{\langle I \rangle} \sum_{k=-\infty}^{\infty} \int \mathrm{d}z' \Big(& \lambda_l(z'; s - s_r) W_0(z - z' + s_r) + \\ & u d_l(z'; s - s_r) W_u^D(z - z' + s_r) + \\ & \frac{u^2}{2} \lambda_l(z'; s - s_r) W^Q(z - z' + s_r) \Big), \end{aligned} \tag{4.14}$$

where s_r is the retarded position defined in equation (3.30), λ_l and d_l are the longitudinal distribution and dipole moment of the beam, defined in equations (3.32), and W_0 is the primitive function of the longitudinal wake, W_0'.

4.4 Potential-Well Distortion

All the effects of the wakes on the beam can be calculated from the Hamiltonian defined in equation (4.13). One particular effect is the distortion of the potential well created by the RF cavities, which changes the equilibrium distribution of the particles and the intrabunch dynamic properties such as the synchrotron tune.

To calculculate susch effect we consider a static distribution for the beam and neglect the effects of W_u^D and W^Q, because they are small for a well centered beam in the vacuum chamber. Besides, apart from the effect of cavities, which will be discussed in Appendix **??**, the distortions are dominated by short range wakes, in such a way that we can neglect the multi–bunch and multi–turn contributions. Under such considerations, the Hamiltonian of the particle becomes

$$H = \frac{\alpha}{2}\delta^2 + U(z) - \frac{I_b T_0}{(E_0/e) L_0} \int \mathrm{d}z' \lambda(z') W_0(z - z'), \tag{4.15}$$

which is time–independent. Following the same reasonings performed in section 2.4.1 we notice that equation 2.47 is still valid if we substitute the expression for the longitudinal distribution by

$$\lambda(z) = \frac{1}{A} \exp\left(\frac{1}{\alpha \sigma_\delta^2}\left(-U(z) + \frac{I_b T_0}{(E_0/e) L_0} \int \mathrm{d}z' \lambda(z') W_0(z - z')\right)\right), \tag{4.16}$$

which is a transcendental integral equation for the longitudinal distribution. This equation was first proposed and solved by Haïssinski (1973) and for this reason carries his name. Even though analytical solutions exist for some special impedances, such as the one presented by Shobuda & Hirata (1999), in general it must be solved numerically. In Appendix I.2.1 we will describe the approach used in this work for such a solution

4.5 Incoherent Tune–shifts

Another effect derivable of the Hamiltonian of equation (4.13) is the variation of the transverse oscillation frequency of the bunch as a function of the current,

$$\Delta\nu_u^n = \frac{(\Delta\mu_u')^n}{\omega_0/c} = \frac{1}{\omega_0/c}\left(\left.\frac{\partial H_n}{\partial J_u}\right|_{\langle I\rangle} - \left.\frac{\partial H_n}{\partial J_u}\right|_{\langle I\rangle=0}\right) \tag{4.17}$$

where the superscript n was used because the tune–shift is different for different bunches if the filling pattern is not uniform and the wakes that generates it are multi–turn effects. Considering the distributions are in equilibrium, we can show that

$$\Delta\nu_u^n = \frac{\langle I\rangle\, T_0}{2\pi(E_0/e)}\sum_{l\in\mathscr{B}}\frac{I_l}{\langle I\rangle}\sum_{k=-\infty}^{\infty}\int \mathrm{d}z'\left(\sqrt{\frac{\beta_u}{2J_u}}\cos(\mu_u)d_l(z')W_u^D(z-z'+s_r)+\right. \tag{4.18}$$

$$\left.\beta_u\cos^2(\mu_u)\lambda_l(z')W_u^Q(z-z'+s_r)\right), \tag{4.19}$$

where it was used $u = \sqrt{2J_u\beta_u}\cos(\mu_u)$. Notice that for a well centered beam $d_l = 0$ and the dipole wake does not influence the tune, and even in the case when the beam is off centered its average effect is zero, because of the term $\cos(\mu_u)$ that averages to zero for each particle in the beam, unless the tune is very close to an integer value. The quadrupolar wake, on the other hand, creates a z dependent tune–shift in the beam

$$\Delta\nu_u^n = \beta_u(1+\cos(2\mu_u))\frac{\langle I\rangle\, T_0}{4\pi(E_0/e)}\sum_{l\in\mathscr{B}}\frac{I_l}{\langle I\rangle}\sum_{k=-\infty}^{\infty}\int \mathrm{d}z'\lambda_l(z')W_u^Q(z-z'+s_r) \tag{4.20}$$

Considering an uniform filling patern, with M equal bunches equally spaced, we can follow the reasonings presented in subsection 3.7.2 and use equation (3.39b) to show that

$$\Delta\nu_u = -\beta_u(1+\cos(2\mu_u))\frac{I_bT_0}{4\pi(E_0/e)}\frac{iM\omega_0}{2\pi}\sum_{p=-\infty}^{\infty}\tilde{\lambda}(pM\omega_0)Z_u^Q(pM\omega_0)e^{-ipM\omega_0 z/c}, \tag{4.21}$$

where I_b is the current per bunch. Averaging this result with the bunch distribution and using the impedance property described in equation (3.23b), we get

$$\langle\Delta\nu_u\rangle = \beta_u\frac{I_bT_0}{4\pi(E_0/e)}\overbrace{\frac{M\omega_0}{2\pi}\sum_{p=-\infty}^{\infty}|\tilde{\lambda}(pM\omega_0)|^2\Im\left\{Z_u^Q(pM\omega_0)\right\}}^{\kappa_u^Q}, \tag{4.22}$$

where κ_u^Q is the quadrupolar kick factor. Notice that

4.6 Instabilities

4.6.1 Multi-Turn Instabilities

4.6.2 Single-Turn Instabilities

4.7 Analytical Treatment

4.7.1 The Linearized Fokker-Planck Equation

4.7.1.1 Modal expantion

4.7.1.1.1 Head-tail modes

4.7.1.2 Solution for Gaussian Bunches

4.7.1.3 Low Current Limit: Multi-Turn Instabilities

4.7.1.4 High Current Limit: Mode Coupling Instabilities

4.7.2 The Microwave Instability

4.7.3 Strong Head-tail instability

5 IMPEDANCE MODELING

In this chapter the modelling of the impedance of some components of the storage ring will be described. The components described below are the ones for which the modeling is not trivial and required detailed analysis of some key aspects. The gathering of all the components and analysis of the whole impedance budget will be performed in the next chapter.

5.1 Standard Chamber

Sirius standard vacuum chamber will be round, made of copper and will have an internal radius, b, of 12 mm, which is considerably smaller than the chambers of the 3rd GLS, as showed by Nagaoka & Bane (2014). This small chamber does not only affect the resistive wall impedance, which scales with $1/b^3$ for the transverse planes, but also all the other components impedance, because of the proximity of the walls with the beam (NAGAOKA; BANE, 2014). Besides, the solution adopted for the vacuum in Sirius employs the mixed and concomintant use of localized and distributed pumping, where the last is achieved through coating the vacuum vessel with NEG (BENVENUTI *et al.*, 1998; PRODROMIDES, 2002). In 2012 the LNLS signed a license agreement with CERN to use NEG and since then the Vacuum Group has been working on the development of the infrastructure and improvement of techniques for production, deposition and in–situ activation of NEG, to produce coatings with low surface roughness and good thickness uniformity in all vacuum chambers of the ring, as explained by Seraphim *et al.* (2015) and Rocha (2017).

The presence of NEG changes the electromagnetic properties of the inner surface of the chamber and contributes to the increase of the impedance. This effect was first noticed in an impedance measurement made in ELETTRA by Karantzoulis *et al.* (2003), where the authors described an anomalous increase of the tune–shift with current after the installation of NEG coated Aluminum chambers for IDs. Nagaoka (2004b) tried to explain the measured results using the multi–layer formulas for the transverse impedance, but quantitative agreement was only obtained using excessively large resistivities for NEG. Such experimental results created some concern in the community and the effect of the roughness of the inner surface of the chamber was hipotesized as a possible explanation. Nagaoka *et al.* (2007) studied such an effect when analyzing Soleil storage ring measurements, where the impedance budget of the machine was not enough to account for the bunch lengthening observed, and concluded that the impedance of the measured roughness could not explain the additional impedance necessary to fit the experimental results.

There are expressions in the literature to estimate the impedance of a rough surface, such as ones of Bane *et al.* (1997), based on numeric calculations, and of Stupakov *et al.* (1999), calculated analytically. Their prediction accounts for an inductive impedance in low frequency, where the characteristic length of the surface protrusions is much smaller than the bunch length, and real impedance for very large frequencies. However, one of the considerations for the derivation of such formulas is that the surface is perfectly conducting, which means all the image charges will flow by the rough surface. It seems reasonable that for finite conductivity chambers, the wall currents will penetrate the material and the effect of the roughness should be even smaller.

Given all the considerations presented above, the initial model adopted for the standard Sirius vacuum chamber is a round smooth multi–layer and infinite pipe, where three layers are considered: 1 µm of NEG coating, 1 mm of copper and air to infinity. Table 2 shows the values of the main parameters of this model, where one can notice that the value used for NEG conductivity was $1\,\mathrm{MS\,m^{-1}}$. This value is the average result of a measurement of the NEG resistivity as function of the frequency made by Koukovini-Platia *et al.* (2014). Since this measurement was performed for a very short frequency range, only from 10 to 11 GHz, and considering that other factors may influence the NEG conductivity, such as the activation process and aging effects, we calculated the impedance for several values of conductivity, as shown in Figure 11a. Also shown in the figure is the spectrum, in arbitrary units, of a gaussian bunch with $\sigma = 2.5$mm, which is the natural bunch length of the Sirius storage ring. Notice that the dependency of the impedance for the frequency range of interest is very non-linear, being almost saturated for lower conductivities, which means that variations on the conductivity does not have a strong impact on the beam behavior. We can also infer from the figure that the effect of NEG on the impedance is mostly inductive in both planes, where an increase of a factor of 3 in the imaginary impedance is noted.

The increase of the imaginary impedance is clearly evidenciated by Figure 12a,

Table 2 – Wall Impedance parameters.

Parameter	Value	Unit
Copper conductivity	59.0	$\mathrm{MS\,m^{-1}}$
Copper relaxation time	27	fs
NEG conductivity	1.0	$\mathrm{MS\,m^{-1}}$
NEG thickness	1.0	µm
Chamber radius	12.0	mm
Chamber thickness	1.0	mm
Total Length	500	m
Dipole Length	100	m
Chamber shape	round	

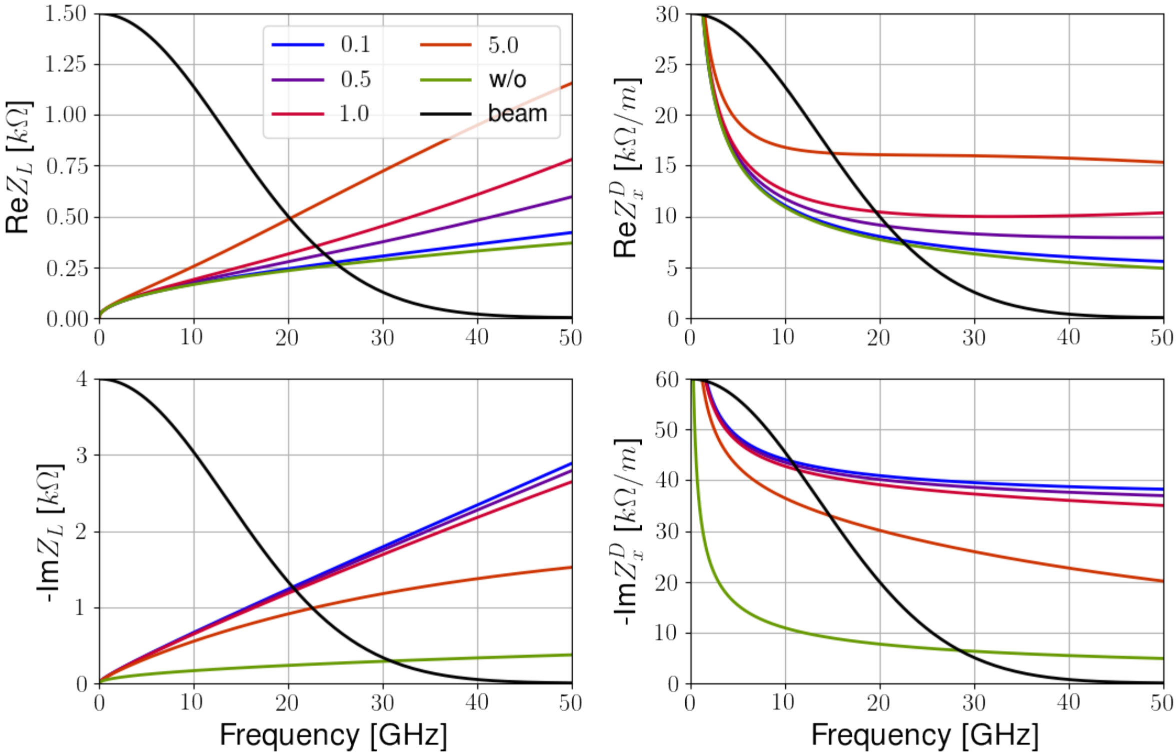

(a) Wall Impedance as function of NEG conductivity (in $\mathrm{MS\,m^{-1}}$).

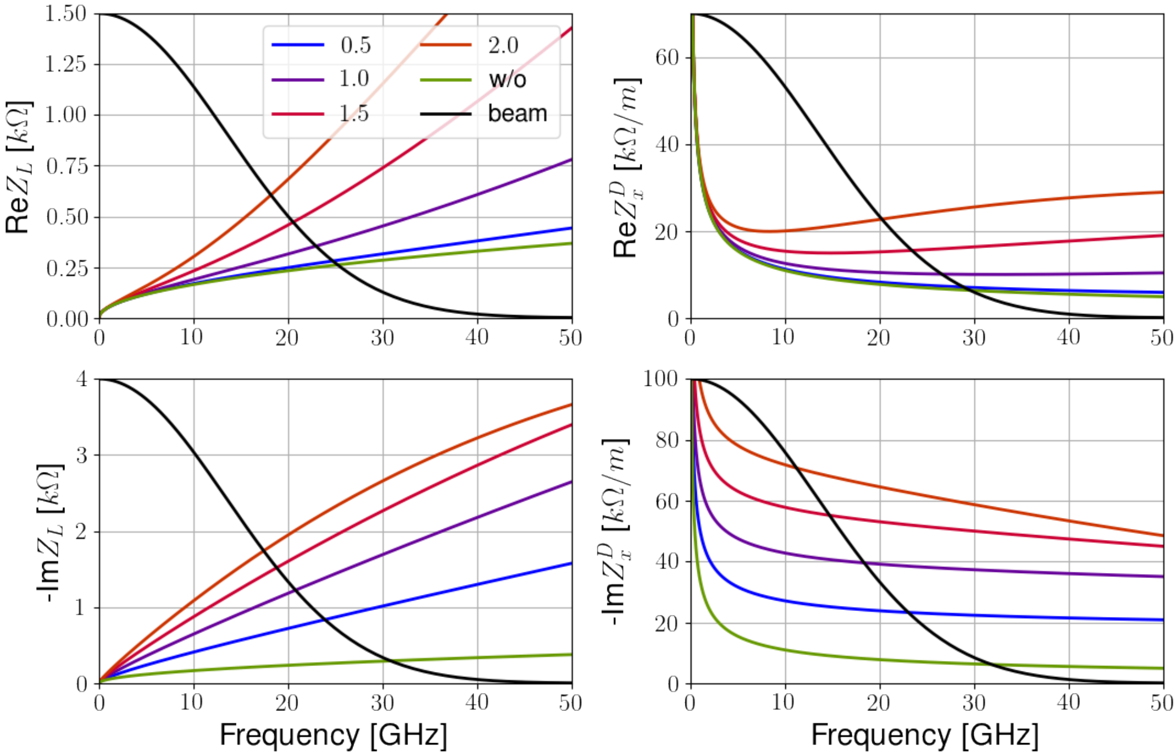

(b) Wall Impedance as function of NEG thickness (in µm).

Figure 11 – Wall impedances as function of the frequency for several values of NEG conductivity (a) and coating thickness (b). The nominal values for both are presented in Table 2. Also shown in black is the spectrum of a 2.5 mm gaussian bunch.

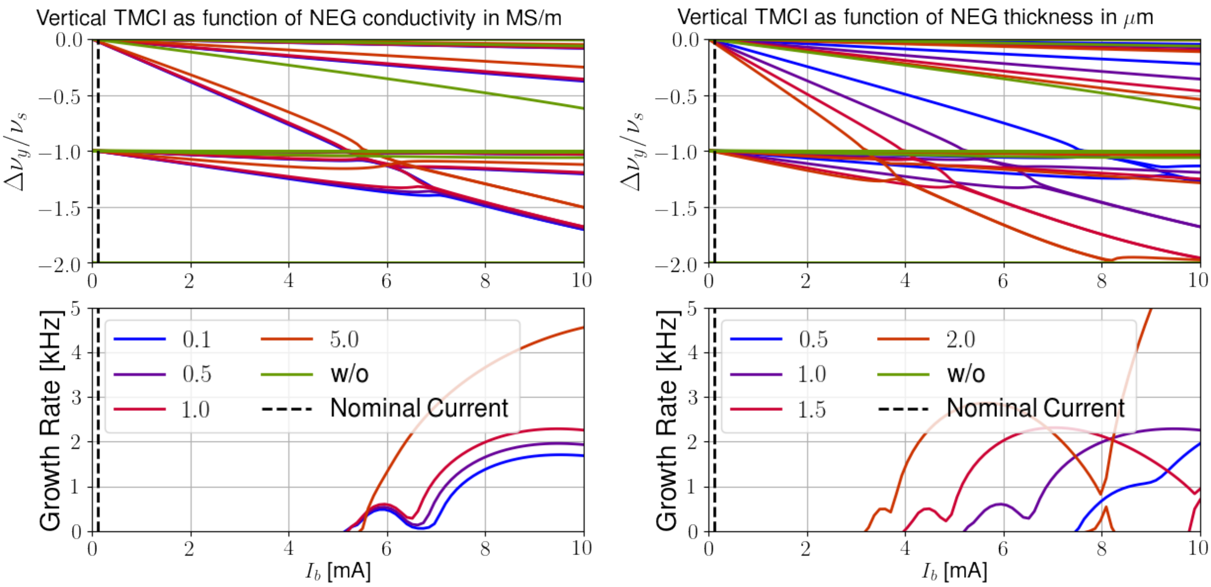

(a) NEG conductivity in $\mathrm{MS\,m^{-1}}$ (b) Coating thickness in µm.

Figure 12 – Simulations of Transverse Mode-Coupling Instability (TMCI) instability for one single bunch in the machine using the parameters of the first phase of operation of the storage ring, as shown in Table 1, and for several different values of NEG conductivity (a) and coating thickness (b).

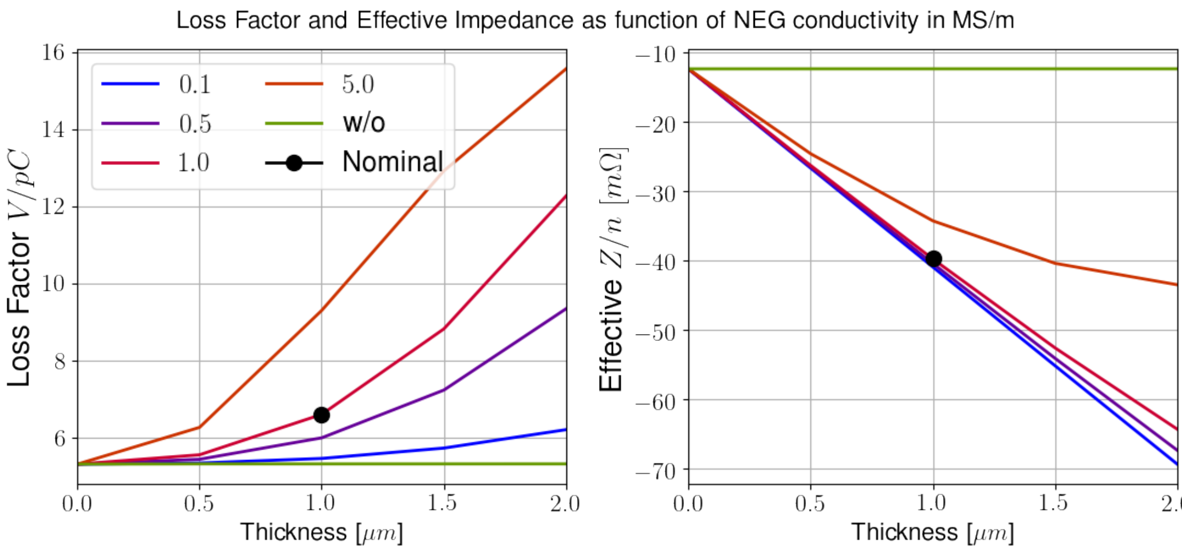

Figure 13 – Loss factor (left) and effective longitudinal impedance (right) for a 2.5 mm bunch as function of the coating thickness for several different values of NEG conductivity, in $\mathrm{MS\,m^{-1}}$.

which shows simulations of transverse single bunch tune-shift and the TMCI instability, and Figure 13, which shows the loss factors and the effective longitudinal impedance.

It was also carried out an study of the dependence of the impedance on the thickness of the NEG coating, as shown in Figure 11b, Figure 12b and Figure 13. Notice that, differently of the conductivity, this parameter has strong influence on the value of the impedance, affecting almost linearly the imaginary part in both planes and quadractically the loss factor.

From the analysis of Figure 12 we note that, even though the NEG coating has a strong influence on the impedance, the TMCI threshold induced only by its contribution is much above the nominal single bunch current for uniform filling of the machine and do not compromise the operation. Besides, as will be seen with further details in the next sections, the increased longitudinal inductive impedance will contribute to the bunch lengthening, which helps decreasing intrabeam scattering effects and improve touscheck lifetime.

A complete analysis of the impedance of a NEG coated chamber is provided by Shobuda & Chin (2017), who explains the existence of several regimes along the spectrum where different mechanisms majorly defines the impedance behavior. For example, the skin depth of NEG at 30 GHz is approximately 3 µm, which is three times larger than the thickness of the coating used in Sirius chambers, thus, in the frequency range analysed so far, from 1 to 50 GHz, most of the losses happens on the copper chamber and that is why the impedance is mostly inductive. For higher frequencies the NEG contribution will be resistive, and for lower it will not have any effect on the impedance.

One particular range of interest for Sirius is the very low frequency part of the impedance, which goes from 0 Hz to a few MHz, because in this range two important mechanisms which influence the dynamics of the beam are defined. The first is the traditional resistive–wall instability, defined by the harmonic of the betatron frequency with lowest frequency, being numerically equal to the fractional part of the tune times the revolution frequency. The second is the incoherent tune–shift induced by the quadrupolar impedance, which depends on the zero frequency value of the impedance. This mechanism was introduced in section 4.5 and is quantitatively described by equation (4.22). Considering that the resistive–wall impedance has a very sharp peak at zero frequency, this term has strong influence on the whole sum that defines the tune–shifts, mainly for multi-bunch operations. Actually the infinitely thick wall theory, from Gluckstern *et al.* (1993) and Yokoya (1993), provides divergent results for this tune–shift. Nagaoka (2001) solved this problem to explain measurements in ESRF using a method developed by Heifets (1998) and detailed explained by Chao *et al.* (2002), which employed the concept of the diffusion time of the magnetic field in the chamber to truncate the multi–turn effect of this impedance as a way of considering the finite thickness of the wall. Later, Shobuda & Yokoya (2002) showed that such approach is not needed when the impedance already takes into account the finite thickness.

The impedance at very low frequencies is very difficult to calculate because it depends on what is outside the vacuum chamber, due to the increasingly large skin depth. Shobuda & Yokoya (2002) pointed this possibility out when they tried to ex-

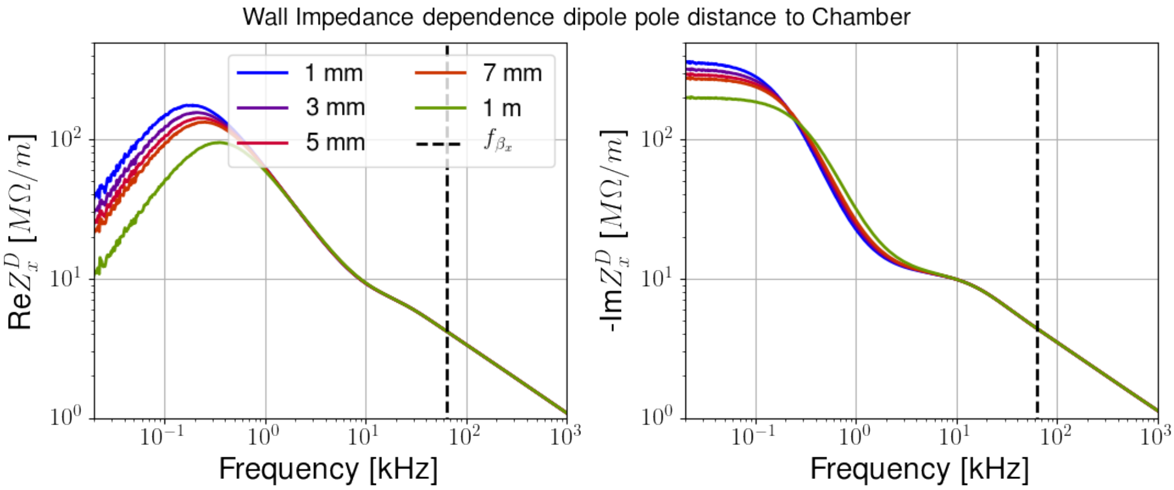

Figure 14 – Low frequency impedance for different values of distance of the magnetic poles of dipoles to the exterior part of the vacuum chamber.

plain the tune–shifts observed in KEKB with their finite–thick wall theory. With the multi–layer formulas used in this work it is possible to see the influence of materials outside the chamber on the impedance, as shown Figure 14, where the infinitely thick layer of air was substituted by a variable gap of air and a layer of NdFeB ($\mu_r = 40$), used in the magnetic poles of Sirius magnets. Note that the first betatron line, responsible for the coherent tune–shifts and the resistive–wall instability is completely determined by the copper chamber, but the zero frequency impedance depends on the distance of the magnet to the external part of the wall. One can argue that, since Sirius vacuum chamber is round, this dependence is not important because there is no quadrupolar impedance. However, considering that the impedance at these frequencies depend on the materials outside the chamber, it is reasonable to think it will depend on how they are distributed too. Remembering that the storage ring is filled with magnets with cores made out of ferromagnets, and noticing that only dipoles can generate a quadrupolar impedance, because the symmetry of the poles of quadrupoles and sextupoles does not allow such component, we considered this effect on the total budget.

According to Zotter & Kheifets (1998, p. 340) the indirect space charge impedance in the ultra-relativistic limit at zero frequency (for penetrating fields) is given by

$$Z_y = i\frac{Z_0 L}{\pi}\left((\varepsilon_1 - \xi_1)\frac{1}{h_1^2} + (\varepsilon_2 - \xi_2)\frac{1}{h_2^2}\right) \tag{5.1}$$

where the indices h_1 and h_2 refer to the electric and magnetic gaps, respectively, ε_i and ξ_i are the Laslett (1963) coefficients for incoherent and coherent tune–shifts associated with the electric (1) and magnetic (2) fields, given by

$$\begin{aligned} &\varepsilon_1 = \varepsilon_2 = 0, \quad \xi_1 = \xi_2 = \frac{1}{2} \quad \text{for round chambers,} \\ &\varepsilon_1 = \frac{\varepsilon_2}{2} = \frac{\pi^2}{48}, \quad \xi_1 = \xi_2 = \frac{\pi^2}{16} \quad \text{for flat chambers.} \end{aligned} \tag{5.2}$$

The coherent coefficients, ξ_i, are a particular case of the dipole impedance, while the incoherent coefficients, ε_i, of the quadrupole impedance. This way, we can intepret the low frequency limit of the impedances show in Figure 14 as the sum of the electric and magnetic incoherent space–charge impedance. In fact, a direct evaluation of equation (5.1) for the electric boundary using h_1 equals to the internal radius of the vacuum chamber gives an impedance of 208 MΩ, which is very similar to the value of 200 MΩ taken from the curve where the magnet is far from the beam. The magnetic part gives a contribution of 117 MΩ when we consider the dipole is 16 mm away from the center of the chamber, which corresponds to the curve 3 mm of the graph. This value is also close to the 120 MΩ, obtained by the subtraction of the curve 3 mm by the curve 1 m. With all the considerations above, we defined the quadrupolar impedance for the Sirius vacuum chambers as [1]

$$Z_y^Q(\omega) = -Z_x^Q(\omega) = \left(\left(Z_y^D(\omega)\right)_{\text{round}}^{3\text{ mm}} - \left(Z_y^D(\omega)\right)_{\text{round}}^{1\text{ m}}\right) \frac{\varepsilon_2^{\text{flat}}}{\xi_2^{\text{round}}} \frac{L_D}{L_T} \tag{5.3}$$

where L_T is the total length considered for the chamber, L_D is the length covered by dipoles and the fraction involing the LASLETT coefficients is the conversion from the round dipole factor to the flat quadrupole factor. Note that if we had used the YOKOYA factors in the equation above we would get an impedance two times lower. This approach is not correct because this factors were derived under the assumption of infinitely thick chambers, which means they are only valid in the frequency range where the electric and magnetic fields are shielded at the same place, in other words, when they do not penetrate the material.

5.2 Kicker Chambers

The Sirius storage ring will have two kicker magnets, one standard dipole kicker and one non-linear kicker. While the first will be used for on-axis injection in the commissioning of the light source and as a pinger magnet for machine studies, the second will be used for injection in top-up mode (LIU *et al.*, 2016b). Even though the topology of both magnets is very different, their vacuum chamber will be identical: a ceramic chamber, coated with 10 μm of Titanium. This means that at high frequencies their impedance will be identical too. Below we describe the considerations on the modeling of the impedance of the dipole kicker magnet and then extrapolate to the case of the non-linear kicker. Table 3 shows the main values of the parameters used to model these components.

Figure 15 shows an schematic drawing of a transverse section of the window-frame

[1] As the Sirius dipoles are straight magnets with inclined poles to produce a quadrupole gradient and the chambers, as well as the beam trajectory, are curved along them, the distance of the poles to the chamber is variable. Nevertheless, 3 mm is a good estimate for the average distance and that is why it was used in the definition above.

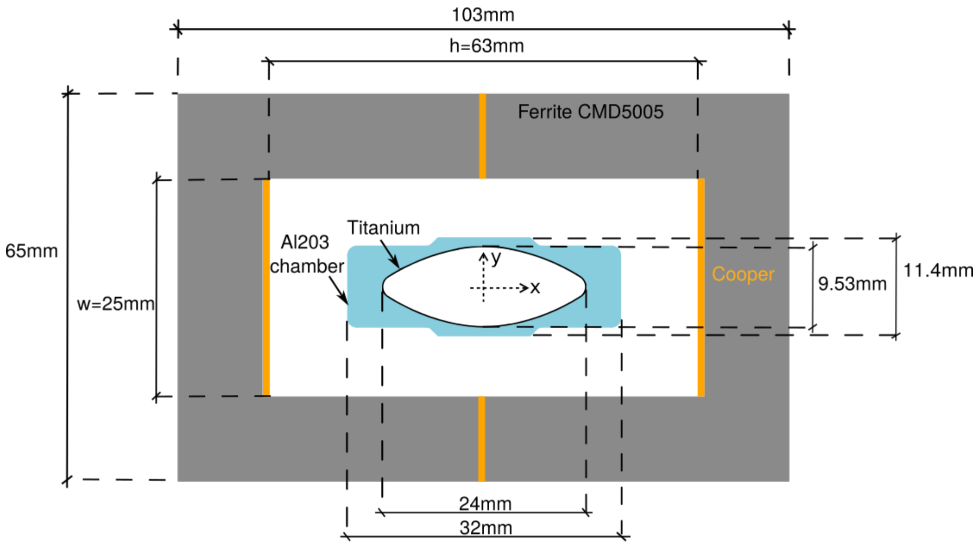

Figure 15 – Cross section of the kicker window–frame magnet that will be used in Sirius storage ring.

dipole kicker magnet that will be used in Sirius storage ring. This type of magnet acts on the beam by the passage of a very strong pulsed current, generated by an external pulser circuit, on the lateral copper plates. This current induces a magnetic field around the plates that is guided by the ferrite to create an almost constant vertical field at the inner gap of the magnet. The copper plates located at the center of the magnet are important to increase the magnetic impedance for the field lines, forcing them to close the loop by the air gap and not around the ferrite blocks.

There are two main contributions to the impedance of this type of magnet: the losses and resonances defined by the materials of the vacuum chamber and the window-frame itself and the coupled flux of the beam with the external circuit that feeds the magnet. While the first contribution dominates the high frequency part of the spectrum, the second is important at low frequencies.

Table 3 – Main parameters of the Kicker magnet for impedance modeling

Parameter	Symbol	Value	Unit
Capacitance	C_{bb}	30.0	pF
Parasitic Resistance	R_s	500	Ω
Pulser circuit resistance	R_e	50.0	Ω
Ferrite permittivity		12	
Ferrite initial permeability	μ_i	1600	
Ferrite saturation frequency	ω_s	20.0	$\mathrm{Mrad\,s^{-1}}$
Ceramic permittivity		9.3	
Titanium conductivity		1.6	$\mathrm{MS\,m^{-1}}$
FeSi conductivity		2.0	$\mathrm{MS\,m^{-1}}$
FeSi permeability		40	

The coupled flux, first modeled by Nassibian & Sacherer (1979) and improved by Davino & Hahn (2003), treats the window-frame as a transformer that couples the beam with the external circuit impedance, $Z_g(\omega)$, characterized by the impedance termination of the pulser circuit and the residual capacitances and resistances of the device, which can be accessed via twin wire measurements (MOSTACCI; CASPERS, 2016) of the opened and shorted circuits on the endplates, as explained by Davino & Hahn (2003). This model predicts impedances for the coupled flux given by

$$Z_\parallel^* = \frac{\Delta^2}{h^2}\frac{i\omega L_2 Z_g}{i\omega L_2 + Z_g}, \quad Z_X^D = \frac{c}{\omega\Delta^2}Z_\parallel \tag{5.4}$$

where Δ is a transverse offset of the beam,

$$L_2 = \mu_0 L \frac{h}{w}\frac{\mu_r t}{\mu_r t + h\left(\frac{h}{w}+1\right)}, \tag{5.5}$$

L is the length of the magnet, h and w are the transverse dimensions defined in Figure 15, t is the ferrite thickness and $\mu_r = \mu_r(\omega)$ is the frequency dependent relative magnetic permeability of the ferrite, which can be modeled by

$$\mu_r(\omega) = 1 + \frac{\mu_i}{1 + i\frac{\omega}{\omega_s}} \tag{5.6}$$

where μ_i is the initial permeability and ω_s is the saturation frequency of the material. In the case of Sirius, the ferrite that will be used in this magnet is the CMD5005 (Ceramic Magnets, 2017) and the μ_i and ω_s of the equation above were obtained by fitting the datasheet curve. The values found agreed well with direct measurements made by Hahn & Davino (2002).

Note in equation 5.4 that the coupled flux does not contributes to the vertical impedance and that for a well centered beam, $\Delta = 0$ the longitudinal impedance is zero too. Considering there is no measurements yet for the circuit impedance, $Z_g(\omega)$, of the kicker magnet, the parametric dependency described by Davino & Hahn (2003)

$$Z_g(\omega) = R_e + \frac{1}{\frac{1}{R_s} + i\omega C_{bb}} \tag{5.7}$$

was used for Sirius, where C_{bb} is the busbar capacitance, equal to 30 pF for their kicker, R_s is a resistance in parallel with the capacitance to account for the ferrite losses, equals to 490 Ω in their case, and R_e is the matching impedance of the external circuit, which we considered equal to 50 Ω. Figure 16 shows the coupled flux horizontal impedance for some values of C_{bb} and R_s, where it is possible to notice the resonant behaviour created by the parallel association of the inductance L_2 with the capacitance C_{bb}. Note how these values influence the positioning, intensity and width of the resonant peaks, all around a few MHz, but do not change the value of the imaginary impedance at lower frequencies. As will be shown below, the Titanium coating in the vacuum chamber shields the electromagnetic fields of the beam starting from approximately the frequency range of these peaks, thus, it is expected they will be attenuated. However, the low frequency impedance will not, and will influence the coupled-bunch motion. This source of impedance will not contribute to the incoherent tune–shifts because there is no quadrupolar impedance associated with this mechanism.

Regarding the uncoupled flux, there are no formulas in the literature to estimate the impedance of an out-of-vacuum window-frame magnet as the one presented in Figure 15. There is, however, a model for an in-vacuum magnet developed by Tsutsui (2000) for the longitudinal impedance, which was extended to the transverse dipole impedances by Tsutsui & Vos (2000) and then to the quadrupolar impedance by Salvant *et al.* (2010). These formulas were derived by solving the ME exactly for an ultra-relativistic beam, considering the geometry of Figure 17, which is infinite in the longitudinal direction. Note that in this model the fraction of the fields generated by the beam that are inside the region defined by the angle θ directly interacts with a PEC material, which is an approximation to the cooper plates of the real magnet, and the rest of the field directly see the ferrite, which is a lossy material. With the exception of the presence of the vacuum chamber, this is what happens in the real magnet, which makes this model a good approximation for its geometry.

In order to estimate the effect of the vacuum chamber on the impedance, other models based on the round multi-layer formulas were analysed. The idea behind the formulation of these models is to try to account for limiting cases of the Tsutsui geometry

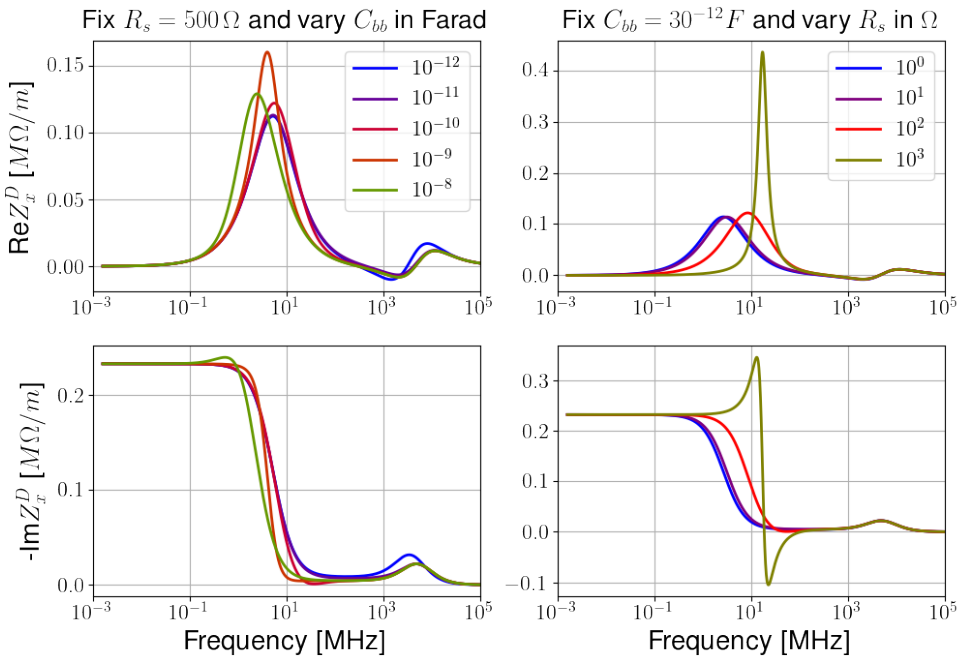

Figure 16 – Coupled flux impedance of the dipole kicker magnet as function of the frequency for several values of capacitance (left) and resistance (right).

in relation to the angle θ, that defines the proportion of the fields that interact with a good conductor. Under these assumptions the models are:

Worst case (W): The beam only sees the ferrite. The layers of the round model in this case are composed by: Titanium, ceramic, air, ferrite and Copper;

Best case (B): The beam only sees the good conductor: Titanium, ceramic, air and Copper;

No Coating (NC): To show the effect of the Titanium coating, this layer was removed from the analysis of the worst case model: ceramic, ferrite, air and Copper.

Figure 18 shows the transverse impedances of the four models analysed. Note that the W curve matches the low frequency limit of the NC case, but at approximately 1 MHz the coating starts to affect the impedance, damping all of them to very low values. Besides, notice that the impedance predicted by the Tsutsui model (TT) is even lower than the

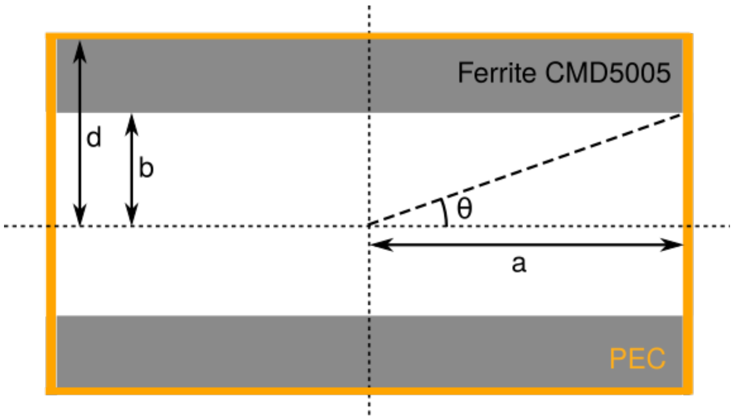

Figure 17 – Tsutsui model for the window–frame kicker magnet.

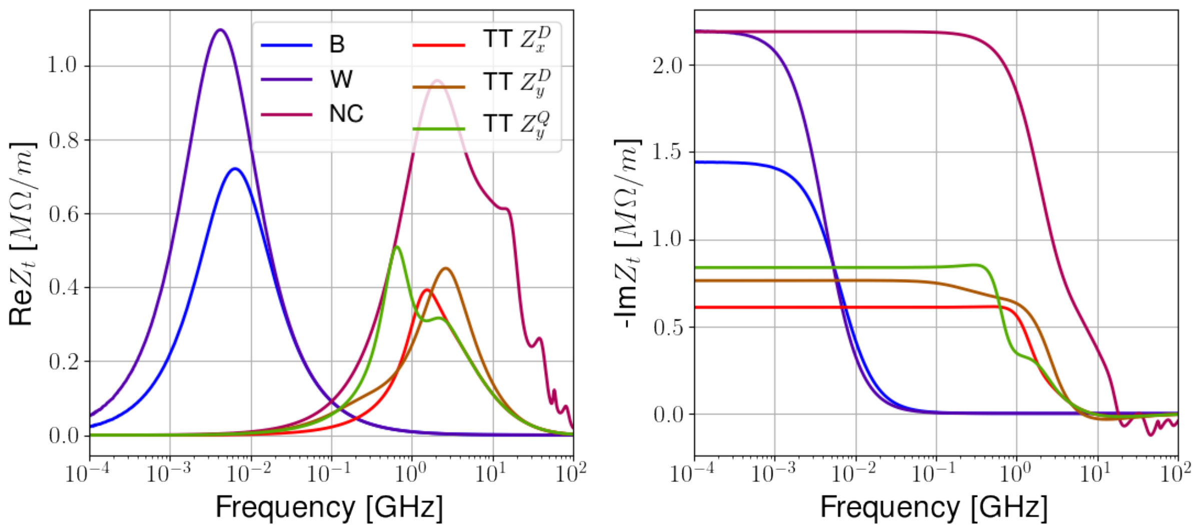

Figure 18 – Transverse impedances of the four models of kicker analysed.

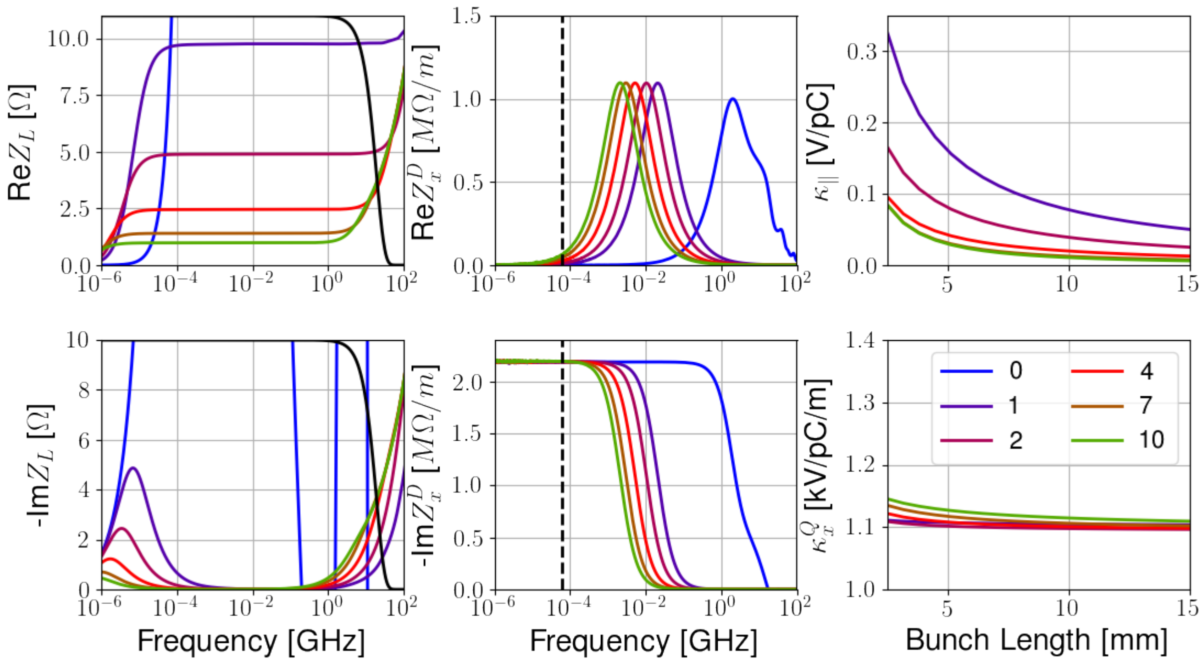

Figure 19 – Longitudinal (left) and dipole horizontal (middle) impedances as function of the frequency for several values of coating thickness, in µm. The spectrum of a 2.5 mm bunch is also shown (solid black) in the left to highlight the important part of the frequency spectrum, and the first horizontal betatron line (black dashed) is shown in the middle. In the right is shown the loss factor (above) and quadrupolar kick factor (below) as function of the bunch length for several values of coating thickness.

B case, and that the relations between the three of them cannot be described by the constant Yokoya (1993) factors, a property already pointed out by Salvant *et al.* (2010). Considering that this component have a stronger influence on the total budget due to the low frequency limit of the impedance, the model adopted for the transverse plane was the W case, multiplied by constant factors that matches its impedance to the tsutsui model. The values used were (0.42, 0.52, 0.58) for the dipole horizontal, dipole vertical and quadrupole vertical impedances, respectively. Note that the factor for the dipole horizontal impedance is very close its counterpart given by Yokoya (1993), $\pi^2/12 \approx 0.41$, which is an indication that this wake function is strongly influenced by the copper plates of the magnet.

For the longitudinal plane it is well–known from the works of Zotter (1969a) and Piwinski (1977) that the coating influences the impedance at much lower frequencies than the skin depth of the metal. For this reason we varied the thickness of the Titanium layer in our simulations to check if it could be thinner than the nominal value. The results are shown in Figure 19, where we note that indeed the coating is effective since very low frequencies, because of the difference from the result without coating. For almost all the relevant frequency range, the longitudinal impedance is constant, starting increasing only at large frequencies, because in this limit it is dominated by skin–depth effect on the

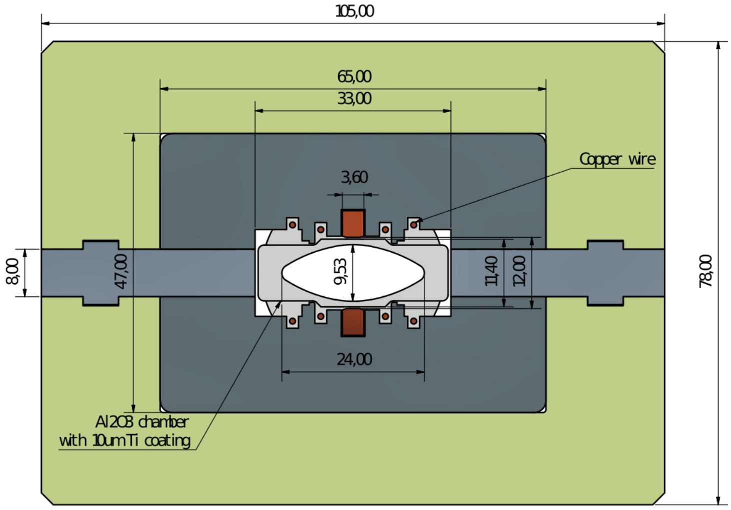

Figure 20 – Drawing of a deprecated version of the non–linear kicker that will be for injection in Sirius storage ring. The current version of the magnet does not have the copper blocks below and above the vacum chamber. The magnet core is made of FeSi.

Titanium and the standard resistive wall characteristics apply. However, note that the baseline of the impedance is almost inversely proportional to the thickness of the coating. This effect is seen in the behavior of the loss factor also shown in Figure 19, which can be used to calculate the power density on the wall through equations (4.10), (4.11), and (4.12). Note that a reduction of the coating thickness to 4 µm would not impact the impedance and heating issues. In the transverse plane, the effect of the coating reduction is only to cause a linear shift on the frequency where the impedance is damped, which does not change its effect on the beam, as can be seen by the quadrupolar kick factor.

Figure 20 shows an old version of the non-linear kicker magnet that will be used in Sirius. Based on the study presented above, we defined the impedance of this kicker as a round multi–layer chamber with: vacuum, Titanium, ceramic, air, FeSi and Copper. Besides the substitution of the ferrite with the FeSi as the magnet core, this component does not have the parallel copper plates to induce a dipole kick on the beam, creating a much more complex transverse field dependence using copper wires displaced transversely. Such property makes the use of the TSUTSUI model unapropriate for this case, and instead of multiplying the resultant impedance of the round chamber by the same factors of the dipole kicker, we decided to use the LASLETT coefficients, defined in equation (5.2). This magnet also does not have the coupled flux part of the impedance, because the external circuit does not couples with a beam close to the center of the magnet.

5.3 Fast Correctors Chambers

The Fast orbit correctors of the Sirius storage ring will operate at an update rate of 100 kHz in the Fast Orbit Feedback System (FOFB) (TAVARES *et al.*, 2013), requiring special vacuum chambers in order for such high frequency fields to penetrate. The solution adopted was to brase small and thin stainless steel chambers in the standard copper chamber of the ring. The reduced conductance, only 1 MS, of this material provides a skin depth of 1.6 mm at 100 kHz, which is much larger than the thickness of the chamber, which is 0.1 mm, and do not damp or distort significantly the external field of the magnet. The relevant parameters used for modeling of this type of chamber is presented in Table 4.

Table 4 – Main parameters for the fast correctors impedance model.

Parameter	Value	Unit
SS conductivity	1.3	$\mathrm{MS\,m^{-1}}$
Chamber thickness	100	µm
Chamber radius	12	mm
Chamber length	100	mm
Number of elements	80	

The small length of these chambers, only 10 cm, raises a question on the validity of the infinitely long formulas of the multi-layer chambers used so far. This question is answered by Shobuda *et al.* (2009), who calculated the impedance of a finite resistive insert of finite thickness on an otherwise perfectly conducting and infinitely long round chamber. The authors conclude that even for an insert whose length is smaller than its radius, if the thickness is of the order of 100 µm, the impedance is already equal to the infinitely long chamber counterpart. This result shows that the use of the multi-layer formulas employed so far for the other components are still valid for the fast correctors chambers.

5.4 Undulators Chambers

For the first phase of operation of the Sirius light source it is planned the installation of seven IDs on the storage ring, with four different types of devices: two Delta-type undulators (TEMNYKH, 2008) and two APU (CARR, 1991). The design details as well as first experiences with the prototype measuments of the Sirius Delta undulator are described by Vilela *et al.* (2017) and the information regarding the radiation parameters of such devices can be found elsewhere (SIRIUS, 2013). All the IDs will be out of vacuum and their vacuum chamber will be made of copper and coated with NEG. Regarding the impedance issues, on the one hand this is good because it simplifies the design of the tapers, allowing further optimization of its parameters for impedance reduction, but on the other hand the resistive wall impedance will always be there, regardless of the existence or not of the additional damping provided by radiation emittion[2].

Table 5 shows the main impedance related parameters of each device type. These devices have two main source of impedance that will be modeled separately: one comes from the two tapers at both ends of the device and another from the resistive wall. The modeling of the tapers was performed with the whole collimator in the simulation, consideding perfectly conducting walls and linear transitions with factor[3] t equals to 20, which means the angle of the taper is 2.86° (50 mrad), much lower than the rule of thumb of 10°. The APU chambers were calculated with ECHOzR (ZAGORODNOV *et al.*, 2015), being modeled as flat collimators starting from a square chamber of sides equal to the radius of the real chamber and final gap equal to the Vertical BSC defined in Table 5. The Delta–type undulators are a little more complicated to model, because their final chamber geometry is an ellipse with the major and minor axes given by the horizontal and vertical BSC presented in Table 5, which invalidates the consideration of a flat geometry, due to the non–negligible horizontal tapering. We delt with this problem by simulating a round transition with ECHOz2 (ZAGORODNOV; WEILAND, 2005) and applying numerical factors given by Podobedov & Krinsky (2007, Figures 12a, 13 and 14), to the impedances. Even though their comparisons are valid for tapers with transverse sections composed by confocal ellipes, all the analytical formulas analysed in subsection 3.9.1 suggests that the parts of the tapers with lower gaps contributes more to the total impedance, which corroborates with this approach. The form factos used here were $(1, 1.3, 0.5, -0.4)$ for the longitudinal, vertical dipole, horizontal dipole and horizontal quadrupole impedances,

[2] One important remark is that both types of undulators that will be used in Sirius does not have the degree of freedom to change their gap, which means that when they are not being used there is no way to "turn off" their magnetic field. What is usually done is to change the phases among the Halbach (1985) cassets in such a way that the field lays down in the longitudinal direction, so the electron beam stops radiating.

[3] Here we recall the notation defined in subsection 3.9.1.

Table 5 – Main parameters of the Undulators for their impedance modeling.

Parameter	APU19	APU20	Delta21	Delta52	Unit
Length	2.4	2.4	2.4	3.6	m
Quant. in Phase 1	1	1	2	3	
Quant. in Phase 2	2	3	6	6	
Straight type	low–beta	high–beta	low–beta	low–beta	
Full Magnetic Gap	5	6.2	7.0	13.8	mm
Chamber thickness	0.10	0.10	0.80	1.00	mm
Hor. Beam Stay Clear	24.0	24.0	8.2	11.2	mm
Vert. Beam Stay Clear	4.8	6.0	5.0	8.0	mm
Transition factor (t)		20			

respectively.

Figure 21 shows the impedances of the four ID types before the application of the form factors on the Delta–type undulators. Also shown is the low frequency analytic expressions discussed in subsection 3.9.1. Note that in general their quantitative agreement with the numerical simulations is not very good, but the qualitative comparisons among all the types of undulators, mainly the differences between the round and flat geometry, are well predicted by the theory. In the case of the longitudinal and horizontal impedances of flat geometries this quantitative difference between theory and numerical simulations could be explained by the fact that the second condition imposed on the limits of validity of the expressions ($h \ll w$) is not met in the cases studied here, because the tapers start with a square geometry. Stupakov (2007) provides expressions for impedances for any ratio h/w, which consists on multiplying the integrands of equations (3.47) by form factor functions that depends on $h(s)/w$. The paper has graphics that explicitly show the value of these form factors and, after a qualitative analysis, it can be concluded that they justify the differences observerd here. For the vertical dipole impedance this scenario changes, because the analytic formula overestimates the impedance by a factor larger than four (they are above the upper limit of the graphic and are not shown), which is so large that even the form factors could not account for the difference observed. Maybe this disagreement, if our results are correct, comes from higher order terms in the taper angle

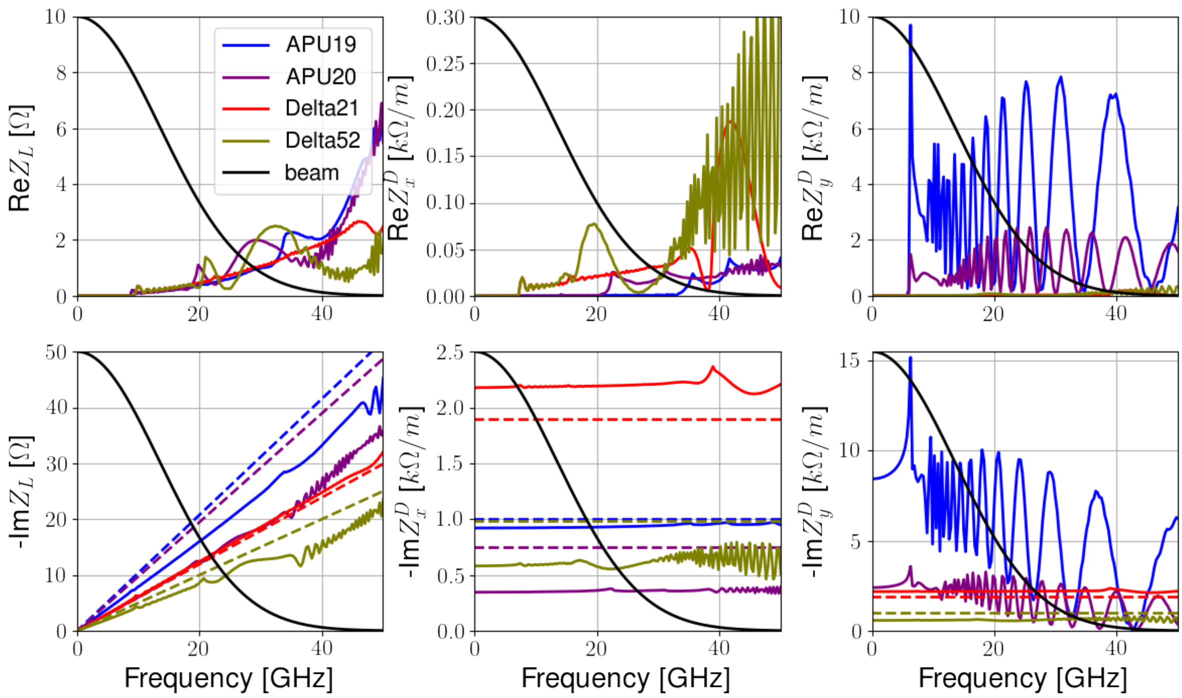

Figure 21 – Geometric impedance from the tapered transitions of the undulators. Solid lines represent numerical calculations performed with ECHOz1 and ECHOz2 for the Delta undulator and with ECHOzR for the APU. Dashed lines are the prediction by the analytic formulas studied in subsection 3.9.1.

that are not considered in the derivation of the analytic formulas.

Another interesting aspect of the numerical calculated vertical dipole impedance is the presence of the narrow–band trapped mode studied by Blednykh (2006) for the APU19. Considering that this mode depends strongly on the width of the chamber and the fact that the Sirius undulators were not desined yet, the complete effect of the this peak was not studied in details, being subject for future works. However, it was verified that it does not induce transverse coupled–bunch oscillations.

Figure 22 shows the vertical dipole and longitudinal wall impedance of the four types of undulators. They were calculated using the code ImpedanceWake2D (MOUNET, 2011) for flat multi–layer chambers. The layers used in the calculations were: NEG, Copper, air, high μ–material. The last layer was added in an attempt to consider the effect of the magnet blocks of the IDs on the zero frequency impedance, which can be noted in Figure 22b. This figure also show in dashed lines the results obtained with the calculation of the impedance using the round chamber formulas and posterior application of the YOKOYA factors. Note that for the undulators with small gap (APU19, APU20 and Delta21), this method underestimate the impedance, because the sum of the electric and magnetic LASLETT coefficients are larger than the factor for the quadrupolar impedance, but for the Delta52 both formulas agree because in this case only the electric coefficient contributes significantly and it is equal to $\pi^2/24$. Blednykh *et al.* (2016) created a more sofisticated model, where the authors considered that a fraction of the suface of the pole of the IDs was composed by the high μ–materials and the other part by saturated ferromagnet blocks, with $\mu \approx 1$. With this impedance they successfully explained the incoherent tune–shifts caused by these devices in LNLS2. Once the detailed model of the IDs are

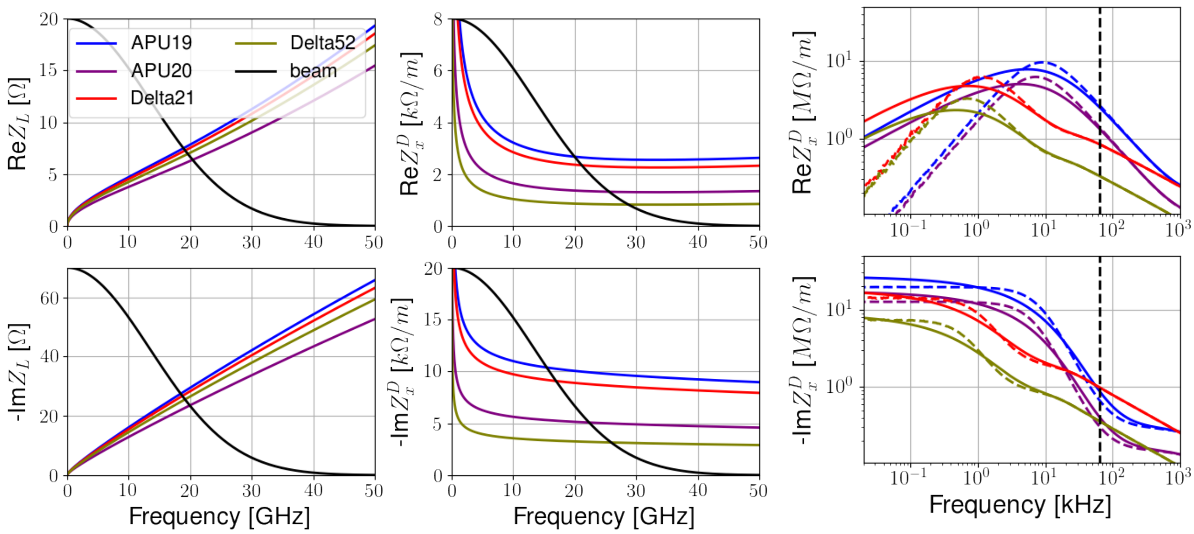

(a) High frequency impedance

(b) Low Frequency

Figure 22 – Wall impedance of the four types of undulators planned for Sirius.

available we intent to improve these components impedance model in a similar way.

The chamber heating is an important aspect to be considered in the design of the undulators, because it is difficult insert cooling systems in devices with such small gap, mainly in the Delta–type undulators, which have small appertures in both transverse directions. To estimate the power density for these devices we used the flat chamber approximation, described in equation (4.12). Even though the undulators chambers are not flat, the estimation of the peak density using this formula is a worst case scenario for the real value and, even in this case it was verified through heating simulations that the power deposited by the wake fields is not an issue.

5.5 BC Chamber

The BC magnet is the central dipole of the arch of the Sirius storage ring unit cell. It is a permanent magnet with longitudinal and transverse gradient and at its center there is a very thin slice that will reach a peak magnetic flux density of 3.2 T which will be used as source for 20 beamlines, providing radiation with critical energy of 19.2 keV. In order to achieve this high flux density, the poles of central part must be very close to the beam, with a full gap of only 10 mm.

The initial proposal for the chamber of the central section of this magnet was a elliptical chamber with inner minor semi–axis equal to 4 mm and major semi–axis equal to the radius of the standard chamber, 12 mm, connected by a smooth tapered transition with transition factor equal to 15. Motivated by the analytical formulas predicted by the theory, discussed in subsection 3.9.1, we also investigated the impedance of a round chamber with inner radius equal to the minor radius of the proposed elliptical chamber. For the impedance calculations, the elliptical chamber was approximated by a flat one and simulated using ECHOzR (ZAGORODNOV *et al.*, 2015), while the round chamber was simulated with ECHOz1 and ECHOz2 (ZAGORODNOV; WEILAND, 2005). It was known, however, that the round chamber did not meet the vacuum requirements, because the radiation generated by the upstream dipole would hit strongly the inner part of the transition in the positive (outward the storage ring center) horizontal direction, causing heating problems. For this reason, a chamber which satisfies the requirements, with a "keyhole" shape, as shown in Figure 23, was also proposed and its impedance simulated

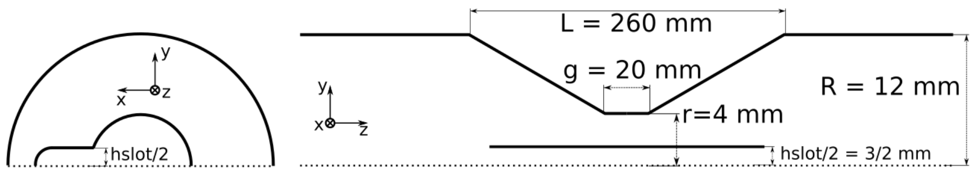

Figure 23 – Scheme of the keyhole–shaped chamber for the BC magnet.

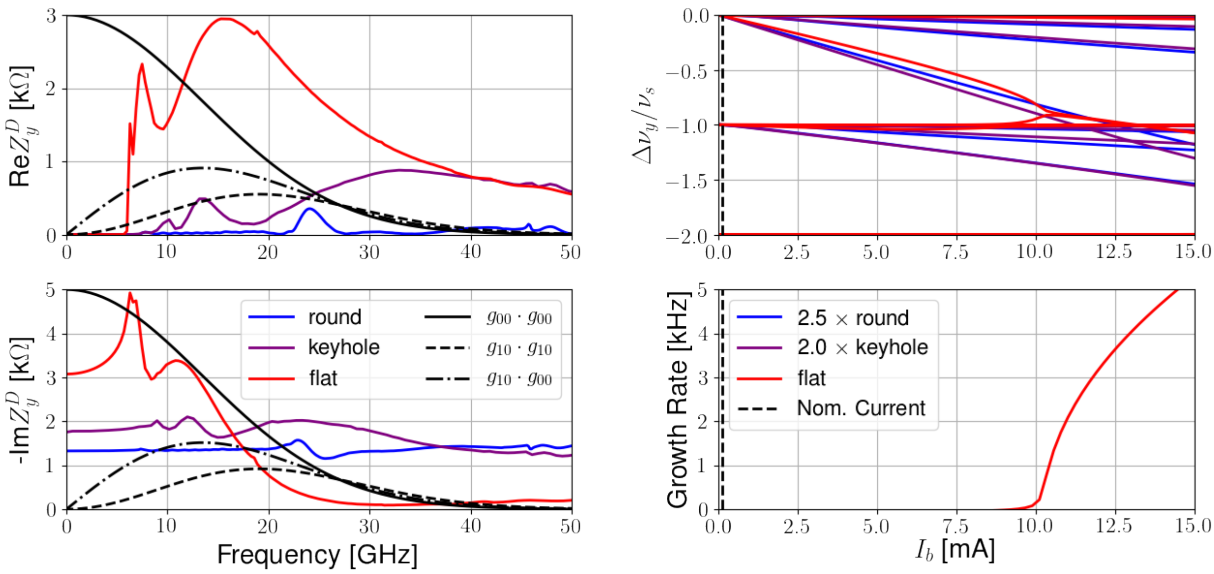

(a) Vertical Impedance (b) Vertical TMCI

Figure 24 – Comparison of the impedance and its effect on the beam through simulations of mode–coupling instability for different models of impedance. For the TMCI a gaussian single bunch with 2.5 mm root-mean-square (rms) length was considered. The impedance used was that of the 20 components along the ring, multiplied by the averave betatron function at the magnet's position.

with GdfdL (BRUNS, 2017).

Figure 24a shows the comparison of the vertical dipole impedance among the three models analysed. The theory predicts a higher low frequency inductive impedance for the flat chamber model and we note that this is indeed true. One interesting factor, however, is that the round chamber remains imaginary for all the frequency range analysed, its real part only emerges at frequencies larger than 60 GHz, while the flat chamber has a very strong real part at low frequencies, which couples with the beam oscillation mode $g_{10} \cdot g_{00}$. From the theory of mode–coupling instability, discussed in subsection **??**, we know that at zero chromaticity the imaginary part of the impedance causes tune–shifts of the coherent modes and bring them close to each other, in this case the modes 0 and -1, represented in the figure by the spectra $g_{00} \cdot g_{00}$ and $g_{10} \cdot g_{10}$, respectively; but it is the real part of the impedance that couples them causing the intability. We can see this mathematically recalling that the mode–coupling matrix has the following form, when only the modes 0 and -1 are considered

$$\frac{M}{N} \propto \begin{pmatrix} I_1 - \frac{1}{N} & R_1 \\ -R_1 & I_0 \end{pmatrix} \Rightarrow \frac{\lambda_{1,2}}{N} \propto \frac{I_0 + I_1 - \frac{1}{N}}{2} \pm \frac{1}{2}\sqrt{\left(I_1 - \frac{1}{N} - I_0\right)^2 - 4R_1^2} \tag{5.8}$$

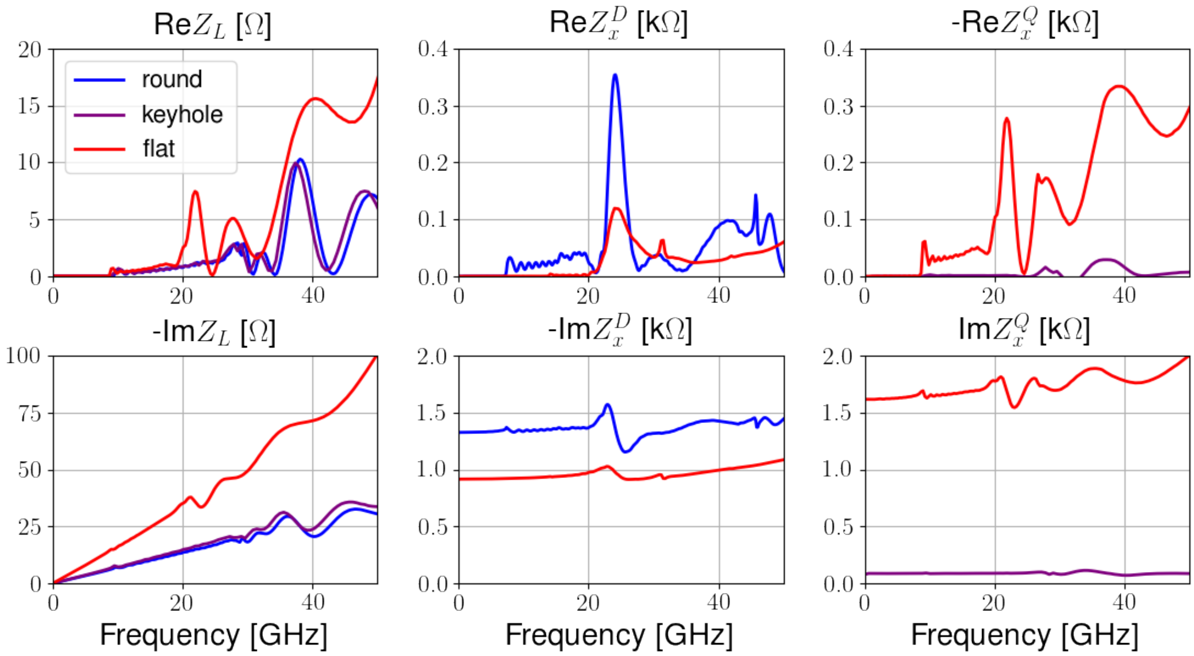

Figure 25 – Longitudinal (left), dipole horizontal (center) and quadrupole horizontal (right) impedances for the three models of BC chamber considered. The dipole horizontal impedance of the keyhole chamber was not calculated yet and the round chamber does no have a quadrupole impedance.

where N is the number of particles in the bunch,

$$I_i = \int d\omega \Im\left\{Z_y^D\right\} g_{i0} g_{i0} \tag{5.9a}$$

$$R_1 = \int d\omega \Re\left\{Z_y^D\right\} g_{10} g_{00}, \tag{5.9b}$$

and g_{ml} is given by equation (**??**). Henceforth, it is clear from the eigen–value expression in equation (5.8) that the instability can only happen if the real part of the impedance is strong enough to couple with beam in such a way that

$$2|R_1| \geq \left| I_1 - \frac{1}{N} - I_0 \right|. \tag{5.10}$$

Note that when the number of particles in the bunch is small, the r.h.s. of the inequality above is very large and when $N \to \infty$ it tends to $I_1 - I_0$. If R_1 is not larger than this difference, the modes simply cross each other. Note that some mechanism similar to the one explained above is happening in Figure 24b for the round and keyhole chambers, where even after being multiplied by a factor of 2.5 and 2.0, respectively, to match the tune–shifts, their real impedances is not strong enough to create the instability.

Figure 25 shows the other impedances for the three models. Note that the imaginary part of the longitudinal impedance of the keyhole and round models are smaller than the one of the flat chamber by a factor of approximately 2, which is accordance with the theory predictions, and the quadrupolar impedance introduced by keyhole is negligible. The horizontal dipole impedance was not calculated for this model yet, but a calculation was performed for a keyhole geometry with the *hslot*, defined in Figure 23, equals to 2 mm and it was similar to the transverse impedance of the round model.

5.6 Coherent synchrotron radiation (CSR)

The radiation emitted by one particle can influence other particles in the bunch in a similar way as the wake fields and, for this reason, is treated with the same formalism of impedances and wake functions discussed so far. Such mechanism is often refered to as CSR because its net effect is only relevant for wavelengths of the same order or larger than the bunch length, according to Nagaoka & Bane (2014). The wake function of a source particle moving in circular trajectory in free–space over a witness particle in this same trajectory was calculated by Derbenev *et al.* (1995) and is given by:

$$\frac{W_0'(z)}{L} = \begin{cases} -\dfrac{Z_0 c}{2\pi 3^{4/3}} \dfrac{1}{\rho^{2/3}(-z)^{4/3}} & z < 0 \\ 0 & z > 0 \end{cases}, \tag{5.11}$$

where ρ is the radius of curvature of the trajectory, $L = 2\pi\rho$ is the total length of the circle and, contrary to other wakes, it only affects particles ahead of the source particle. Notice that this formula not only diverges at the origin as it predicts energy gain for all ranges of interaction. This happens because this equation is only the tail of a very short–range and intense wake. This wake starts at $W_0'(0^-) \approx \gamma^4/\rho^2$, crosses zero at $-z \approx 2\rho/9\gamma^2$ and soon after that assumes the value of the asymptotic behavior described by the equation above[4]. A fast calculation shows that the short–range scales of the complete wake ($\rho/\gamma^2 \approx$500 nm for Sirius) are much smaller than any characteristic length important for the stability analysis in Sirius, which justifies the use of equation (5.11).

Murphy *et al.* (1997) calculated the wake function of the same trajectory described above, but instead of considering the particles were in free space, the authors included two infinite parallel plates equally spaced from the particles trajectory. The asymptotic form of the wake they obtained has, in addition to the term of equation (5.11), a contribution from the radiation of the image charges on the plates, given by

$$\frac{W_1'(z)}{L} = -\frac{Z_0 c}{4\pi} \frac{1}{2\pi h^2} G\left(\frac{\rho^{1/2}}{h^{3/2}} z\right), \tag{5.12}$$

where h is the distance of any one of the plates to the beam trajectory. The function G is given by

$$G(x) = 8\pi \sum_{k=1}^{\infty} \frac{(-1)^{k+1}}{k^2} \frac{Y_k(x)\,(3 - Y_k(x))}{(1 + Y_k(x))^3}, \tag{5.13}$$

[4] Figure 2 of Murphy *et al.* (1997) has a graphic of this function.

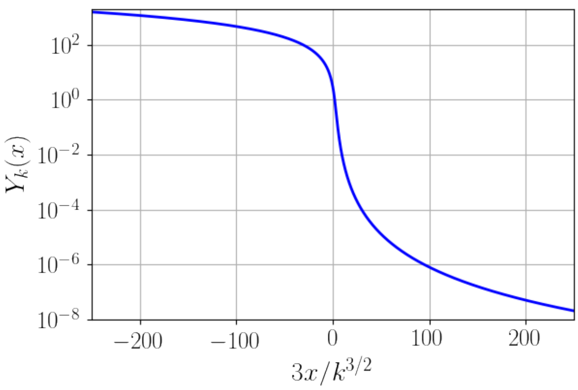

(a) lakd

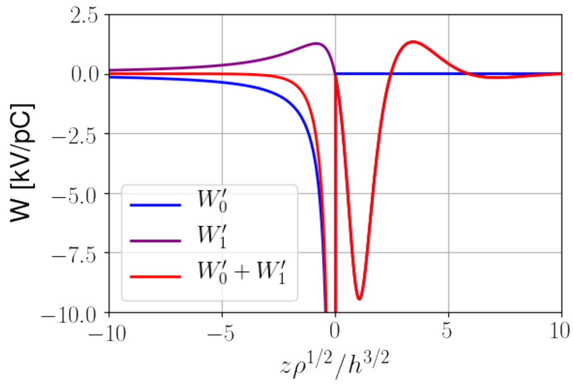

(b) lakd

with $Y_k(x)$ being one of the roots of the equation

$$Y_k - \frac{3x}{k^{3/2}} Y_k^{1/4} - 3 = 0. \tag{5.14}$$

According to Bane *et al.* (2010) from the four roots of the equation above, two are complex and two are real and we are interested in the one that gives the larger value for $Y_k(x)$ when $x < 0$, the smallest for $x > 0$ and when $x = 0$ the two real roots are equal to 3. Figure 26a shows $Y_k(x)$ as function of the term $3x/k^{3/2}$, where we note a smooth and well behaved dependency, which guarantees a fast convergence of the infinite series that defines G, being necessary to compute only the first 25 to 30 terms in almost all practical cases. Figure 26b shows the effect of the plates on the total wake, where we can note that, contrary to the free–space term, it is non–zero behind the source particle and that its contribution in the portion ahead is to cancel the long tail of the free–space wake, working as a shield for low frequency terms.

The CSR impedance with and without shielding is known for a long time, see for example the work of Faltens & Laslett (1973). The free-space impedance, corresponding to the wake given in equation (5.11) is given by (NAGAOKA; BANE, 2014, Eq. 18)

$$\frac{Z(\omega)}{L} = \frac{Z_0}{2\pi}\frac{\Gamma\left(2/3\right)}{3^{1/3}} \exp\left(\frac{i\pi}{6}\right)\left(\frac{\omega}{c\rho^2}\right)^{1/3}. \tag{5.15}$$

Calculations of the impedance of the shielded configuration with the parallel plates can be found in Warnock (1990) and Murphy *et al.* (1997). However, recently Cai (2011) presented a approximated result that he built based on the exact equations given by WARNOCK which is easy to calculate numerically and simply describes the impedance in terms of scaled results

$$\frac{\rho}{h}\frac{Z(n)}{n} = 16 Z_0 u_0 \sum_{p=0}^{\infty} \left(\mathrm{Ai}'(u_p)\mathrm{Ci}'(u_p) + u_p \mathrm{Ai}(u_p)\mathrm{Ci}(u_p)\right), \tag{5.16}$$

where $n = \omega\rho/c$, Ai and Bi are the Airy functions (Wikipedia Contributors, 2017a) and the prime denotes their derivatives, $\mathrm{Ci} = \mathrm{Ai} - i\mathrm{Bi}$ and the variable u_p is given by

$$u_p = \frac{\pi^2(2p+1)^2}{2^{2/3}}\left(n\left(\frac{2h}{\rho}\right)^{3/2}\right)^{-4/3}. \tag{5.17}$$

Using the parallel plates model for the CSR impedance Bane *et al.* (2010) calculated the threshold for the microwave instability as function of the plates separations using a Vlasov Fokker Planck (VFP) equation solver developed by Warnock & Ellison (2000) and showed that the CSR induced instability depends on only two scaled variables: the threshold strength, $(S_\mathrm{csr})_\mathrm{th}$, and the shielding parameter, Π, given by

$$(S_\mathrm{csr})_\mathrm{th} = I\frac{\rho^{1/3}}{\sigma_{z,0}^{4/3}}, \qquad \Pi = \sigma_{z,0}\frac{\rho^{1/2}}{h^{3/2}} \tag{5.18}$$

where $\sigma_{z,0}$ is the bunch length at zero current and I is a normalized bunch current (with unit of m in the International System of Units (SI)) given by

$$I = \frac{Z_0 c}{4\pi}\frac{I_0 T_0}{2\pi\nu_{s,0}\left(E_0/e\right)\sigma_{\delta,0}} \tag{5.19}$$

where N_b is the number of particles in the bunch, $\nu_{s,0}$ is the zero current synchrotron tune and $\sigma_{\delta,0}$ is the zero current energy spread. Figure 27 shows their main results, with the addition of lines indicating the shielding parameters for Sirius dipoles, where one can notice

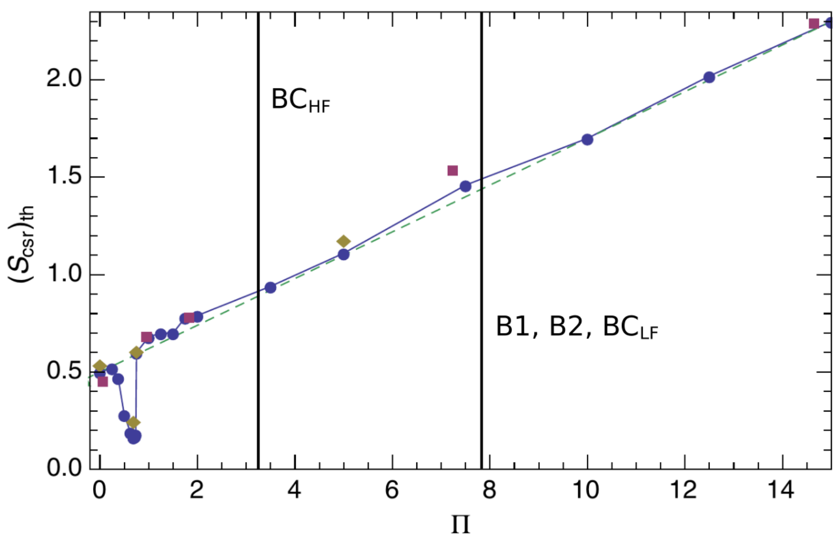

Figure 27 – Plot adapted from Bane *et al.* (2010): CSR threshold strengh, $(S_\mathrm{csr})_\mathrm{th}$, as function of the shielding parameter, Π. Blue dots: simulations with the VFP solver; red squares: results of the linearized Vlasov equation (does not include damping); olive diamonds: results with a damping factor two times larger; dashed line: the scaling $(S_\mathrm{csr})_\mathrm{th} = 0.5{+}0.12\Pi$; black lines: shielding parameters for Sirius dipoles, where line on the right is relative to B1, B2 and the low field part of the BC magnet (BC$_\mathrm{LF}$) and the one on the left is for the high field part of this same magnet (BC$_\mathrm{HF}$).

Table 6 – Main parameters used for modelling the CSR impedance and effective wake function

Parameter	B1, B2, BC_{LF}	BC_{HF}	Unit
Bending radius	17.2	3.1	m
Magnet length	0.8/1.2/0.4	0.06	m
Total deflection angle	337.6	22.4	°
Vacuum chamber radius	12	4	mm
Shielding parameter	7.8	3.4	
Threshold current	1.0	0.95	mA

the thresholds considering the whole ring is composed only with one type of dipole are $(S_{\text{csr}})_{\text{th}} = 0.90$ and $(S_{\text{csr}})_{\text{th}} = 1.5$ for the high and low field dipoles, respectively. Converting these values to bunch current with equations (5.19) and (5.18) we get approximately the same value for both cases, 1 mA.

Note that for most of the shielding range simulated, the threshold follows a simple dependency given by the line

$$(S_{\text{csr}})_{\text{th}} = 0.5 + 0.12\Pi. \tag{5.20}$$

Despite of the simple model for the impedance used in these calculations, several expirements confirmed the instability predictions above, for example the one performed at the Metrology Light Source explained by Ries *et al.* (2012) and the more recent results from ANKA, described in Brosi *et al.* (2016). However, the threshold calculated this way does not take into account the effect of other impedances, requiring a more specific study.

Inspired by these good agreements between the theory and the measuments we decided to create an initial model for the CSR impedance based on this parallel plates approximation. Table 6 shows the main parameters used for modeling the impedances and wakes for the case of the Sirius storage ring. The impedance was directly calculated from equation (5.16), but the method to obtain the wake was more envolving. Instead of the wake-function of the point charge, we convolved the the expressions of equations (5.11) and (5.12) with a small gaussian beam of $\sigma = 80$ µm to avoid the divergence of the free–space wake and used this effective wake function as input for tracking simulations. The convolution with the shielded contribution to the impedance was done in the standard way, but the one with the free–space contribution was performed following the trick described by Nagaoka & Bane (2014)

$$V_0(z) = -\int_{-\infty}^{0} \mathrm{d}z' W_0'(z')\lambda(z-z') = \int_{-\infty}^{0} \mathrm{d}z' W_0(z')\lambda'(z-z') \tag{5.21}$$

where

$$\frac{W_0(z)}{L} = \begin{cases} \dfrac{Z_0 c}{2\pi 3^{1/3}} \dfrac{1}{\rho^{2/3}(-z)^{1/3}} & z < 0 \\ 0 & z > 0 \end{cases} \quad \text{and} \quad \lambda(z) = \frac{1}{\sqrt{2\pi}\sigma} \exp\left(-\frac{z^2}{2\sigma^2}\right). \tag{5.22}$$

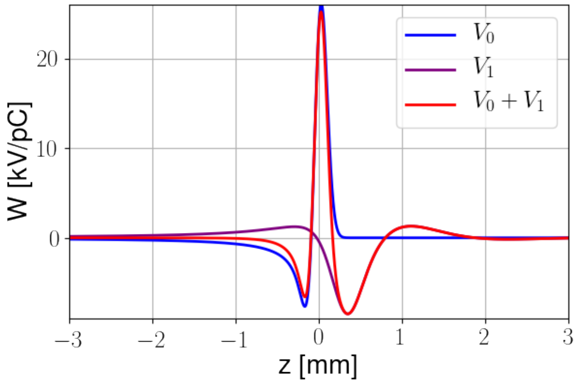

(a) lakd

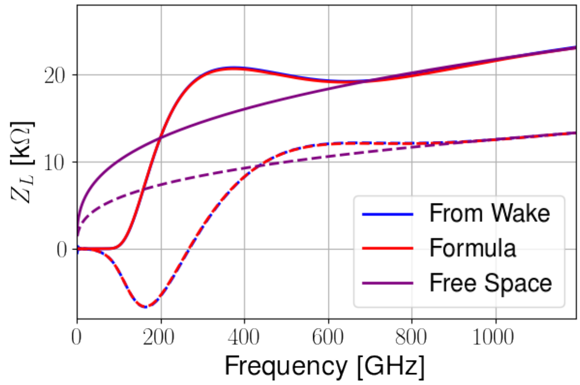

(b) lakd

Note that $W_0(z)$ also diverges at the origin, but slower, in such a way that the convolution can be carried out numerically or analytically. The analytic result was obtained with Wolfram Mathematica (Wolfram Research Inc., 2016) and it reads

$$V_0(z) = \frac{Z_0 c}{\pi^{3/2}(12\rho^2\sigma^{10})^{1/3}} \left\{ \sqrt{2}\Gamma\left(\frac{5}{6}\right)\left(\sigma^2\,{}_1\mathrm{F}_1\left(-\frac{1}{3};\frac{1}{2};-\frac{z^2}{2\sigma^2}\right) - z^2\,{}_1\mathrm{F}_1\left(\frac{2}{3};\frac{3}{2};-\frac{z^2}{2\sigma^2}\right)\right)\right.$$
$$\left. + z\sigma\Gamma\left(\frac{4}{3}\right)\left(3\,{}_1\mathrm{F}_1\left(\frac{1}{6};\frac{1}{2};-\frac{z^2}{2\sigma^2}\right) - 2\,{}_1\mathrm{F}_1\left(\frac{1}{6};\frac{3}{2};-\frac{z^2}{2\sigma^2}\right)\right)\right\},$$

where ${}_1\mathrm{F}_1$ is the confluent hypergeometric function (Wikipedia Contributors, 2017b). Figure 28a shows the two components of the wake and their sum, while Figure 28b shows the impedance calculated via the Inverse Fourier Transform and posterior deconvolution of equation (5.21) compared with the calculation using equation (5.16) and the free-space impedance (5.15)

6 IMPEDANCE BUDGET

6.1 Longitudinal Impedance

6.1.1 Effective Z/n

6.1.2 Multi-bunch Kloss and Dissipated Power

6.2 Vertical Impedance

6.3 Horizontal Impedance

7 SIMULATIONS AND INSTABILITIES THRESHOLDS

7.1 Frequency Domain Calculations

7.1.1 Vertical Plane

7.1.1.1 Single-bunch Tune–Shifts

7.1.1.2 Multi-bunch Tune–Shifts

7.1.1.3 Coupled-Bunch Instabilities

7.1.1.4 Single-Bunch Instabilities

7.1.2 Horizontal Plane

7.1.2.1 Single-bunch Tune–Shifts

7.1.2.2 Multi-bunch Tune–Shifts

7.1.2.3 Coupled-Bunch Instabilities

7.1.2.4 Single-Bunch Instabilities

7.1.3 Longitudinal Plane

7.1.3.1 Multi-Bunch Instabilities

7.1.3.2 Single-Bunch Instabilities

7.2 Time Domain Calculations

7.2.1 Longitudinal Plane

7.2.2 Vertical Plane

7.2.3 Horizontal Plane

CONCLUSÃO

Lorem ipsum dolor sit amet, consectetuer adipiscing elit. Ut purus elit, vestibulum ut, placerat ac, adipiscing vitae, felis. Curabitur dictum gravida mauris. Nam arcu libero, nonummy eget, consectetuer id, vulputate a, magna. Donec vehicula augue eu neque. Pellentesque habitant morbi tristique senectus et netus et malesuada fames ac turpis egestas. Mauris ut leo. Cras viverra metus rhoncus sem. Nulla et lectus vestibulum urna fringilla ultrices. Phasellus eu tellus sit amet tortor gravida placerat. Integer sapien est, iaculis in, pretium quis, viverra ac, nunc. Praesent eget sem vel leo ultrices bibendum. Aenean faucibus. Morbi dolor nulla, malesuada eu, pulvinar at, mollis ac, nulla. Curabitur auctor semper nulla. Donec varius orci eget risus. Duis nibh mi, congue eu, accumsan eleifend, sagittis quis, diam. Duis eget orci sit amet orci dignissim rutrum.

Nam dui ligula, fringilla a, euismod sodales, sollicitudin vel, wisi. Morbi auctor lorem non justo. Nam lacus libero, pretium at, lobortis vitae, ultricies et, tellus. Donec aliquet, tortor sed accumsan bibendum, erat ligula aliquet magna, vitae ornare odio metus a mi. Morbi ac orci et nisl hendrerit mollis. Suspendisse ut massa. Cras nec ante. Pellentesque a nulla. Cum sociis natoque penatibus et magnis dis parturient montes, nascetur ridiculus mus. Aliquam tincidunt urna. Nulla ullamcorper vestibulum turpis. Pellentesque cursus luctus mauris.

Nulla malesuada porttitor diam. Donec felis erat, congue non, volutpat at, tincidunt tristique, libero. Vivamus viverra fermentum felis. Donec nonummy pellentesque ante. Phasellus adipiscing semper elit. Proin fermentum massa ac quam. Sed diam turpis, molestie vitae, placerat a, molestie nec, leo. Maecenas lacinia. Nam ipsum ligula, eleifend at, accumsan nec, suscipit a, ipsum. Morbi blandit ligula feugiat magna. Nunc eleifend consequat lorem. Sed lacinia nulla vitae enim. Pellentesque tincidunt purus vel magna. Integer non enim. Praesent euismod nunc eu purus. Donec bibendum quam in tellus. Nullam cursus pulvinar lectus. Donec et mi. Nam vulputate metus eu enim. Vestibulum pellentesque felis eu massa.

Quisque ullamcorper placerat ipsum. Cras nibh. Morbi vel justo vitae lacus tincidunt ultrices. Lorem ipsum dolor sit amet, consectetuer adipiscing elit. In hac habitasse platea dictumst. Integer tempus convallis augue. Etiam facilisis. Nunc elementum fermentum wisi. Aenean placerat. Ut imperdiet, enim sed gravida sollicitudin, felis odio placerat quam, ac pulvinar elit purus eget enim. Nunc vitae tortor. Proin tempus nibh sit amet nisl. Vivamus quis tortor vitae risus porta vehicula.

Fusce mauris. Vestibulum luctus nibh at lectus. Sed bibendum, nulla a faucibus semper, leo velit ultricies tellus, ac venenatis arcu wisi vel nisl. Vestibulum diam. Aliquam pellentesque, augue quis sagittis posuere, turpis lacus congue quam, in hendrerit risus eros eget felis. Maecenas eget erat in sapien mattis porttitor. Vestibulum porttitor. Nulla facilisi. Sed a turpis eu lacus commodo facilisis. Morbi fringilla, wisi in dignissim interdum, justo lectus sagittis dui, et vehicula libero dui cursus dui. Mauris tempor ligula sed lacus. Duis cursus enim ut augue. Cras ac magna. Cras nulla. Nulla egestas. Curabitur a leo. Quisque egestas wisi eget nunc. Nam feugiat lacus vel est. Curabitur consectetuer.

BIBLIOGRAPHY

AL-DMOUR, E. *et al.* Diffraction-limited storage-ring vacuum technology. *Journal of Synchrotron Radiation*, International Union of Crystallography, v. 21, n. 5, p. 878–883, 2014. ISSN 1600-5775. Disponível em: <http://scripts.iucr.org/cgi-bin/paper?S1600577514010480>. 28

AL-KHATEEB, A. M. *et al.* Longitudinal impedance and shielding effectiveness of a resistive beam pipe for arbitrary energy and frequency. *Physical Review E*, v. 71, p. 026501, 2005. ISSN 0094243X. 74

BANE, K.; STUPAKOV, G.; ZAGORODNOV, I. Impedance calculations of nonaxisymmetric transitions using the optical approximation. *Physical Review Special Topics - Accelerators and Beams*, v. 10, n. 7, p. 074401, 2007. ISSN 1098-4402. Disponível em: <http://link.aps.org/doi/10.1103/PhysRevSTAB.10.074401>. 69

BANE, K. L. F. *The short range resistive wall wakefields*. Stanford, 1991. 26 p. 72

BANE, K. L. F.; CAI, Y.; STUPAKOV, G. Threshold Studies of the Microwave Instability in Electron Storage Rings. *Physical Review Special Topics - Accelerators and Beams*, v. 13, n. 10, p. 104402, 2010. ISSN 10984402. 11, 107, 108

BANE, K. L. F.; NG, C. K.; CHAO, A. W. Estimate of the impedance due to wall surface roughness. *Proceedings of PAC 1997*, p. 1738–1740, 1997. Disponível em: <http://ieeexplore.ieee.org/xpls/abs{_}all.jsp?arnumber=750>. 87

BANE, K. L. F.; RUTH, R. D. Bunch Lengthenning Calculations for the SLC Dampling Rings. In: *Proceedings of PAC 1989*. [S.l.: s.n.], 1989. p. 789–791. 58, 150

BARTY, A. Single molecule imaging using X-ray free electron lasers. *Current Opinion in Structural Biology*, Elsevier Ltd, v. 40, p. 186–194, 2016. ISSN 1879033X. Disponível em: <http://dx.doi.org/10.1016/j.sbi.2016.11.017>. 18

BARTY, A.; KÜPPER, J.; CHAPMAN, H. N. Molecular Imaging Using X-Ray Free-Electron Lasers. *Annual Review of Physical Chemistry*, v. 64, n. 1, p. 415–435, 2013. ISSN 0066-426X. Disponível em: <http://www.annualreviews.org/doi/10.1146/annurev-physchem-032511-143708>. 18

BASSI, G. *et al. Analysis of coupled-bunch instabilities for the NSLS-II storage ring with a 500 MHz 7-cell PETRA-III cavity*. Upton, 2015. 151–163 p. 150, 151

BENGTSSON, J. *Sextupole Scheme for the Swiss Light Source (SLS): An Analytic Approach*. Villigen, 1997. 39, 44

BENVENUTI, C. A New Pumping Approach for the Large Electron Positron Collider (LEP). *Nuclear Instruments and Methods*, v. 205, p. 391–401, 1983. 29

BENVENUTI, C. *et al.* Decreasing surface outgassing by thin film getter coatings. *Vacuum*, v. 50, n. 1-2, p. 57–63, 1998. ISSN 0042207X. Disponível em: <http://www.scopus.com/inward/record.url?eid=2-s2.0-0032058258{&}partnerID=tZOtx>. 86

BERG, J. S. *Coherent modes for multiple non-rigid bunches in a storage ring.* Tese (Doutorado) — Stanford University, 1996. 43, 82

BIRDSALL, C. K.; BREWER, G. R.; HAEFF, A. V. The Resistive-Wall Amplifier. *Proceedings of the IRE*, v. 41, n. 7, p. 865–875, 1953. ISSN 0096-8390. Disponível em: <http://ieeexplore.ieee.org/lpdocs/epic03/wrapper.htm?arnumber=4051404>. 72

BJORKEN, J. D.; MTINGWA, S. Intrabeam Scattering. *Particle Accelerators*, v. 13, p. 115–143, 1983. ISSN 0094243X. 30

BLEDNYKH, A. Trapped modes in tapered vacuum chambers for a mini-gap undulator magnet. *Nuclear Instruments and Methods in Physics Research, Section A: Accelerators, Spectrometers, Detectors and Associated Equipment*, v. 565, n. 2, p. 380–393, 2006. ISSN 01689002. 71, 102

BLEDNYKH, A. *et al.* Low-frequency quadrupole impedance of undulators and wigglers. *Physical Review Accelerators and Beams*, v. 19, n. 10, p. 104401, 2016. ISSN 24699888. 55, 102

BLEDNYKH, A.; FERREIRA, M. J.; KRINSKY, S. Impedance Calculations for the Nsls-Ii Storage Ring. In: *Proceedings of PAC09*. Vancouver: [s.n.], 2009. D04, p. 4595–4597. 29

BLEDNYKH, A.; KRINSKY, S. Preliminary impedance budget for NSLS-II storage ring. In: *Proceedings of PAC07*. Albuquerque: [s.n.], 2007. v. 05-D04, p. 4321–4323. ISBN 1424409179. 29

BORLAND, M. Elegant: A Flexible SDDS-Compliant Code for Accelerator Simulation. In: *Proceedings of ICAP 2000*. Darmstadt: [s.n.], 2000. Disponível em: <http://www.osti.gov/bridge/product.biblio.jsp?osti{_}id=761>. 151

BORLAND, M. *et al.* Lattice design challenges for fourth-generation storage-ring light sources. *Journal of Synchrotron Radiation*, International Union of Crystallography, v. 21, n. 5, p. 912–936, 2014. ISSN 16005775. 28, 29, 36

BROSI, M. *et al.* Systematic Studies of Short Bunch-Length Bursting At Anka. In: *Proceedings of IPAC 2016*. Busan: [s.n.], 2016. p. 1662–1665. ISBN 9783954501472. 109

BRUNS, W. GdfidL: a finite difference program with reduced memory and CPU usage. *Proceedings of PAC 1997*, p. 2651–2653, 1997. 78

BRUNS, W. *GdfidL Web Page*. 2017. Disponível em: <http://www.gdfidl.de/>. 78, 104

BUROV, A.; LEBEDEV, V. TRANSVERSE RESISTIVE WALL IMPEDANCE FOR MULTI-LAYER FLAT CHAMBERS. In: *Proceedings of EPAC2002*. Paris: [s.n.], 2002. v. 12, n. 7, p. 1455–1457. 74

BUROV, A.; LEBEDEV, V. Transverse Resistive Wall Impedance for Multi-Layer Round Chambers. In: *Proceedings of EPAC2002*. Paris: [s.n.], 2002. v. 1, p. 1452–1454. 74

BYRD, J. *et al.* Observation of Broadband Self-Amplified Spontaneous Coherent Terahertz Synchrotron Radiation in a Storage Ring. *Physical Review Letters*, v. 89, n. 22, p. 224801, nov 2002. ISSN 0031-9007. Disponível em: <http://link.aps.org/doi/10.1103/PhysRevLett.89.224801>. 30

CAI, Y. A Linear Theory of Microwave Instability in Electron Storage Rings. *Physical Review Special Topics - Accelerators and Beams*, v. 14, n. 6, p. 061002, 2011. 107

CARR, R. Adjustable phase insertion devices as X-ray sources. *Nuclear Inst. and Methods in Physics Research A*, v. 306, n. 1-2, p. 391–396, 1991. ISSN 01689002. 99

Ceramic Magnets. *CMD5005 Datasheet*. 2017. Disponível em: <http://www.cmi-ferrite.com/Materials/Datasheets/NiZn/CMD5005.pdf>. 94

CHAO, A. W. *Physics of Collective Beam Instabilities in High Energy Accelerators*. 1st. ed. New York: John Wiley & Sons, 1993. 371 p. (Wiley Series in Beam Physics and Accelerators Technology). ISBN 0471551848. 61, 62, 67, 72

CHAO, A. W.; HEIFETS, S.; ZOTTER, B. Tune shifts of bunch trains due to resistive vacuum chambers without circular symmetry. *Physical Review Special Topics - Accelerators and Beams*, v. 5, n. 11, p. 111001, 2002. 73, 90

CHIN, Y. H. *User's Guide for ABCI Version 8.7 (Azimuthal Beam Cavity Interaction*. Geneva, 1994. 1—-74 p. Disponível em: <http://cds.cern.ch/record/259547/files/CM-P00061200.pdf?version=1>. 76

COURANT, E.; SNYDER, H. Theory of the alternating-gradient synchrotron. *Annals of Physics*, v. 3, n. 1, p. 1–48, 1958. ISSN 00034916. 40, 48

COURANT, E. D.; SESSLER, A. M. Transverse coherent resistive instabilities of azimuthally bunched beams in particle accelerators. *Review of Scientific Instruments*, v. 37, n. 11, p. 1579–1588, 1966. ISSN 00346748. 72

CST. *CST–Particle Studio*. 2017. Disponível em: <https://www.cst.com/products/cstps>. 78

DANILOV, V. V. Extended definitions of wake fields and their influence on beam dynamics. *Physical Review Special Topics - Accelerators and Beams*, v. 3, n. 1, p. 1–5, 2000. ISSN 1098-4402. Disponível em: <http://link.aps.org/doi/10.1103/PhysRevSTAB.3.014201>. 56

DANILOV, V. V. *et al.* Experimental Study of Collective Effects in BEP Storage Ring with High Stored Current. In: *Proceedings of PAC 1993*. [S.l.: s.n.], 1993. p. 3711–3713. 56

DAVINO, D.; HAHN, H. Improved Analytical Model of the Transverse Coupling Impedance of Ferrite Kicker Magnets. *Physical Review Special Topics - Accelerators and Beams*, v. 6, n. 1, p. 012001, 2003. 66, 94

DENES, P.; SCHMITT, B. Pixel detectors for diffraction-limited storage rings. *Journal of Synchrotron Radiation*, International Union of Crystallography, v. 21, n. 5, p. 1006–1010, 2014. ISSN 16005775. 29

DERBENEV, Y. S. *et al. Microbunch Radiative Tail-Head Interaction*. Hamburg, 1995. 30, 59, 106

DESTER, P. S.; SÁ, F. H. de; LIU, L. Energy Acceptance and on Momentum Aperture Optimization for the Sirius Project. In: *Proceedings of IPAC2017*. Copenhagen: [s.n.], 2017. v. 05-D02, p. 3041–3044. ISBN 9783954501823. 33

ERIKSSON, M.; Van Der Veen, J. F.; QUITMANN, C. Diffraction-limited storage rings-A window to the science of tomorrow. *Journal of Synchrotron Radiation*, International Union of Crystallography, v. 21, n. 5, p. 837–842, 2014. ISSN 16005775. 28

FALTENS, A.; LASLETT, L. J. Longitudinal Coupling Impedance of a Stationary Electron Ring in a Cylindrical Geometry. *Particle Accelerators*, v. 4, p. 1–24, 1973. Disponível em: <papers2://publication/uuid/9400908E-3087-41D5-9EE9-CA66BB81BF1B>. 107

FARVACQUE, L. *et al.* a Low-Emittance Lattice for the E.S.R.F. In: *Proceedings of IPAC 2013*. Shanghai: [s.n.], 2013. p. 79–81. ISBN 9783954501229. 23

FRENET, F. Sur les courbes à double courbure. *Journal de Mathématiques Pures et Appliquées*, v. 17, p. 437–447, 1852. ISSN 0021-7874. Disponível em: <http://eudml.org/doc/233946>. 36

GLUCKSTERN, R. L. *Analytic methods for calculating coupling impedances*. Geneva, 2000. 67

GLUCKSTERN, R. L.; ZEIJTS, J. V.; ZOTTER, B. Coupling Impedance of beam pipes of general cross section. *Phys. Rev. E*, v. 47, n. 1, p. 656–663, 1993. Disponível em: <http://dx.doi.org/10.1103/PhysRevE.47.656>. 72, 90

GÜNZEL, T. F. Transverse coupling impedance of the storage ring at the European Synchrotron Radiation Facility. *Physical Review Special Topics - Accelerators and Beams*, v. 9, n. 11, p. 114402, 2006. 68

GÜNZEL, T. F.; PEREZ, F. Impedance and Instabilities for the ALBA Storage Ring. In: *Proceedings of EPAC08*. Genoa: [s.n.], 2008. v. 05-D04, p. 1622–1624. 29, 68

HAHN, H. *Matrix solution to longitudinal impedance of multi-layer circular structures*. Upton, 2008. 12 p. 74

HAHN, H.; DAVINO, D. RHIC Abort Kicker with Reduced Coupling Impedance. In: *Proceedings of EPAC 2002*. Paris: [s.n.], 2002. p. 1502–1504. 94

HAÏSSINSKI, J. Exact Longitudinal Equilibrium Distribution of Stored Electrons in the Presence of Self-fields. *Il Nuovo Cimento*, v. 18, n. 1, p. 72–82, 1973. ISSN 03693554. 83

HALBACH, K. Applications of Permanent Magnets in Accelerators and Electron Storage Rings. *Journal of Applied Physics*, v. 57, n. 1, p. 3605, 1985. 100

HEIFETS, S. *Tune Shift due to Asymmetry of the Resistive Beam Pipe*. Stanford, 1998. 7 p. 90

HEIFETS, S. A. *On the Direction Symmetry of the Impedance*. Stanford, 1990. 1—-5 p. 69, 71

HEIFETS, S. A.; KHEIFETS, S. A. Coupling impedance in modern accelerators. *Reviews of Modern Physics*, v. 63, n. 3, p. 633–673, 1991. 61, 69

HETTEL, R. O. Challenges in the Design of Diffraction-Limited Storage Rings. In: *Proceedings of IPAC2014*. Dresden: [s.n.], 2014. v. 02-A16, p. 7–11. ISBN 9783954501328. 29

HETTEL, R. O. DLSR design and plans: An international overview. *Journal of Synchrotron Radiation*, International Union of Crystallography, v. 21, n. 5, p. 843–855, 2014. ISSN 16005775. 25, 28

HITCHCOCK, A. P.; TONEY, M. F. Spectromicroscopy and coherent diffraction imaging: Focus on energy materials applications. *Journal of Synchrotron Radiation*, International Union of Crystallography, v. 21, n. 5, p. 1019–1030, 2014. ISSN 16005775. 28

HUANG, Z. Brightness and Coherence of Synchrotron Radiation and FELs. In: *Proceedings of IPAC 2013*. Shanghai: [s.n.], 2013. p. 16–20. ISBN 9783954501229. Disponível em: <http://epaper.kek.jp/IPAC2013/papers/moycb101.pdf>. 26, 28

JACKSON, J. D. *Classical Electrodynamics*. 2nd. ed. New York: John Wiley & Sons, 1962. 848 p. 46, 54

JOHANSSON, L. C. *et al.* A Bright Future for Serial Femtosecond Crystallography with XFELs. *Trends in Biochemical Sciences*, Elsevier Ltd, v. 42, n. 9, p. 749–762, 2017. ISSN 13624326. Disponível em: <http://dx.doi.org/10.1016/j.tibs.2017.06.007>. 18

JOHANSSON, M.; ANDERBERG, B.; LINDGREN, L. J. Magnet design for a low-emittance storage ring. *Journal of Synchrotron Radiation*, International Union of Crystallography, v. 21, n. 5, p. 884–903, 2014. ISSN 16005775. 28

JONES, R. M.; KROLL, N. M.; MILLER, R. H. Spectral Function Calculation of Angle Wakes, Wake Moments, and Misalignment Wakes for the SLAC Damped Detuned Structures (DDS). In: *Proceedings of PAC 1997*. [S.l.: s.n.], 1998. p. 551–553. ISBN 078034376X. 56

KARANTZOULIS, E.; SMALUK, V.; TOSI, L. Broad band impedance measurements on the electron storage ring ELETTRA. *Physical Review Special Topics - Accelerators and Beams*, v. 6, n. 3, p. 36–43, 2003. ISSN 10984402. 86

KLEIN, M. *et al.* STUDY OF COLLECTIVE BEAM INSTABILITIES FOR THE MAX IV 3 G e V RING. In: *InProceedings of IPAC 2013*. Shanghai: [s.n.], 2013. v. 05-D05, p. 1730–1732. ISBN 9783954501229. 29

KOUKOVINI-PLATIA, E.; RUMOLO, G.; ZANNINI, C. High Frequency electromagnetic Characterization of NEG Properties for the CLIC Damping Rings. In: *Proceedings of IPAC2014*. Dresden: [s.n.], 2014. v. 07-T14, p. 3097–3099. ISBN 9783954501687. 87

KRONIG, R. d. L. On the Theory of Dispersion of X-Rays. *J. Opt. Soc. Am.*, v. 12, n. 6, p. 547—-557, 1926. Disponível em: <http://www.osapublishing.org/abstract.cfm?URI=josa-12-6-547>. 62

KUBO, K.; OIDE, K.; INTRODUCTION, I. Intrabeam Scattering in Electron Storage Rings. *Physical Review Special Topics - Accelerators and Beams*, v. 4, n. September, p. 124401, 2001. ISSN 1098-4402. 30

LANDAU, L. D.; LIFSHITZ, E. *Physical Kinetics (Course of Theoretical Physics, Vol 10)*. [S.l.]: Pergamon Press Ltd., 1981. 452 p. ISBN 0080264808. 50

LANDAU, L. D.; LIFSHITZ, E. M. *Electrodynamics of Continuous Media (Course of Theoretical Physics, Vol 8)*. Pergamon Press Ltd., 1960. 429 p. ISSN 0002-9505. ISBN 0750626348. Disponível em: <http://aapt.scitation.org/doi/10.1119/1.1937882>. 82

LASLETT, L. J. *On Intensity Limitations Imposed by Transverse Space-Charge Effects in Circular Particle Accelerators*. Upton, 1963. 324–367 p. Disponível em: <http://lss.fnal.gov/conf/C630610/p324.pdf>. 31, 91, 92, 98, 102

LASLETT, L. J.; NEIL, V. K.; SESSLER, A. M. Transverse Resistive Instabilities of Intense Coasting Beams in Particle Accelerators. *Review of Scientific Instruments*, v. 36, n. 4, p. 436–448, 1965. 72

LEE, S. Y. *Accelerator Physics*. 1st. ed. Singapore: World Scientific Publishing Co. Pte. Ltd., 1999. 491 p. ISBN 981023709X. 36, 37, 39, 50

LEEMANN, S. C. *et al.* Beam dynamics and expected performance of Sweden's new storage-ring light source: MAX IV. *Physical Review Special Topics - Accelerators and Beams*, v. 12, n. 12, p. 120701, 2009. ISSN 1098-4402. Disponível em: <http://link.aps.org/doi/10.1103/PhysRevSTAB.12.120701>. 23, 32

LINDBERG, R. R. Fokker-Planck analysis of transverse collective instabilities in electron storage rings. *Phys. Rev. Accel. Beams*, v. 19, n. 12, p. 124402, 2016. Disponível em: <https://link.aps.org/doi/10.1103/PhysRevAccelBeams.19.124402>. 50, 51, 82

LINDBERG, R. R.; BLEDNYKH, A. Modeling of Impedance Effects for the APS-MBA Upgrade. In: *Proceedings of IPAC2015*. Richmond: [s.n.], 2015. v. 02-A05, p. 1825–1827. ISBN 9783954501687. 29

LIU, L. *et al.* Status of Sirius - A New Brazilian Synchrotron Light Source. In: *Proceedings of IPAC2011*. San Sebastián: [s.n.], 2011. v. 02-A05, p. 931–933. 32

LIU, L. *et al.* Update on Sirius, the New Brazilian Light Source. In: *Proceedings of IPAC2014*. Dresden: [s.n.], 2014. v. 02-A05, p. 191–193. ISBN 9783954501328. 32

LIU, L. *et al.* a New 5Ba Low Emittance Lattice for Sirius. In: *Proceedings of IPAC2013*. Shanghai: [s.n.], 2013. v. 05-D01, p. 1874–1876. ISBN 9783954501229. 32

LIU, L.; RESENDE, X. R.; RODRIGUES, A. R. D. Sirius (BR): A New Brazilian Synchrotron Light Source. In: *Proceedings of IPAC'10*. Kyoto: [s.n.], 2010. v. 02-A05, p. 2481–2483. ISBN 9789290833529. 32

LIU, L. *et al.* Upgraded Optics for Sirius With Improved Matching of Electron and Photon Beam Emittances. In: *Proceedings of IPAC2015*. Richmond: [s.n.], 2015. v. 02-A05, p. 1407–1409. ISBN 9783954501687. 32

LIU, L.; SÁ, F. H. de; RESENDE, X. R. A New Optics for Sirius. In: *Proceedings of IPAC2016*. Busan: [s.n.], 2016. v. 05-D01, p. 3413–3415. ISBN 9783954501472. 32, 33

LIU, L. *et al.* Injection Dynamics for Sirius Using a Nonlinear Kicker. In: *Proceedings of IPAC2016*. Busan: [s.n.], 2016. v. 05-D02, p. 3406–3408. ISBN 9783954501472. 34, 92

LIU, L.; WESTFAHL, H. Towards Diffraction Limited Storage Ring Based Light Sources. In: *Proceedings of IPAC2017*. Copenhagen: [s.n.], 2017. p. 1203–1208. ISBN 9783954501823. 27, 28

MARX, V. Structural biology: Doors open at the European XFEL. *Nature Methods*, Nature Publishing Group, v. 14, n. 9, p. 843–846, 2017. ISSN 15487105. Disponível em: <http://dx.doi.org/10.1038/nmeth.4394>. 18

MCNEIL, B. W. J.; THOMPSON, N. R. X-ray free-electron lasers. *Nature Photonics*, Nature Publishing Group, v. 4, n. 12, p. 814–821, 2010. ISSN 1749-4885. Disponível em: <http://www.nature.com/doifinder/10.1038/nphoton.2010.239>. 18

MOSTACCI, A.; CASPERS, F. Beam-Coupling Impedance and Wake Field — Bench Measurements. *IFCA Beam Dynamics Newsletter No. 69*, Geneva, p. 88—-96, 2016. 94

MOUNET, N. *ImpedanceWake2D*. 2011. Disponível em: <https://twiki.cern.ch/twiki/bin/view/ABPComputing/ImpedanceWake2D>. 74, 102

MOUNET, N. *The LHC Transverse Coupled-Bunch Instability*. Tese (phdthesis) — École Polytechinique Fédérale de Lausanne, 2012. 74

MOUNET, N.; MÉTRAL, E. *Electromagnetic field created by a macroparticle in an infinitel long and axisymmetric multilayer beam pipe*. Geneva, 2009. 74

MOUNET, N.; MÉTRAL, E. *Electromagnetic fields and beam coupling impedances in a multilayer flat chamber*. Geneva, 2010. 74

MOUNET, N.; MÉTRAL, E. Impedances of Two Dimensional Multilayer Cylindrical and Flat Chambers in the Non-ultrarelativistic Case. In: *Proceedings of HB 2010*. Morschach: [s.n.], 2010. p. 353–357. 74

MURPHY, J. B.; KRINSKY, S.; GLUCKSTERN, R. L. Longitudinal Wakefield for an Electron moving on a Circular Orbit. *Particle Accelerators*, v. 57, n. BNL-63090, p. 9–64, 1997. 30, 106, 107

NAGAOKA, R. Impact of Resistive–Wall Wake Fields Generated by Low–Gap Chambers on the Beam at the ESRF. In: *Proceedings of PAC 2001*. Chicago: IEEE, 2001. p. 3531–3533. ISBN 0780371917. 90

NAGAOKA, R. Numerical Evaluation of Geometric Impedance for Soleil. In: *proceedings of EPAC 2004*. Lucerne: [s.n.], 2004. p. 2041–2043. 29

NAGAOKA, R. Study of Resistive-Wall Effects on Soleil. In: *Proceedings of EPAC 2004*. Lucerne: [s.n.], 2004. p. 2038–2040. 86

NAGAOKA, R. Instability Studies Using Evaluated Wake Fields and Comparison With Observations at Soleil. In: *Proceedings of EPAC 2006*. Edinburgh: [s.n.], 2006. v. 05-D04, p. 2847–2849. 82

NAGAOKA, R.; BANE, K. L. F. Collective effects in a diffraction-limited storage ring. *Journal of Synchrotron Radiation*, v. 21, n. 5, p. 937–960, 2014. Disponível em: <https://doi.org/10.1107/S1600577514015215>. 29, 30, 34, 86, 106, 107, 109

NAGAOKA, R. *et al.* Beam Instability Observations and Analysis at Soleil. In: *Proceedings of PAC 2007*. Albuquerque: [s.n.], 2007. v. 05-D04, p. 2019–2021. ISBN 1424409179. 86

NAPOLY, O.; Yong Ho Chin; ZOTTER, B. A generalized method for calculating wake potentials. *Nuclear Inst. and Methods in Physics Research A*, v. 334, n. 2-3, p. 255–265, 1993. ISSN 01689002. 77

NASSIBIAN, G.; SACHERER, F. Methods for Measuring Transverse Coupling Impedances in Circular Accelerators. *Nuclear Instruments and Methods*, v. 159, n. 6, p. 21–27, 1979. 94

NEIL, V. K.; SESSLER, A. M. Longitudinal Resistive Instabilities of Intense Coasting Beams in Particle Accelerators. *The Review of Scientific Instruments*, v. 36, n. 4, p. 429–436, 1965. 72

NEUENSCHWANDER, R. T. *et al.* Engineering Challenges of Future Light Sources. In: *Proceedings of IPAC2015*. Richmond: [s.n.], 2015. p. 1308–1313. ISBN 9783954501687. 29

NG, K.-Y.; BANE, K. L. F. *Explicit Expressions of Impedances and Wake Functions*. Stanford, 2010. 1—-10 p. 68

NIEDERMAYER, U.; GJONAJ, E. Wake Field and Beam Coupling Impedance Simulations. *Beam Dynamics Newsletter*, v. 69, n. December, p. 78–87, 2016. 75

PALUMBO, L.; VACCARO, V. G.; ZOBOV, M. *Wake Fields and Impedance*. Rhodes, 1994. 1–70 p. 67, 69

PELLEGRINI, C. X-ray free-electron lasers: From dreams to reality. *Physica Scripta*, IOP Publishing, T169, p. 014004, 2016. ISSN 02811847. 18

PERSICHELLI, S. *et al.* Impedance and Collective Effects for the Advanced Light Source Upgrade at LBNL. In: *Proceedings of IPAC2017*. Copenhagen: [s.n.], 2017. v. 05-D04, p. 3192–3195. ISBN 9783954501823. 29

PIERCE, J. R. Waves in Electron Streams and Circuits. *Bell System Technical Journal*, v. 30, n. 3, p. 626–651, 1951. 72

PIWINSKI, A. Intra-Beam-Scattering. In: *9th International Conference on High-energy Accelerators*. Stanford: [s.n.], 1974. p. 405–409. 30

PIWINSKI, A. Penetration of the Field of a Bunched Beam Through a Ceramic Vacuum Chamber With Metallic Coating. *IEEE Transactions on Nuclear Science*, NS-24, n. 3, p. 1364–1366, 1977. 73, 97

PIWINSKI, A. *Wake Fields and Ohmic Losses in Flat Vacuum Chambers*. Hamburg, 1992. 1—-18 p. 82

PIWINSKI, A. *The Touschek Effect in Strong Focusing Storage Rings*. [S.l.], 1998. 1–22 p. Disponível em: <http://arxiv.org/abs/physics/9903034>. 30

PODOBEDOV, B.; KRINSKY, S. Transverse Impedance of Tapered Transitions with Elliptical Cross Section. *Physical Review Special Topics - Accelerators and Beams*, v. 10, n. 7, p. 074402, 2007. ISSN 1098-4402. Disponível em: <http://link.aps.org/doi/10.1103/PhysRevSTAB.10.074402>. 71, 100

PODOBEDOV, B.; STUPAKOV, G. Point-Charge Wakefield Calculations from Finite Length Bunch Wake Potentials. *Physical Review Special Topics - Accelerators and Beams*, v. 16, n. 2, p. 024401, 2013. ISSN 1098-4402. Disponível em: <http://link.aps.org/doi/10.1103/PhysRevSTAB.16.024401>. 76

PRODROMIDES, A. *Non-Evaporable Getter Thin Film Coatings for Vacuum Applications.* 180 p. Tese (Tese Doutorado) — Ecole Polytechnique Federale de Lausanne, 2002. 86

RIES, M. *et al.* THz Bursting Thresholds Measured at the Metrology Light Source. In: *Proceedings of IPAC 2012*. New Orleans: [s.n.], 2012. p. 3030–3033. ISBN 9783954501151. Disponível em: <http://accelconf.web.cern.ch/Accelconf/IPAC2012/papers/weppr046.pdf>. 109

ROCHA, T. M. da. *The vacuum system at the upcoming SIRIUS light source in Brazil.* Karlsruhe: [s.n.], 2017. Disponível em: <https://indico.gsi.de/event/5393/session/7/contribution/15/material/slides/0.pdf>. 86

SÁ, F. H. de; LIU, L.; RESENDE, X. R. Optimization of Nonlinear Dynamics for Sirius. In: *Proceedings of IPAC2016*. Busan: [s.n.], 2016. v. 05-D02, p. 3409–3412. ISBN 9783954501472. 33

SÁ, F. H. de *et al.* A New Booster Synchrotron for the Sirius Project. In: *Proceedings of IPAC2014*. Dresden: [s.n.], 2014. v. 02-T12, p. 1959–1962. ISBN 9783954501328. 34

SÁ, F. H. de *et al.* Instability Thresholds and Tune Shift Estimation for Sirius. In: *Proceedings of IPAC 2015*. Richmond: [s.n.], 2015. v. 05-D05, p. 70–73. ISBN 9783954501687. 150

SALVANT, B. *et al.* Quadrupolar Impedance of Simple Models of Kickers. In: *Proceedings of IPAC 2010*. Kyoto: [s.n.], 2010. v. 05-D05, p. 2054—-2057. 95, 97

SANDS, M. *The Physics of Electron Storage Rings - An Introduction.* Stanford, 1970. 172 p. 36, 51

SERAPHIM, R. M. *et al.* Vacuum system design for the sirius storage ring. In: *Proceedings of IPAC 2015*. Richmond: [s.n.], 2015. v. 07-T14, p. 2744–2746. ISBN 9783954501687. 86

SERRET, J.-A. Sur Quelques Formules Relatives à la Théorie des Courbes à Double Courbure. *Journal de mathématiques pures et appliquées 1re séries*, v. 16, p. 193–207, 1851. Disponível em: <http://eudml.org/doc/235002>. 36

SESSLER, A. M.; VACCARO, V. G. *Longitudinal instabilities of azimuthally uniform beams in circular vacuum chambers with walls of arbitrary electrical properties.* Geneva, 1967. 66

SHOBUDA, Y.; CHIN, Y.; TAKATA, K. Coupling impedances of a resistive insert in a vacuum chamber. *Physical Review Special Topics - Accelerators and Beams*, v. 12, n. 9, p. 094401, sep 2009. ISSN 1098-4402. Disponível em: <http://link.aps.org/doi/10.1103/PhysRevSTAB.12.094401>. 99

SHOBUDA, Y.; CHIN, Y. H. Resistive-wall impedances of a thin non-evaporable getter coating on a conductive chamber. *Progress of Theoretical and Experimental Physics*, v. 2017, n. 12, p. 123G01, 2017. ISSN 2050-3911. Disponível em: <http://academic.oup.com/ptep/article/doi/10.1093/ptep/ptx167/4746618>. 90

SHOBUDA, Y.; HIRATA, K. The Existence of a Static Solution for the Haissinski Equation with Purely Inductive Wake Force. *Particle Accelerators*, v. 62, p. 165–177, 1999. 83, 150

SHOBUDA, Y.; YOKOYA, K. Resistive wall impedance and tune shift for a chamber with a finite thickness. *Physical Review E*, v. 66, n. 5, p. 056501, nov 2002. ISSN 1063-651X. Disponível em: <http://link.aps.org/doi/10.1103/PhysRevE.66.056501>. 90

SIEWERT, F. *et al.* On the characterization of ultra-precise x-ray optical components: Advances and challenges in ex situ metrology. *Journal of Synchrotron Radiation*, v. 21, n. 5, p. 968–975, 2014. ISSN 16005775. 29

SIRIUS. *Sirius Web Page*. 2013. Disponível em: <https://wiki-sirius.lnls.br/mediawiki/index.php/Main{_}P>. 32, 33, 34, 99

SOUTOME, K. *et al.* Non-Linear Optimization of Storage Ring Lattice for the SPring-8 Upgrade. In: *Proceedings of IPAC 2016*. Busan: [s.n.], 2016. v. 02-A05, p. 3440–3442. ISBN 9783954501472. 23

STAN, C. A. *et al.* Liquid explosions induced by X-ray laser pulses. *Nature Physics*, v. 12, n. 10, p. 966–971, 2016. ISSN 17452481. 18

STUPAKOV, G. Using the parabolic equation for calculation of beam impedance. *New Journal of Physics*, v. 8, n. 11, p. 280, 2006. ISSN 1367-2630. Disponível em: <http://stacks.iop.org/1367-2630/8/i=11/a=280?key=crossref.760948553bf92eaaf4e439da364a2540>. 68

STUPAKOV, G.; BANE, K. L.; ZAGORODNOV, I. Optical approximation in the theory of geometric impedance. *Physical Review Special Topics - Accelerators and Beams*, v. 10, n. 5, p. 1–11, 2007. ISSN 10984402. 71

STUPAKOV, G. *et al.* Effects of beam-tube roughness on x-ray free electron laser performance. *Physical Review Special Topics - Accelerators and Beams*, v. 2, n. 6, p. 060701, jun 1999. ISSN 1098-4402. Disponível em: <http://link.aps.org/doi/10.1103/PhysRevSTAB.2.060701>. 87

STUPAKOV, G. V. Geometrical wake of a smooth taper. *Particle Accelerators*, v. 56, p. 83–97, 1996. 70

STUPAKOV, G. V. *Wake and Impedance*. Stanford, California, 2000. 55, 57, 61, 76

STUPAKOV, G. V. Low frequency impedance of tapered transitions with arbitrary cross sections. *Physical Review Special Topics - Accelerators and Beams*, v. 10, n. 9, p. 094401, 2007. ISSN 1098-4402. Disponível em: <https://link.aps.org/doi/10.1103/PhysRevSTAB.10.094401>. 70, 101

STUPAKOV, G. V.; BANE, K. L. F.; ZAGORODNOV, I. Impedance Scaling for Small Angle Transitions. *Physical Review Special Topics - Accelerators and Beams*, v. 14, n. 1, p. 014402, 2011. ISSN 10984402. 68

STUPAKOV, G. V.; PODOBEDOV, B. High-frequency impedance of small-angle tapers and collimators. *Physical Review Special Topics - Accelerators and Beams*, v. 13, n. 10, p. 104401, 2010. ISSN 10984402. 71

SUN, Y.; BORLAND, M. Alternate lattice design for advanced photon source multi-bend achromat upgrade. In: *Proceedings of IPAC2015*. Richmond: [s.n.], 2013. p. 1803–1805. ISBN 9783954501687. 23

SUSINI, J. *et al.* New challenges in beamline instrumentation for the esrf upgrade programme phase ii. *Journal of Synchrotron Radiation*, v. 21, n. 5, p. 986–995, 2014. ISSN 16005775. 29

SUZUKI, T. Theory of longitudinal bunched-beam instabilities based on the fokker-planck equation. *Particle Accelerators*, v. 14, p. 91–108, 1983. 50

SUZUKI, T. Fokker-planck theory of transverse mode-coupling instability. *Particle Accelerators*, v. 20, p. 79–96, 1986. 50

TAVARES, D. O. *et al.* Development of an Open-Source Hardware Platform for Sirius Bpm and Orbit Feedback. In: *Proceedings of ICALEPCS 2013*. San Francisco: [s.n.], 2013. p. 1036—-1039. ISBN 9783954501397. Disponível em: <http://accelconf.web.cern.ch/AccelConf/ICALEPCS2013/papers/wecocb07.pdf>. 99

TEMNYKH, A. B. Delta undulator for Cornell energy recovery linac. *Physical Review Special Topics - Accelerators and Beams*, v. 11, n. 12, p. 12072, 2008. ISSN 10984402. 99

THIBAULT, P.; GUIZAR-SICAIROS, M.; MENZEL, A. Coherent imaging at the diffraction limit. *Journal of Synchrotron Radiation*, International Union of Crystallography, v. 21, n. 5, p. 1011–1018, 2014. ISSN 16005775. 28

TSUTSUI, H. *Some Simplified Models of Ferrite Kicker Magnet for Calculation of longitudinal Coupling Impedance*. Geneva, 2000. 1—-19 p. 95, 98

TSUTSUI, H.; VOS, L. *Transverse Coupling Impedance of a Simplified Ferrite Kicker Magnet Model*. Geneva, 2000. 1–6 p. 95

VACCARO, V. G. *Longitudinal Instability of a Coasting Beam above Transition, due to the action of Lumped Discontinuities*. Geneva, 1966. 61

VILELA, L. N. P. *et al.* Studies of Delta-Type Undulators for Sirius. In: *Proceedings of IPAC2017*. Copenhagen: [s.n.], 2017. v. 05-D02, p. 52–54. ISBN 9783954501823. 32, 99

WANG, L. *et al.* Beam Ion Instability: Measurement, Analysis, and Simulation. *Physical Review Special Topics - Accelerators and Beams*, v. 16, n. 10, p. 1–14, 2013. ISSN 10984402. 34, 59

WANG, M. C.; UHLENBECK, G. E. On the Theory of the Brownian Motion. *Reviews of Modern Physics*, v. 17, p. 323–342, 1945. 50

WANG, N. *et al.* Studies on Collective Instabilities in HEPS. In: *Proceedings of IPAC2017*. Copenhagen: [s.n.], 2017. v. 05-D05, p. 3763–3766. ISBN 9783954501823. 29

WANG, N. *et al.* Development of the Impedance Model in HEPS. In: *Proceedings of IPAC2017*. Copenhagen: [s.n.], 2017. v. 05-D04, n. 11205171, p. 3110–3113. ISBN 9783954501823. 29

WARNOCK, R. L. *Shielded Coherent Synchrotron Radiation and its Effect on Very Short Bunches*. [S.l.], 1990. v. 1990, n. November, 1–10 p. Disponível em: <http://inspirehep.net/record/300390/files/slac-pub-5375.pdf>. 107

WARNOCK, R. L.; ELLISON, J. *A General Method for Propagation of the Phase Space Distribution, with Application to the Sawtooth Instability*. Stanford, 2000. 108

WEILAND, T. On the Computation of Resonant Modes in Cylindrically Symmetric Cavities. *Nuclear Instruments and Methods*, v. 216, n. 3, p. 329–348, 1983. 77

WIEDEMANN, H. *Particle Accelerator Physics*. 3rd. ed. Berlin: Springer, 2007. 949 p. ISBN 9783540490432. 36, 39, 42, 50, 51

Wikipedia Contributors. *Airy function — Wikipedia, The Free Encyclopedia*. 2017. 107

Wikipedia Contributors. *Confluent hypergeometric function — Wikipedia, The Free Encyclopedia*. 2017. Disponível em: <https://en.wikipedia.org/w/index.php?title=Confluent{_}hypergeometric{_}function{&}oldid=>. 110

Wikipedia Contributors. *Convolution theorem — Wikipedia, The Free Encyclopedia*. 2017. Disponível em: <https://en.wikipedia.org/w/index.php?title=Convolution{_}theorem{&}oldid=804>. 75

Wikipedia Contributors. *Frenet–Serret formulas — Wikipedia, The Free Encyclopedia*. 2017. Disponível em: <https://en.wikipedia.org/w/index.php?title=Frenet-Serret{_}formulas{&}oldid=814>. 36

Wolfram Research Inc. *Wolfram Mathematica v11.0.1.0*. 2016. 110

YOKOYA, K. *Impedance of Slowly Tapered Structures*. Geneva, 1990. 1—-12 p. 70

YOKOYA, K. Resistive Wall Impedance of Beam Pipes of General Cross Section. *Particle Accelerators*, v. 41, p. 221–248, 1993. 72, 74, 90, 92, 97, 102

ZAGORODNOV, I. Indirect methods for wake potential integration. *Physical Review Special Topics - Accelerators and Beams*, v. 9, n. 10, p. 102002, oct 2006. ISSN 1098-4402. Disponível em: <http://link.aps.org/doi/10.1103/PhysRevSTAB.9.102002>. 77

ZAGORODNOV, I.; BANE, K. L. F.; STUPAKOV, G. V. Calculation of wakefields in 2D rectangular structures. *Physical Review Special Topics - Accelerators and Beams*, v. 18, n. 10, p. 104401, 2015. ISSN 1098-4402. Disponível em: <http://link.aps.org/doi/10.1103/PhysRevSTAB.18.104401>. 58, 77, 100, 103

ZAGORODNOV, I.; SCHUHMANN, R.; WEILAND, T. Long-time numerical computation of electromagnetic fields in the vicinity of a relativistic source. *Journal of Computational Physics*, v. 191, n. 2, p. 525–541, nov 2003. ISSN 00219991. Disponível em: <http://linkinghub.elsevier.com/retrieve/pii/S0021999103003292>. 77

ZAGORODNOV, I.; WEILAND, T. TE/TM field solver for particle beam simulations without numerical Cherenkov radiation. *Physical Review Special Topics - Accelerators and Beams*, v. 8, n. 4, p. 73–87, 2005. ISSN 10984402. 77, 100, 103

ZOTTER, B. *High Frequency Effects on the Transverse Resistive Wall Instability in Particle Storage Rings*. Geneva, 1969. 53 p. 73, 97

ZOTTER, B. *Transverse Oscillations of a Relativistic Particle Beam in a Laminated Vacuum Chamber*. Geneva, 1969. 56 p. 73

ZOTTER, B. Longitudinal instabilities of charged particle beams inside cylindrical walls of finite thickness. *Particle Accelerators*, v. 1, n. 1, p. 311–326, 1970. 73

ZOTTER, B. *New Results on the Impedance of Resistive Metal Walls of Finite Thickness*. Geneva, 2005. 25 p. 74

ZOTTER, B.; KHEIFETS, S. *Impedances And Wakes In High Energy Particle Accelerators And Storage Rings*. 1st. ed. Singapore: World Scientific Publishing Co. Pte. Ltd., 1998. 405 p. ISBN 9789810226268. 61, 66, 67, 91

ZWANZIG, R. *Nonequilibrium Statistical Mechanics*. 1st. ed. New York: Oxford University Press, 2001. 222 p. ISBN 0195140184. 50

Appendix

APPENDIX A – LORENTZ FORCE ULTRA-RELATIVISTIC LIMIT

Intuitively, we tend to think the direct interaction between charged particles, such as electric repulsion, is the responsible for the collective effects observed in storage rings, however, as we will see in the subsequent analysis, this is not the main mechanism for ultra-relativistic particles.

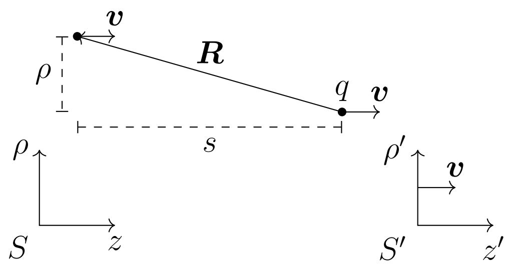

Figure 29 – Duas partículas interagindo via campo direto.

To see this lets consider the interaction of a source particle Q moving with velocity $\vec{\boldsymbol{v}} = v\vec{\hat{\boldsymbol{z}}}$ with a witness particle q moving with the same velocity (parallel path) at a distance s in the direction parallel to the movement and at a transverse distance ρ, as shown in Figure 29. We want to determine the force that the source particle exerts on the witness particle. One way to do this is by calculating the electric field of the source particle in the co-moving frame of reference, S', and Lorentz transforming it back to the laboratory's frame. After the math we obtain:

$$\vec{\boldsymbol{E}} = \frac{q}{4\pi\epsilon_0}\frac{\vec{\boldsymbol{R}}}{\gamma^2 R^{*3}}, \qquad \vec{\boldsymbol{B}} = \frac{1}{c^2}\vec{\boldsymbol{v}} \times \vec{\boldsymbol{E}} \tag{A.1}$$

where $\vec{\boldsymbol{R}}$ is the vector which connects both particles, going from the source to the witness and $R^{*2} = s^2 + x^2/\gamma^2$, e $\gamma = 1/(1 - v^2/c^2)$.

Combining equation A.1 with the Lorentz force, we get the longitudinal and transverse force over the witness particle:

$$F_l = E_z = -\frac{q}{4\pi\epsilon_0}\frac{s}{\gamma^2\left(s^2 + x^2/\gamma^2\right)^{3/2}}, \tag{A.2}$$

$$F_t = E_x - vB_y = -\frac{q}{4\pi\epsilon_0}\frac{x}{\gamma^4\left(s^2 + x^2/\gamma^2\right)^{3/2}} \tag{A.3}$$

In accelerator physics the force $\vec{\boldsymbol{F}}$ is known as space charge force. We can infer from equation A.2 that for any position s and x, the longitudinal force is proportional to

γ^{-2} and $F_t \sim \gamma^{-4}$ if $s \gg x/\gamma$ and $F_t \sim \gamma^{-1}$ if $s \approx 0$. This way, in the ultra-relativistic limit, $\gamma \to \infty$, the electromagnetic interaction between particles moving parallel to each other in free space is zero. It is easy to show that in this limit, if the movement of the particles is not parallel, there is an interaction force only for $s = 0$, but, as their speed is the same, this situation can only happen for an infinitesimal time.

In this work we are interested in the the interaction between particles in the ultra-relativistic limit, $v \to c$. The space charge effects discussed above are despicable in this limit and the interaction between the particles is due to the presence of the walls of the vacuum chamber. Note that taking the limit $v \to c$ in the equation A.1 and remembering that $s = vt - z$, we can write the electromagnetic field of a ultra-relativistic charge as

$$\vec{\boldsymbol{E}} = \frac{q}{2\pi\epsilon_0}\frac{\vec{\hat{\boldsymbol{r}}}}{r}\delta(z - ct), \qquad \vec{\boldsymbol{B}} = \frac{1}{c}\vec{\hat{\boldsymbol{z}}} \times \vec{\boldsymbol{E}}, \tag{A.4}$$

where $\vec{\boldsymbol{r}} = \vec{\hat{\boldsymbol{x}}}\,x + \vec{\hat{\boldsymbol{y}}}\,y$ is a bidimensional vector in cylindrical coordinates ($\vec{\hat{\boldsymbol{x}}}$ and $\vec{\hat{\boldsymbol{y}}}$ are unit vectors in the x e y directions, respectively). The equations above show that the field is pancake-like and follow the beam as it travels through the empty space. It is important to notice that this solution is steady-state, it was necessary an infinite amount of time before t to build it and that's why there is no causal paradoxes in it.

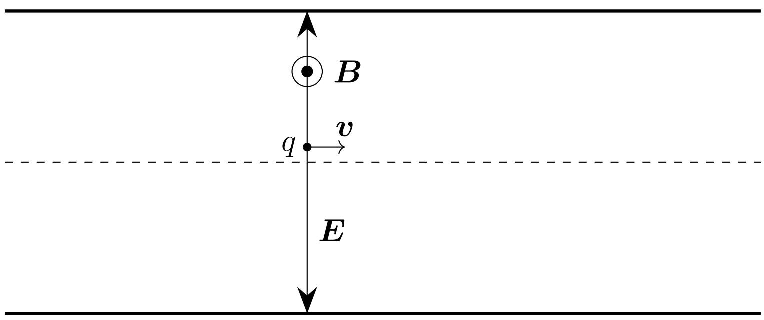

Figure 30 – Particles interacting in a perfectly conducting cylindrical tube.

Lets consider now a pipe with cylindrical symmetry[1], hollow and with absolute vacuum in its interior, made of a perfect electric conductor material and with arbitrary cross section. If we put the particles of the previous example inside this pipe, moving parallel to symmetry axis, they will induce image charges in the surface of the wall which cancel the electromagnetic field inside the metal.

The image charges travel with the same velocity $\vec{\boldsymbol{v}}$ of the particles (see Figure 30). As they move in parallel paths with constant velocity, in the limit $v \to c$, according to the previous results, they do not interact, independently of how close they are from each other.

[1] do not confuse cylindrical symmetry with cylinder. By cylindrical symmetry we mean a system with translational symmetry in one direction.

From this analysis we conclude that the interaction between particles in the ultra-relativistic limit can occur only for two reasons:

- The wall is not perfectly conducting, or
- The pipe does not have cylindrical symmetry (which generally is due to the presence of RF cavities, flanges, bellows, beam position monitors, vacuum pumps, among other elements in the vacuum chamber of an accelerator).

APPENDIX B – DUAS PARTÍCULAS INTERAGINDO NO VÁCUO

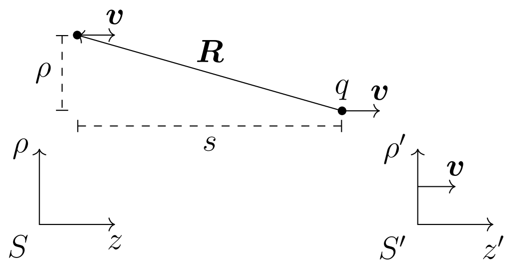

Figure 31 – Duas partículas interagindo via campo direto.

Primeiro, campos gerados por q_1. No referencial S':

$$\overrightarrow{\boldsymbol{E'}} = \frac{q}{4\pi\epsilon_0}\frac{\overrightarrow{\hat{\boldsymbol{r}}'}}{r'^2} \tag{B.1}$$

$$\overrightarrow{\boldsymbol{B'}} = \overrightarrow{\boldsymbol{0}'} \tag{B.2}$$

assumindo que a partícula 1 está na origem do sistema de coordenadas S'.

Lembrando que a transformação entre coordenadas esféricas para cilíndricas são:

$$r' = \sqrt{s'^2 + \rho'^2} \tag{B.3}$$

$$\overrightarrow{\hat{\boldsymbol{r}}'} = \cos\theta' \overrightarrow{\hat{\boldsymbol{z}}'} + \sin\theta' \overrightarrow{\hat{\boldsymbol{\rho}}'} = -\frac{s'}{r'}\overrightarrow{\hat{\boldsymbol{z}}'} + \frac{\rho'}{r'}\overrightarrow{\hat{\boldsymbol{\rho}}'} \tag{B.4}$$

onde a coordenada ϕ fica inalterada.

Assim podemos reescrever o campo elétrico em suas partes longitudinal e transversal:

$$\overrightarrow{\boldsymbol{E'}}_{||} = \frac{q}{4\pi\epsilon_0}\frac{\cos\theta' \overrightarrow{\hat{\boldsymbol{z}}'}}{r'^2} = -\frac{q}{4\pi\epsilon_0}\frac{s' \overrightarrow{\hat{\boldsymbol{z}}'}}{(\rho'^2 + s'^2)^{3/2}} \tag{B.5}$$

$$\overrightarrow{\boldsymbol{E'}}_{\perp} = \frac{q}{4\pi\epsilon_0}\frac{\sin\theta' \overrightarrow{\hat{\boldsymbol{\rho}}'}}{r'^2} = \frac{q}{4\pi\epsilon_0}\frac{x' \overrightarrow{\hat{\boldsymbol{\rho}}'}}{(\rho'^2 + s'^2)^{3/2}} \tag{B.6}$$

Lembrando as equações de transformação de Lorentz para campos elétricos e magnéticos, para esse problema:

$$\overrightarrow{\boldsymbol{E}}_{||} = \overrightarrow{\boldsymbol{E'}}_{||} \tag{B.7}$$

$$\overrightarrow{\boldsymbol{B}}_{||} = \overrightarrow{\boldsymbol{B'}}_{||} \tag{B.8}$$

$$\overrightarrow{\boldsymbol{E}}_{\perp} = \gamma \left(\overrightarrow{\boldsymbol{E'}}_{\perp} - \overrightarrow{\boldsymbol{v}} \times \overrightarrow{\boldsymbol{B'}} \right) \tag{B.9}$$

$$\overrightarrow{\boldsymbol{B}}_{\perp} = \gamma \left(\overrightarrow{\boldsymbol{B'}}_{\perp} + \frac{1}{c^2} \overrightarrow{\boldsymbol{v}} \times \overrightarrow{\boldsymbol{E'}} \right) \tag{B.10}$$

Ainda, as coordenadas espaciais são transformadas da seguinte maneira:

$$\overrightarrow{\hat{\boldsymbol{\rho}}} = \overrightarrow{\hat{\boldsymbol{\rho}}'}, \quad \overrightarrow{\hat{\boldsymbol{z}}} = \overrightarrow{\hat{\boldsymbol{z}}'} \tag{B.11}$$

$$\rho = \rho', \quad z = \frac{z'}{\gamma} \tag{B.12}$$

Assim, podemos notar que:

$$\overrightarrow{\boldsymbol{E}}_{||} = -\frac{q}{4\pi\epsilon_0} \frac{s' \overrightarrow{\hat{\boldsymbol{z}}'}}{(\rho'^2 + s'^2)^{3/2}} = -\frac{q}{4\pi\epsilon_0} \frac{\gamma s \overrightarrow{\hat{\boldsymbol{z}}}}{((\gamma s)^2 + \rho^2)^{3/2}} = -\frac{q}{4\pi\epsilon_0} \frac{s \overrightarrow{\hat{\boldsymbol{z}}}}{\gamma^2 R^{*3}} \tag{B.13}$$

$$\overrightarrow{\boldsymbol{E}}_{\perp} = \frac{q}{4\pi\epsilon_0} \frac{\gamma\rho' \overrightarrow{\hat{\boldsymbol{\rho}}'}}{(\rho'^2 + s'^2)^{3/2}} = \frac{q}{4\pi\epsilon_0} \frac{\gamma\rho \overrightarrow{\hat{\boldsymbol{\rho}}}}{((\gamma s)^2 + \rho^2)^{3/2}} = \frac{q}{4\pi\epsilon_0} \frac{\rho \overrightarrow{\hat{\boldsymbol{\rho}}}}{\gamma^2 R^{*3}} \tag{B.14}$$

$$\overrightarrow{\boldsymbol{B}}_{\perp} = -\frac{\gamma v E'_{\perp}}{c^2} \overrightarrow{\hat{\boldsymbol{\phi}}'} = -\frac{v E_{\perp}}{c^2} \overrightarrow{\hat{\boldsymbol{\phi}}} \tag{B.15}$$

onde $R^* = \sqrt{s^2 + (\rho/\gamma)^2}$

Agora podemos analisar a força exercida pela partícula fonte sobre a partícula teste usando a força de Lorentz

$$\overrightarrow{\boldsymbol{F}} = \left(\overrightarrow{\boldsymbol{E}} + \overrightarrow{\boldsymbol{v}} \times \overrightarrow{\boldsymbol{B}} \right) \tag{B.16}$$

onde foi assumida carga unitária para a partícula teste, e os campos calculados anteriormente.

Assumindo que a velocidade da partícula teste é a mesma da partícula fonte (mesmo módulo e direção), as componentes longitudinal e transversal da força ficam:

$$\overrightarrow{\boldsymbol{F}}_{||} = \overrightarrow{\boldsymbol{E}}_{||} = -\frac{q}{4\pi\epsilon_0} \frac{s \overrightarrow{\hat{\boldsymbol{z}}}}{\gamma^2 R^{*3}} \tag{B.17}$$

$$\overrightarrow{\boldsymbol{F}}_{\perp} = \left(1 + \frac{\overrightarrow{\boldsymbol{v}} \times \overrightarrow{\boldsymbol{v}} \times}{c^2} \right) \overrightarrow{\boldsymbol{E}}_{\perp} = \left(1 - \frac{v^2}{c^2} \right) \overrightarrow{\boldsymbol{E}}_{\perp} = \frac{q}{4\pi\epsilon_0} \frac{\rho \overrightarrow{\hat{\boldsymbol{z}}}}{\gamma^4 R^{*3}} \tag{B.18}$$

onde vemos que a força longitudinal tende a zero proporcionalmente a γ^{-2} quando $v \to c$ e que a força longitudinal tende a zero com γ^{-4}, se $s > \rho/\gamma$ e com γ^{-1} se $s < \rho/\gamma$.

Agora, vamos assumir que a velocidade da partícula teste não é paralela à velocidade da partícula fonte

$$\overrightarrow{\boldsymbol{v_2}} = v(\cos\delta\,\overrightarrow{\hat{\boldsymbol{z}}} + \sin\delta\,\overrightarrow{\hat{\boldsymbol{\rho}}}) \tag{B.19}$$

Assim, a força sofrida por essa partícula fica

$$\begin{aligned}\overrightarrow{\boldsymbol{F}} &= \overrightarrow{\boldsymbol{E}}_{||} + \overrightarrow{\boldsymbol{E}}_{\perp} - v(\cos\delta\,\overrightarrow{\hat{\boldsymbol{z}}} + \sin\delta\,\overrightarrow{\hat{\boldsymbol{\rho}}}) \times \overrightarrow{\hat{\boldsymbol{\phi}}}\frac{vE_\perp}{c^2} \\ &= \left(1 - \frac{v^2}{c^2}\cos\delta\right)\overrightarrow{\boldsymbol{E}}_{\perp} + \overrightarrow{\boldsymbol{E}}_{||} + \frac{v^2}{c^2}E_\perp \sin\delta\,\overrightarrow{\hat{\boldsymbol{z}}}\end{aligned} \tag{B.20}$$

Olhando essa expressão, vemos que, conforme $v \to c$, a força pode ser expressa como:

$$\overrightarrow{\boldsymbol{F}} = \begin{cases} \left((1-\cos\delta)\,\overrightarrow{\hat{\boldsymbol{\rho}}} + \sin\delta\,\overrightarrow{\hat{\boldsymbol{z}}}\right)\dfrac{q}{4\pi\epsilon_0}\dfrac{\gamma\,\overrightarrow{\hat{\boldsymbol{\rho}}}}{\rho^2} & |s| < \rho/\gamma \\ 0 & |s| > \rho/\gamma \end{cases} \tag{B.21}$$

APPENDIX C – CAUSALITY AND CATCH UP DISTANCE

If one particle moves in a straight line at light speed, the electromagnetic field scattered by the discontinuities of the chamber will not catch up with it and will not affect the charges travelling ahead of it. The field will only interact with the charges moving behind of the source particle. Such property is known as causality.

Even though this property is not strictly true in the real world, because particles always travel at speeds lower than the light's, it is true in most practical cases, as we will see bellow.

Lets try to calculate the distance z where the field generated by some discontinuity in the vacuum chamber will catch up with a witness particle at a distance s behind the source particle. At the time $t = 0$ the source particle passes through the discontinuity and an electromagnetic wave is generated with its wave front travelling at the speed of light in all directions, forming a sphere of radius R, see FigureXX. At any given time after this, the following relation holds:

$$ct = R \quad vt = z \qquad \Rightarrow \qquad R = \frac{z}{\beta} \quad \text{where } \beta = \frac{v}{c} \tag{C.1}$$

where z is the distance travelled by the source particle. Besides that, at the specific time when the wake catchs up with the witness particle, the following relation is valid:

$$R^2 = b^2 + (z-s)^2 \Rightarrow z^2(\frac{1}{\beta^2} - 1) + 2sz - (b^2 + s^2) = 0 \Rightarrow \tag{C.2}$$

$$z = -\gamma^2\beta^2 s + \sqrt{s^2\gamma^4\beta^4 + \gamma^2\beta^2\left(b^2 + s^2\right)} = \gamma^2\beta^2 s\left(-1 + \sqrt{1 + \frac{1}{\gamma^2\beta^2}\left(1 + \frac{b^2}{s^2}\right)}\right) \tag{C.3}$$

where b is the distance from the discontinuity to the trajectory of the particles and $\gamma = 1/\sqrt{1-\beta^2}$ is the relativistic energy. FigureXX shows a graphic of this function, normalized by the distance b. We notice that, for $s = 0$, which means the field catching up with the source particle, $z = \gamma\beta b$. For the case of Sirius, $\gamma \approx 5870$ and $\beta \approx 1$, if $b = 2$mm, $z \approx 12$m.

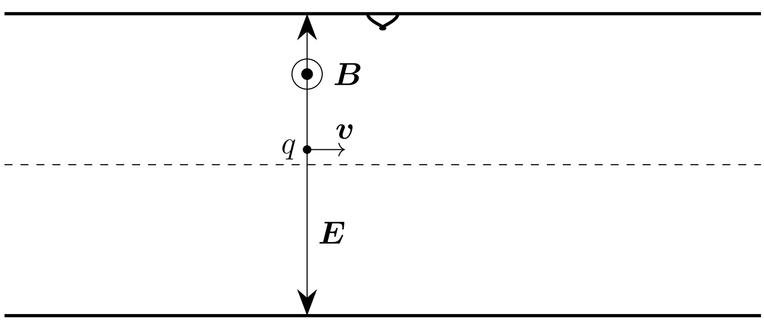

Figure 32 – The catch up distance.

APPENDIX D – CHECK PANOFSKY-WENZEL

As the velocity of the particle is in the longitudinal direction we have

$$\frac{\mathrm{d}a}{\mathrm{d}t} = \frac{\partial a}{\partial t} + v\frac{\partial a}{\partial s} \tag{D.1}$$

where a can be any of the components of vector potential or the scalar potential. This way, since all fields and potentials go to zero in infinity, we always have this equality for the integral of these quantities:

$$\int_{-\infty}^{\infty}\mathrm{d}t\left(\frac{\partial a}{\partial t} + v\frac{\partial a}{\partial s}\right)|_{s=vt-z} = 0. \tag{D.2}$$

Besides, since the integration in time happens with $s = vt - z$, we have

$$\frac{\partial}{\partial z}\left(\int_{-\infty}^{\infty}\mathrm{d}t a\right) = \int_{-\infty}^{\infty}\mathrm{d}t\frac{\partial a}{\partial s}\frac{\partial s}{\partial z} = -\int_{-\infty}^{\infty}\mathrm{d}t\frac{\partial a}{\partial s} \tag{D.3}$$

Also, lets remember the relations between the electromagnetic fields and the potentials:

$$E_x = -\frac{\partial A_x}{\partial t} - \frac{\partial \phi}{\partial x} \qquad B_x = \frac{\partial A_y}{\partial s} - \frac{\partial A_s}{\partial y} \tag{D.4}$$

$$E_y = -\frac{\partial A_y}{\partial t} - \frac{\partial \phi}{\partial y} \qquad B_y = \frac{\partial A_s}{\partial x} - \frac{\partial A_x}{\partial s} \tag{D.5}$$

$$E_s = -\frac{\partial A_s}{\partial t} - \frac{\partial \phi}{\partial s} \qquad B_s = \frac{\partial A_x}{\partial y} - \frac{\partial A_y}{\partial x} \tag{D.6}$$

$$\begin{aligned} w_s = \frac{\partial W}{\partial z} &= \frac{c}{qQ}\frac{\partial}{\partial z}\left(\int_{-\infty}^{\infty}\mathrm{d}t\,(vA_s - \phi)\right) = \frac{c}{qQ}\int_{-\infty}^{\infty}\mathrm{d}t\left(-v\frac{\partial A_s}{\partial s} + \frac{\partial \phi}{\partial s}\right) \\ &= \frac{c}{qQ}\int_{-\infty}^{\infty}\mathrm{d}t\left(\frac{\partial A_s}{\partial t} + \frac{\partial \phi}{\partial s}\right) = -\frac{c}{qQ}\int_{-\infty}^{\infty}\mathrm{d}t E_s \end{aligned} \tag{D.7}$$

$$\begin{aligned} w_x = \frac{\partial W}{\partial x} &= \frac{c}{qQ}\int_{-\infty}^{\infty}\mathrm{d}t\left(v\frac{\partial A_s}{\partial x} - \frac{\partial \phi}{\partial x}\right) \\ &= \frac{c}{qQ}\int_{-\infty}^{\infty}\mathrm{d}t\left(vB_y + v\frac{\partial A_x}{\partial s} + E_x + \frac{\partial A_x}{\partial t}\right) = \frac{c}{qQ}\int_{-\infty}^{\infty}\mathrm{d}t\,(E_x + vB_y) \end{aligned} \tag{D.8}$$

$$\begin{aligned} w_y = \frac{\partial W}{\partial y} &= \frac{c}{qQ}\int_{-\infty}^{\infty}\mathrm{d}t\left(v\frac{\partial A_s}{\partial y} - \frac{\partial \phi}{\partial y}\right) \\ &= \frac{c}{qQ}\int_{-\infty}^{\infty}\mathrm{d}t\left(-vB_x + v\frac{\partial A_y}{\partial s} + E_y + \frac{\partial A_y}{\partial t}\right) = \frac{c}{qQ}\int_{-\infty}^{\infty}\mathrm{d}t\,(E_y + vB_x) \end{aligned} \tag{D.9}$$

APPENDIX E – SYMMETRY ANALYSIS

First lets consider the general expansion of the Wake potential of a bunch in the transverse coordinates of the centroid of the source (x_s, y_s) and the integration path (x, y) up to third order:

$$W(\overrightarrow{\boldsymbol{x}}, s) = W_0(s) + \sum_{i=1}^{4} M_i(s)x_i + \frac{1}{2}\sum_{i,j=1}^{4} D_{ij}(s)x_ix_j + \frac{1}{3}\sum_{i,j,k=1}^{4} Q_{ijk}(s)x_ix_jx_k \tag{E.1}$$

where we considered $\overrightarrow{\boldsymbol{x}} = (x_1, x_2, x_3, x_4) = (x_s, y_s, x, y)$ and because of the commutative property of multiplication, we can set $D_{ij} = D_{ji}$ and $Q_{ijk} = Q_{kij} = Q_{jki} = Q_{ikj} = Q_{jik} = Q_{kji}$ without loss of generality. With these considerations, number of independent components of D is 10 and Q is 20. Besides that, the fact that W is an harmonic function of the transverse coordinates of the integration path, imposes that

$$D_{33} = -D_{44} \tag{E.2}$$

$$Q_{33i} = -Q_{44i}, \quad \text{with} \quad i = 1, 2, 3, 4 \tag{E.3}$$

which leaves only nine independent components of D and sixteen of Q.

Thus, the wake forces become:

$$F_L(\vec{x}, s) = W'(\vec{x}, s) = W_0' + \sum_{i=1}^{4} M_i'x_i + \frac{1}{2}\sum_{i,j=1}^{4} D_{ij}'x_ix_j + \frac{1}{3}\sum_{i,j,k=1}^{4} Q_{ijk}'x_ix_jx_k \tag{E.4}$$

$$F_x(\vec{x}, s) = \frac{\partial W(\overrightarrow{\boldsymbol{x}}, s)}{\partial x} = M_3 + \sum_{i=1}^{4} D_{3i}x_i + \sum_{i,j=1}^{4} Q_{3ij}x_ix_j \tag{E.5}$$

$$F_y(\vec{x}, s) = \frac{\partial W(\overrightarrow{\boldsymbol{x}}, s)}{\partial y} = M_4 + \sum_{i=1}^{4} D_{4i}x_i + \sum_{i,j=1}^{4} Q_{4ij}x_ix_j \tag{E.6}$$

Generally we are interested in obtaining the linear terms as function of the transverse coordinates correct up to second order. It means we want to isolate the linear from the quadract terms in the simulations. Thus, lets keep only the second order terms in the wake forces above.

$$F_L(\overrightarrow{\boldsymbol{x}}, s) = W_0' + \overrightarrow{\boldsymbol{M'}}^T \cdot \overrightarrow{\boldsymbol{x}} + \frac{1}{2}\overrightarrow{\boldsymbol{x}}^T \cdot \overleftrightarrow{\boldsymbol{D'}} \cdot \overrightarrow{\boldsymbol{x}} \tag{E.7}$$

$$F_x(\overrightarrow{\boldsymbol{x}}, s) = M_x + \overrightarrow{\boldsymbol{D_x}}^T \cdot \overrightarrow{\boldsymbol{x}} + \overrightarrow{\boldsymbol{x}}^T \cdot \overleftrightarrow{\boldsymbol{Q_x}} \cdot \overrightarrow{\boldsymbol{x}} \tag{E.8}$$

$$F_y(\overrightarrow{\boldsymbol{x}}, s) = M_y + \overrightarrow{\boldsymbol{D_y}}^T \cdot \overrightarrow{\boldsymbol{x}} + \overrightarrow{\boldsymbol{x}}^T \cdot \overleftrightarrow{\boldsymbol{Q_y}} \cdot \overrightarrow{\boldsymbol{x}} \tag{E.9}$$

where

$$\overrightarrow{\boldsymbol{M}} = \begin{pmatrix} M_1 \\ M_2 \\ M_3 \\ M_4 \end{pmatrix} \tag{E.10}$$

$$\overleftrightarrow{\boldsymbol{D}} = \begin{pmatrix} D_{11} & D_{12} & D_{13} & D_{14} \\ D_{21} & D_{22} & D_{23} & D_{24} \\ D_{31} & D_{32} & D_{33} & D_{34} \\ D_{41} & D_{42} & D_{43} & D_{44} \end{pmatrix} = \begin{pmatrix} D_{11} & D_{12} & D_{13} & D_{14} \\ D_{12} & D_{22} & D_{23} & D_{24} \\ D_{13} & D_{23} & D_{33} & D_{34} \\ D_{14} & D_{24} & D_{34} & -D_{33} \end{pmatrix} \tag{E.11}$$

$$\overrightarrow{\boldsymbol{D_x}} = \overleftrightarrow{\boldsymbol{D}} \cdot \overrightarrow{\hat{\boldsymbol{x}}} \tag{E.12}$$

$$\overrightarrow{\boldsymbol{D_y}} = \overleftrightarrow{\boldsymbol{D}} \cdot \overrightarrow{\hat{\boldsymbol{y}}} \tag{E.13}$$

$$\overleftrightarrow{\boldsymbol{Q_x}} = \begin{pmatrix} Q_{311} & Q_{312} & Q_{313} & Q_{314} \\ Q_{321} & Q_{322} & Q_{323} & Q_{324} \\ Q_{331} & Q_{332} & Q_{333} & Q_{334} \\ Q_{341} & Q_{342} & Q_{343} & Q_{344} \end{pmatrix} = \begin{pmatrix} Q_{113} & Q_{123} & Q_{133} & Q_{134} \\ Q_{123} & Q_{223} & Q_{233} & Q_{234} \\ Q_{133} & Q_{233} & Q_{333} & Q_{334} \\ Q_{134} & Q_{234} & Q_{334} & -Q_{333} \end{pmatrix} \tag{E.14}$$

$$\overleftrightarrow{\boldsymbol{Q_y}} = \begin{pmatrix} Q_{411} & Q_{412} & Q_{413} & Q_{414} \\ Q_{421} & Q_{422} & Q_{423} & Q_{424} \\ Q_{431} & Q_{432} & Q_{433} & Q_{434} \\ Q_{441} & Q_{442} & Q_{443} & Q_{444} \end{pmatrix} = \begin{pmatrix} Q_{114} & Q_{124} & Q_{134} & Q_{133} \\ Q_{124} & Q_{224} & Q_{234} & Q_{233} \\ Q_{134} & Q_{234} & Q_{334} & -Q_{333} \\ Q_{133} & Q_{233} & -Q_{333} & -Q_{334} \end{pmatrix} \tag{E.15}$$

$$\tag{E.16}$$

Due to their importance, some components of the D tensor have a name: the D_{31} and D_{42} are called dipolar wakes; and D_{33} and D_{44} are the quadrupolar wakes. While the first generates coherent tune–shifts and instabilities, the later is the responsible for incoherent tune–shifts of the beam. The other terms are the skew components, which are zero for most practical cases, as we will see below.

When the geometry has symmetry the number of independent componónts in M, D and Q are reduced even more. When the symmetry occurs in one plane, the number of independent components is two, five and eight, respectivelly.Below we list examples for the most practical cases:

- symmetry in the yz plane, or $x = 0$.

$$W(x_s, y_s, x, y, s) = W(-x_s, y_s, -x, y, s) \Rightarrow \tag{E.17}$$

$$M_2 = M_4 = 0 \tag{E.18}$$

$$D_{12} = D_{14} = D_{23} = D_{34} = 0 \tag{E.19}$$

$$Q_{111} = Q_{122} = Q_{113} = Q_{223} = 0 \tag{E.20}$$

$$Q_{133} = Q_{333} = Q_{124} = Q_{234} = 0 \tag{E.21}$$

$$\overrightarrow{\boldsymbol{M}} = \begin{pmatrix} M_1 \\ 0 \\ M_3 \\ 0 \end{pmatrix} \qquad \overleftrightarrow{\boldsymbol{D}} = \begin{pmatrix} D_{11} & 0 & D_{13} & 0 \\ 0 & D_{22} & 0 & D_{24} \\ D_{13} & 0 & D_{33} & 0 \\ 0 & D_{24} & 0 & -D_{33} \end{pmatrix} \tag{E.22}$$

$$\overleftrightarrow{\boldsymbol{Q_x}} = \begin{pmatrix} 0 & Q_{123} & 0 & Q_{134} \\ Q_{123} & 0 & Q_{233} & 0 \\ 0 & Q_{233} & 0 & Q_{334} \\ Q_{134} & 0 & Q_{334} & 0 \end{pmatrix} \quad \overleftrightarrow{\boldsymbol{Q_y}} = \begin{pmatrix} Q_{114} & 0 & Q_{134} & 0 \\ 0 & Q_{224} & 0 & Q_{233} \\ Q_{134} & 0 & Q_{334} & 0 \\ 0 & Q_{233} & 0 & -Q_{334} \end{pmatrix} \tag{E.23}$$

- symmetry in the xz plane, or $y = 0$.

$$W(x_s, y_s, x, y, s) = W(x_s, -y_s, x, -y, s) \Rightarrow \tag{E.24}$$

$$M_1 = M_3 = 0 \tag{E.25}$$

$$D_{12} = D_{14} = D_{23} = D_{34} = 0 \tag{E.26}$$

$$Q_{112} = Q_{222} = Q_{123} = Q_{233} = 0 \tag{E.27}$$

$$Q_{114} = Q_{224} = Q_{134} = Q_{334} = 0 \tag{E.28}$$

$$\overrightarrow{\boldsymbol{M}} = \begin{pmatrix} 0 \\ M_2 \\ 0 \\ M_4 \end{pmatrix} \qquad \overleftrightarrow{\boldsymbol{D}} = \begin{pmatrix} D_{11} & 0 & D_{13} & 0 \\ 0 & D_{22} & 0 & D_{24} \\ D_{13} & 0 & D_{33} & 0 \\ 0 & D_{24} & 0 & -D_{33} \end{pmatrix} \tag{E.29}$$

$$\overleftrightarrow{\boldsymbol{Q_x}} = \begin{pmatrix} Q_{113} & 0 & Q_{133} & 0 \\ 0 & Q_{223} & 0 & Q_{234} \\ Q_{133} & 0 & Q_{333} & 0 \\ 0 & Q_{234} & 0 & -Q_{333} \end{pmatrix} \quad \overleftrightarrow{\boldsymbol{Q_y}} = \begin{pmatrix} 0 & Q_{124} & 0 & Q_{133} \\ Q_{124} & 0 & Q_{234} & 0 \\ 0 & Q_{234} & 0 & -Q_{333} \\ Q_{133} & 0 & -Q_{333} & 0 \end{pmatrix} \tag{E.30}$$

- symmetry in the plane $y = x$.

$$W(x_s, y_s, x, y, s) = W(y_s, x_s, y, x, s) \Rightarrow \tag{E.31}$$

$$M_1 = M_2, \quad M_3 = M_4 \tag{E.32}$$

$$D_{11} = D_{22}, \quad D_{13} = D_{24}, \quad D_{14} = D_{23}, \quad D_{33} = 0 \tag{E.33}$$

$$Q_{111} = Q_{222}, \quad Q_{112} = Q_{122}, \quad Q_{113} = Q_{224}, \quad Q_{114} = Q_{223} \tag{E.34}$$

$$Q_{123} = Q_{124}, \quad Q_{133} = -Q_{233}, \quad Q_{134} = Q_{234}, \quad Q_{333} = -Q_{334} \tag{E.35}$$

$$\overleftrightarrow{\boldsymbol{M}} = \begin{pmatrix} M_1 \\ M_1 \\ M_3 \\ M_3 \end{pmatrix} \qquad \overleftrightarrow{\boldsymbol{D}} = \begin{pmatrix} D_{11} & D_{12} & D_{13} & D_{14} \\ D_{12} & D_{11} & D_{14} & D_{13} \\ D_{13} & D_{14} & 0 & D_{34} \\ D_{14} & D_{13} & D_{34} & 0 \end{pmatrix} \tag{E.36}$$

$$\overleftrightarrow{\boldsymbol{Q_x}} = \begin{pmatrix} Q_{113} & Q_{123} & Q_{133} & Q_{134} \\ Q_{123} & Q_{114} & -Q_{133} & Q_{134} \\ Q_{133} & -Q_{133} & Q_{333} & -Q_{333} \\ Q_{134} & Q_{134} & -Q_{333} & -Q_{333} \end{pmatrix} \quad \overleftrightarrow{\boldsymbol{Q_y}} = \begin{pmatrix} Q_{114} & Q_{123} & Q_{134} & Q_{133} \\ Q_{123} & Q_{113} & Q_{134} & -Q_{133} \\ Q_{134} & Q_{134} & -Q_{333} & -Q_{333} \\ Q_{133} & -Q_{133} & -Q_{333} & Q_{333} \end{pmatrix} \tag{E.37}$$

- symmetry in the plane $y = -x$.

$$W(x_s, y_s, x, y, s) = W(-y_s, -x_s, -y, -x, s) \Rightarrow \tag{E.38}$$

$$M_1 = -M_2, \quad M_3 = -M_4 \tag{E.39}$$

$$D_{11} = D_{22}, \quad D_{13} = D_{24}, \quad D_{14} = D_{23}, \quad D_{33} = 0 \tag{E.40}$$

$$Q_{111} = -Q_{222}, \quad Q_{112} = -Q_{122}, \quad Q_{113} = -Q_{224}, \quad Q_{114} = -Q_{223} \tag{E.41}$$

$$Q_{123} = -Q_{124}, \quad Q_{133} = Q_{233}, \quad Q_{134} = -Q_{234}, \quad Q_{333} = Q_{334} \tag{E.42}$$

$$\overleftrightarrow{\boldsymbol{M}} = \begin{pmatrix} M_1 \\ -M_1 \\ M_3 \\ -M_3 \end{pmatrix} \qquad \overleftrightarrow{\boldsymbol{D}} = \begin{pmatrix} D_{11} & D_{12} & D_{13} & D_{14} \\ D_{12} & D_{11} & D_{14} & D_{13} \\ D_{13} & D_{14} & 0 & D_{34} \\ D_{14} & D_{13} & D_{34} & 0 \end{pmatrix} \tag{E.43}$$

$$\overleftrightarrow{\boldsymbol{Q_x}} = \begin{pmatrix} Q_{113} & Q_{123} & Q_{133} & Q_{134} \\ Q_{123} & -Q_{114} & Q_{133} & -Q_{134} \\ Q_{133} & Q_{133} & Q_{333} & Q_{333} \\ Q_{134} & -Q_{134} & Q_{333} & -Q_{333} \end{pmatrix} \quad \overleftrightarrow{\boldsymbol{Q_y}} = \begin{pmatrix} Q_{114} & -Q_{123} & Q_{134} & Q_{133} \\ -Q_{123} & -Q_{113} & -Q_{134} & Q_{133} \\ Q_{134} & -Q_{134} & Q_{333} & -Q_{333} \\ Q_{133} & Q_{133} & -Q_{333} & -Q_{333} \end{pmatrix} \tag{E.44}$$

Below we combine some of the above mentioned symmetries which are very common in the simulations performed for accelerators elements:

- x=0 and y=0.

$$\overrightarrow{\boldsymbol{M}} = \overrightarrow{\boldsymbol{0}} \qquad \overleftrightarrow{\boldsymbol{D}} = \begin{pmatrix} D_{11} & 0 & D_{13} & 0 \\ 0 & D_{22} & 0 & D_{24} \\ D_{13} & 0 & D_{33} & 0 \\ 0 & D_{24} & 0 & -D_{33} \end{pmatrix} \qquad \overleftrightarrow{\boldsymbol{Q_x}} = \overleftrightarrow{\boldsymbol{0}} \qquad \overleftrightarrow{\boldsymbol{Q_y}} = \overleftrightarrow{\boldsymbol{0}} \tag{E.45}$$

- $y = -x$ and $y = x$.

$$\overrightarrow{\boldsymbol{M}} = \overrightarrow{\mathbf{0}} \qquad \overleftrightarrow{\boldsymbol{D}} = \begin{pmatrix} D_{11} & D_{12} & D_{13} & D_{14} \\ D_{12} & D_{11} & D_{14} & D_{13} \\ D_{13} & D_{14} & 0 & D_{34} \\ D_{14} & D_{13} & D_{34} & 0 \end{pmatrix} \qquad \overleftrightarrow{\boldsymbol{Q}_x} = \overleftrightarrow{\mathbf{0}} \qquad \overleftrightarrow{\boldsymbol{Q}_y} = \overleftrightarrow{\mathbf{0}} \tag{E.46}$$

- $x = 0$, $y = 0$, $y = -x$ and $y = x$.

$$\overrightarrow{\boldsymbol{M}} = \overrightarrow{\mathbf{0}} \qquad \overleftrightarrow{\boldsymbol{D}} = \begin{pmatrix} D_{11} & 0 & D_{13} & 0 \\ 0 & D_{11} & 0 & D_{13} \\ D_{13} & 0 & 0 & 0 \\ 0 & D_{13} & 0 & 0 \end{pmatrix} \qquad \overleftrightarrow{\boldsymbol{Q}_x} = \overleftrightarrow{\mathbf{0}} \qquad \overleftrightarrow{\boldsymbol{Q}_y} = \overleftrightarrow{\mathbf{0}} \tag{E.47}$$

where we notice that when there is at least 2 planes of symmetry, all the odd order terms are zero.

APPENDIX F – WAKE CALCULATION FROM GDFIDL SIMULATIONS

One simulation in GDFIDL consists of passing a linear gaussian bunch with the velocity of light in the longitudinal direction and with a specific transverse position, say $(x_s, y_s) = (d_x, d_y)$ through the simulated structure solving Maxwell equations in time. While doing this, the code saves in memory the wake potential $W(d_x, d_y, x, y, s)$ for all transverse positions (x, y) of integration and all s. This procedure is very time consuming and we gerally try to perform the mininum amount of simulations possible to get the results we need.

Lets suppose a simulation was performed with the position of the source in $(x_s, y_s) = (d, 0)$. If we calculate the Horizontal Wake potential in a path where $y = 0$ then, up to second order in the transverse coordinates we can write:

$$F_L(d,0,x,0) = W_0 + M_1 d + M_3 x + D_{11} d^2 + D_{13} dx + D_{33} x^2 \tag{F.1}$$

$$F_x(d,0,x,0) = M_x + D_{x3} x + D_{x1} d + Q_{x33} x^2 + Q_{x11} d^2 + Q_{x13} xd \tag{F.2}$$

$$F_y(d,0,x,0) = M_y + D_{y3} x + D_{y1} d + Q_{y33} x^2 + Q_{y11} d^2 + Q_{y13} xd \tag{F.3}$$

Now, integrating the total wake in 4 different x points we get:

$$F_1 = F_x(d, x_1) = M_x + D_{x3} x_1 + D_{x1} d + Q_{x33} x_1^2 + Q_{x11} d^2 + Q_{x13} x_1 d \tag{F.4}$$

$$F_2 = F_x(d, x_2) = M_x + D_{x3} x_2 + D_{x1} d + Q_{x33} x_2^2 + Q_{x11} d^2 + Q_{x13} x_2 d \tag{F.5}$$

$$F_3 = F_x(d, x_3) = M_x + D_{x3} x_3 + D_{x1} d + Q_{x33} x_3^2 + Q_{x11} d^2 + Q_{x13} x_3 d \tag{F.6}$$

$$F_4 = F_x(d, x_4) = M_x + D_{x3} x_4 + D_{x1} d + Q_{x33} x_4^2 + Q_{x11} d^2 + Q_{x13} x_4 d \tag{F.7}$$

To extract the component D_x from the total wake we do:

$$\Delta_1 = \frac{F_1}{x_1} - \frac{F_2}{x_2} = \left(M_x + D_{x1} d + Q_{x11} d^2\right)\left(\frac{1}{x_1} - \frac{1}{x_2}\right) + Q_{x33}(x_1 - x_2) \tag{F.8}$$

$$\Delta_2 = \frac{F_3}{x_3} - \frac{F_4}{x_4} = \left(M_x + D_{x1} d + Q_{x11} d^2\right)\left(\frac{1}{x_3} - \frac{1}{x_4}\right) + Q_{x33}(x_3 - x_4) \tag{F.9}$$

then, remembering $(1/a - 1/b)/(a - b) = -1/ab$ we get:

$$\frac{\Delta_1}{x_1 - x_2} - \frac{\Delta_2}{x_3 - x_4} = \left(M_x + D_{x1} d + Q_{x11} d^2\right)\left(\frac{1}{x_3 x_4} - \frac{1}{x_1 x_2}\right) \tag{F.10}$$

$$M_x + D_{x1} d + Q_{x11} d^2 = \left(\frac{x_1 x_2 x_3 x_4}{x_3 x_4 - x_1 x_2}\right)\left(\frac{\Delta_1}{x_1 - x_2} - \frac{\Delta_2}{x_3 - x_4}\right) \tag{F.11}$$

Note that in general to isolate the dipolar component D_x, it is necessary to perform another two simulations. If another simulation is performed with the source at $(x_s, y_s) = (-d, 0)$ it is also possible to isolate the dipolar component.

Now, lets try to extract the quadrupolar component

$$\Delta_1 = \frac{F_1 - F_2}{x_1 - x_2} = D_{x3} + Q_{x13}d + Q_{x33}(x_1 + x_2) \tag{F.12}$$

Notice that, if we choose $x_2 = -x_1$ the contribution from Q_{x33} is canceled and

$$D_{x3} + Q_{x13}d = \Delta_1 \tag{F.13}$$

where it is clear that is necessary other simulation to extract the quadrupolar wake.

APPENDIX G – CÁLCULO DOS WAKE-POTENTIAL A PARTIR DO ECHOZR

De acordo com a referência, temos que:

$$W_{||}(x_0, y_0, x, y, s) = \frac{1}{w}\sum_{m=1}^{\infty} W_m(y_0, y, s)\sin(k_{x,m}x_0)\sin(k_{x,m}x), \tag{G.1}$$

$$W_y(x_0, y_0, x, y, s) = \frac{1}{w}\sum_{m=1}^{\infty} k_{x,m}W_{y,m}(y_0, y, s)\sin(k_{x,m}x_0)\sin(k_{x,m}x), \tag{G.2}$$

$$W_x(x_0, y_0, x, y, s) = \frac{1}{w}\sum_{m=1}^{\infty} k_{x,m}W_{x,m}(y_0, y, s)\sin(k_{x,m}x_0)\cos(k_{x,m}x), \tag{G.3}$$

where w is the half-width of the structure, $0 < x < 2w$ is the horizontal position of the trailing particle, $0 < x_0 < 2w$ is the horizontal position of the source particle, y is vertical position of the trailing particle, y_0 is vertical position of the source particle, $s = z - ct$ is the position of the trailing particle relative to the source particle and

$$k_{x,m} = \frac{\pi}{2w}m \tag{G.4}$$

The other terms are given by

$$\begin{aligned} W_m(y_0, y, s) =& W_m^{cc}(s)\cosh(k_{x,m}y_0)\cosh(k_{x,m}y) + \\ & W_m^{ss}(s)\sinh(k_{x,m}y_0)\sinh(k_{x,m}y), \end{aligned} \tag{G.5}$$

$$\begin{aligned} W_{y,m}(y_0, y, s) =& S_m^{cc}(s)\cosh(k_{x,m}y_0)\sinh(k_{x,m}y) + \\ & S_m^{ss}(s)\sinh(k_{x,m}y_0)\cosh(k_{x,m}y), \end{aligned} \tag{G.6}$$

$$\begin{aligned} W_{x,m}(y_0, y, s) =& S_m^{cc}(s)\cosh(k_{x,m}y_0)\cosh(k_{x,m}y) + \\ & S_m^{ss}(s)\sinh(k_{x,m}y_0)\sinh(k_{x,m}y), \end{aligned} \tag{G.7}$$

where

$$S_m^{cc} = \int_{-\infty}^{s} W_m^{cc}(s')\mathrm{d}s', \qquad S_m^{ss} = \int_{-\infty}^{s} W_m^{ss}(s')\mathrm{d}s' \tag{G.8}$$

and the quantities $W_m^{cc}(s')$ and $W_m^{ss}(s')$ are related to the output of the softwares ECHOzR and ECHO2D by:

$$W_m^{cc}(s') = \frac{W_m^M(y_0, y, s)}{\cosh(k_{x,m}y_0)\cosh(k_{x,m}y)} \tag{G.9}$$

$$W_m^{ss}(s') = \frac{W_m^E(y_0, y, s)}{\sinh(k_{x,m}y_0)\sinh(k_{x,m}y)} \tag{G.10}$$

where $W_m^M(y_0, y, s)$ and $W_m^M(y_0, y, s)$ are the results of the simulation with magnetic and electric boundary conditions, respectively.

Our objective is to obtain the formulas for the monopole longitudinal, dipole and quarupolar transverse wake functions at the point $\vec{v} = (x_0 = w, y_0 = 0, x = w, y = 0)$ from these results. The monopolar wakes are readly obtained:

$$W_m(0,0,s) = W_m^{cc}(s) \Rightarrow W_{||}(\vec{v}) = \frac{1}{w}\sum_{m=1,\mathrm{odd}}^{\infty} W_m^{cc}(s), \tag{G.11}$$

$$W_{y,m}(0,0,s) = 0 \Rightarrow W_y(\vec{v}) = 0, \tag{G.12}$$

$$W_{x,m}(0,0,s) = S_m^{cc}(s) \Rightarrow W_x(\vec{v}) = \frac{1}{w}\sum_{m=1}^{\infty} S_m^{cc}(s)\frac{\sin(m\pi)}{2} = 0 \tag{G.13}$$

To calculate the dipolar and quadrupolar wakes, we need to take the first derivative of the transverse wakes at the point of interest, $\vec{v}$. It is easy to see that the first derivatives of the longitudinal wake are zero. For the transverse:

$$W_{y,d}(s) = \frac{\mathrm{d}}{\mathrm{d}y_0}W_y\bigg|_{\vec{v}} = \frac{1}{w}\sum_{m=1,\mathrm{odd}}^{\infty} k_{x,m}^2 S_m^{ss}(s) = \frac{1}{w}\int_{-\infty}^{s}\sum_{m=1,\mathrm{odd}}^{\infty} k_{x,m}^2 W_m^{ss}(s')\mathrm{d}s', \tag{G.14}$$

$$W_{y,q}(s) = \frac{\mathrm{d}}{\mathrm{d}y}W_y\bigg|_{\vec{v}} = \frac{1}{w}\sum_{m=1,\mathrm{odd}}^{\infty} k_{x,m}^2 S_m^{cc}(s) = \frac{1}{w}\int_{-\infty}^{s}\sum_{m=1,\mathrm{odd}}^{\infty} k_{x,m}^2 W_m^{cc}(s')\mathrm{d}s', \tag{G.15}$$

$$W_{x,d}(s) = \frac{\mathrm{d}}{\mathrm{d}x_0}W_x\bigg|_{\vec{v}} = \frac{1}{w}\sum_{m=1,\mathrm{even}}^{\infty} k_{x,m}^2 S_m^{cc}(s) = \frac{1}{w}\int_{-\infty}^{s}\sum_{m=1,\mathrm{even}}^{\infty} k_{x,m}^2 W_m^{cc}(s')\mathrm{d}s', \tag{G.16}$$

$$W_{x,q}(s) = \frac{\mathrm{d}}{\mathrm{d}x}W_x\bigg|_{\vec{v}} = -\frac{1}{w}\sum_{m=1,\mathrm{odd}}^{\infty} k_{x,m}^2 S_m^{cc}(s) = -\frac{1}{w}\int_{-\infty}^{s}\sum_{m=1,\mathrm{odd}}^{\infty} k_{x,m}^2 W_m^{cc}(s')\mathrm{d}s' \tag{G.17}$$

and all the skew terms are zero.

APPENDIX H – PASSIVE LANDAU CAVITY SIMULATION

Assuming the wake function of the main mode of the Landau cavity can be modeled by the longitudinal resonator impedance with parameters ω_R, R and Q:

$$W_0'(z) = 2\alpha R e^{-\alpha z/c}\left(\cos\left(\frac{\bar{\omega}_R z}{c}\right) - \frac{\alpha}{\bar{\omega}_R}\sin\left(\frac{\bar{\omega}_R z}{c}\right)\right) \tag{H.1}$$

where $\alpha = \omega_R/2Q$, $\bar{\omega}_R = \sqrt{\omega_R^2 - \alpha^2}$, then, the equilibrium normalized potential in the cavity is given by:

$$V_n(z) = \frac{eC_0}{cE_0} 2\alpha R\left(\Re\left\{\hat{V}_n(z)\right\} + \frac{\alpha}{\bar{\omega}_R}\Im\left\{\hat{V}_n(z)\right\}\right) \tag{H.2}$$

where C_0 is the ring circumference, e is the electron charge, E_0 is the average energy of the storage ring and c is the speed of light in vacuum. The subscript n indicates we want to know the potential in the n-th bunch. The term $\hat{V}_n(z)$ is the infinite sum of the potentials deposited by each bunch in the structure in previous turns:

$$\hat{V}_n(z) = \sum_{l\in\mathscr{B}}\sum_{k=a_l}^{\infty} I_l e^{-\beta(s_l(k)-s_n(0)-z)} = e^{\beta z}\sum_{l\in\mathscr{B}} I_l e^{\beta(n-l)\frac{C_0}{h}} \overbrace{\sum_{k=a_l}^{\infty} e^{-\beta k C_0}}^{A_l} \tag{H.3}$$

where $\beta = (\alpha + i\hat{\omega}_R)/c$, I_l is the current of the l-th bunch, h is the harmonic number, $s_l(k)$ indicates the synchrotron position of the l-th bunch k turns behind the current one, $\mathscr{B}$ is the set of all the bunch numbers that are filled and

$$a_l = \begin{cases} 0 & l > n \\ 1 & l \leq n \end{cases} \tag{H.4}$$

to take into account that bunches ahead of the n-th bunch do not contribute to the potential felt by it in the current turn. In the second equality it was used the following identity

$$s_l(k) - s_n(0) - z = (s_l(0) - s_l(k)) - (s_n(0) - s_l(0)) - z = kC_0 - (n-l)\frac{C_0}{h} - z. \tag{H.5}$$

the sum A_l is an infinite geometric series with ratio $e^{-\beta C_0}$ and can be carried out analytically:

$$A_l = \begin{cases} \dfrac{1}{1-e^{-\beta C_0}} & l > n \\ \dfrac{e^{-\beta C_0}}{1-e^{-\beta C_0}} + 1/2 & l = n \\ \dfrac{e^{-\beta C_0}}{1-e^{-\beta C_0}} & l < n \end{cases} \tag{H.6}$$

where the 1/2 in the $l = n$ case is needed to take into account the fundamental theorem of beam loading. This way, we can write

$$\hat{V}_n(z) = e^{\beta z} \sum_{l \in \mathscr{B}} A_l I_l e^{\beta(n-l)\frac{C_0}{h}}. \tag{H.7}$$

The result above can be generalized to distributions $\lambda_l(z)$ different than the point charge, $\delta(z)$. Starting from equation (3.31a) and assuming the wake function is given by equation (H.1), we get an equation similar to (H.2), with $\hat{V}_n(z)$ given by

$$\hat{V}_n(z) = e^{\beta z} \sum_{l \in \mathscr{B}} A_l I_l e^{\beta(n-l)\frac{C_0}{h}} \overbrace{\int_{-\infty}^{\infty} \mathrm{d}z' \lambda_l(z') e^{-\beta z'}}^{B_l} \tag{H.8}$$

where the integral B_l can be carried out assuming the damping factor, α, is small, in such a way that the distribution λ_l goes to zero in an interval much smaller than the scale where the factor $e^{-\alpha z'/c}$ have any influence:

$$B_l = \int_{-\infty}^{\infty} \mathrm{d}z' \lambda_l(z') e^{-\beta z'} \overset{\alpha z_0/c \ll 1}{\approx} \int_{-\infty}^{\infty} \mathrm{d}z' \lambda_l(z') e^{-i\bar{\omega}_R z'} = \tilde{\lambda}_l^*(\bar{\omega}_R) \tag{H.9}$$

where z_0 is any characterist length of the distribution λ_l. Finally, we can write:

$$\hat{V}_n(z) = e^{\beta z} \sum_{l \in \mathscr{B}} A_l I_l \tilde{\lambda}_l^*(\bar{\omega}_R) e^{\beta(n-l)\frac{C_0}{h}}. \tag{H.10}$$

Notice that both expressions, (H.7)

APPENDIX I – LONGITUDINAL INSTABILITY ANALYSIS

I.1 Introduction

In this work the longitudinal tracking results for Sirius with the total impedance budget will be presented. In Sec. I.2 the methods used in the Haissinski solver and in the tracking code are briefly described, in Sec. I.3 the construction of an impedance model for the longitudinal plane based only on resonators is treated and in Sec. I.4 noise issues with the first simulations are discussed, where a simple theory to explain its mechanism is introduced.

I.2 Description of the Methods

I.2.1 Haissinski Solver

The Haissinski equation can be written in the following form, $\rho(z) = \mathcal{H}(\rho, z)$, where

$$\mathcal{H}(\rho, z) = B \exp\left(\frac{q}{\alpha L_0 E_0 \sigma_\delta^2}\left(U_{\text{cav}}(z) - I_b T_0 \int_{-\infty}^{\infty} \mathrm{d}z' W_0'(z-z')\rho(z')\right)\right),$$
$$\text{with } B \in \mathbb{R} \left| \int_{-\infty}^{\infty} \mathrm{d}z \mathcal{H}(\rho, z) = 1 \right. , \tag{I.1}$$

q is the electron charge, I_b is the bunch current and W_0' is the total longitudinal wake function.

To solve this equation an iterative approach was adopted. Starting from a very low I_b and an initial guess

$$\rho_0^{I_b}(z) = A \exp\left(\frac{qU_{\text{cav}}(z)}{\alpha} L_0 E_0 \sigma_\delta^2\right), \text{ with } A \in \mathbb{R} \left| \int_{-\infty}^{\infty} \mathrm{d}z \rho_0^{I_b}(z) = 1 \right. \tag{I.2}$$

we iterate

$$\rho_n^{I_b}(z) = \begin{cases} \mathcal{H}(\rho_0^{I_b}, z) & \text{if } n = 1 \\ \mathcal{H}\left(\frac{\rho_{n-1}^{I_b} + \beta\rho_{n-2}^{I_b}}{1+\beta}, z\right) & \text{if } n > 1 \end{cases}, \tag{I.3}$$

where β is a positive convergence control variable. For each iteration the difference

$$d_n^{I_b} = \int_{-\infty}^{\infty} \mathrm{d}z \left(\rho_n^{I_b} - \rho_{n-1}^{I_b}\right)^2 \tag{I.4}$$

is calculated and compared to a threshold, ϵ. When $d_{n_c}^{I_b} < \epsilon$, convergence is assumed and we set $\rho^{I_b} = \rho_{n_c}^{I_b}$. Then, the current is incremented by a small value $I_b + \Delta I$, with $\Delta I \ll I_b$, and the process is repeated with the initial guess $\rho_0^{I_b+\Delta I} = \rho^{I_b}$. Note that this method does not require the wakes to respect causality and can also be applied to non-parabolic RF cavity potentials.

This implementation was benchmarked with the results presented by Bane & Ruth (1989) for the inductive and resistive impedances[1]. For the capacitive (positive inductance) the code fails to converge when the strength of the perturbation gets close to the well known singularity point of such impedance, as explained by Shobuda & Hirata (1999). However this was not a problem for all the practical cases studied here.

I.2.2 Tracking Code

The structure of the tracking code used is very similar to the one described in Ref. Sá *et al.* (2015), with the additional feature of including damping and quantum excitation terms for the single particle dynamics. Wake field kicks can be included in two different ways:

General Wakes: In this case the wakes do not need to respect the causality condition and are passed to the code as interpolation tables. The code uses the Particle In Cell (PIC) approach, where the total simulation length of the longitudinal direction, L_c, is segmented in N_c intervals and the approximate beam distribution is calculated from the number of macroparticles in each cell. Then, the convolution theorem is used to calculate the kick curve(BASSI *et al.*, 2015), which is interpolated according to each particle's position;

Resonators: The parameters of the resonators, (R_s, ω_r, Q), are used as input. The code does not use the PIC approach, each of the N_p macroparticles being simulated interact with each other and the wake is calculated through the sum of the potentials left by each particle in each resonator.

Note that in the second method N_p is the only variable to be tested for the analysis of the convergence of the results, while for the first method the additional variable N_c is also important. This inconvenience can be avoided if the number of slices is set in such a way that the grid length satifies the Nyquist theorem for the highest relevant frequency of the impedance used in tracking,

$$\Delta z_c = L_c/N_c > \frac{2}{f_{\max}}. \tag{I.5}$$

[1] Since the code cannot handle wake functions that are given by distributions, such as the $\delta'(z)$ and the $\delta(z)$ of the inductive and resistive wakes, respectively, the functions used for the simulation in these cases were their convolution with a very small ($\sigma_z = 20\mu$m) gaussian bunch.

Table 7 – Broad band resonators model of the Sirius longitudinal impedance budget.

f_R [GHz]	716.2	206.9	138.4	79.6	57.3	35.0	17.5	17.8	11.9	9.2
R_s [kΩ]	30.0	6.5	2.0	2.0	2.5	2.5	1.7	3.0	4.0	20.0
Q	0.7	1.3	4.0	1.0	4.5	3.0	1.0	24.0	24.0	100.0

This code was benchmarked with SPACE(BASSI *et al.*, 2015) and Elegant(BORLAND, 2000).

I.3 Impedance Model

Table 7 shows the broad band resonators (BBR) model of the Sirius longitudinal impedance budget. The very high frequency BBR, the first in the table, is due to the NEG coated vacuum chamber, which has a very large inductive impedance at low frequencies, being the major contributor for the bunch lengthening. Besides, note that the last three resonators have a fairly large Q factor. They are originated by the bellows and the BPMs of the machine, and, as explained below, are important to explain the behavior of the beam above the threshold of the microwave instability.

This impedance budget was built by fitting the total impedance and refined based on comparisons of the instabilities thresholds predicted by them in frequency domain, on the bunch-lengthening and synchrotron phase shift as function of the bunch current and also on the behavior of the distribution above the threshold, calculated by tracking. In this process it was noted that including only the first seven BBR is enough to explain the bunch-lengthening effects and the threshold for the microwave instability, but only with all the ten resonators it is possible to reproduce the behavior above the threshold, as shown in Fig. 33 and Fig. 34.

I.4 Noise in tracking simulations

In order to simulate correctly the high frequency BBR of the impedance model, fulfilling the condition imposed by the Nyquist theorem expressed in Eq. (I.5), it was necessary to set $\Delta z_c = 2\mu\text{m}$. Figure 35 shows the results of tracking with the impedance budget of the Sirius storage ring for different numbers of macroparticles in comparison with the behavior predicted by the Haissinski solver and Fig. 36 shows the integrated power spectrum of the kick received by an arbitrary particle in the bunch. Note that even with a number of particles as high as 1 M particles, there is still a strong influence of noise, and only with 10 M particles the results seem to have converged, where the onset of an instability is noted at approximately 3 mA. Such results motivated us to try to understand the mechanism that drives this behavior.

Given a longitudinal density distribution $\rho(z)$, the number of particles in a small interval Δz centered at the position z, $N_l(z)$, is a random variable that follows a binomial distribution. Thus, considering that there are N_p particles in the bunch, we have

$$\langle N_l \rangle = \rho(z)\Delta z N_p \quad \text{and} \quad \mathrm{var}\,(N_l) \approx \rho(z)\Delta z N_p, \tag{I.6}$$

where $\langle \cdot \rangle$ and $\mathrm{var}\,(\cdot)$ denotes average and variance, respectively, being the latter a measure of the fluctuations in the bunch due to the finite number of particles. If the particles were static, this fluctuation would also be, but, as they are moving due to the longitudinal dynamics of the storage ring, these fluctuations are constantly changing. For very small Δz, the value of $N_l(z)$ changes very fast, but as Δz increases, this characteristic time becomes increasinly large.

It is possible to estimate the length scale where the behavior of the variance changes by considering the number of turns it takes for the stored particles to complete one oscillation in the longitudinal phase space, which is $1/\nu_z$. This means that, on average, the longitudinal position of each particle differs from its position in the last turn by

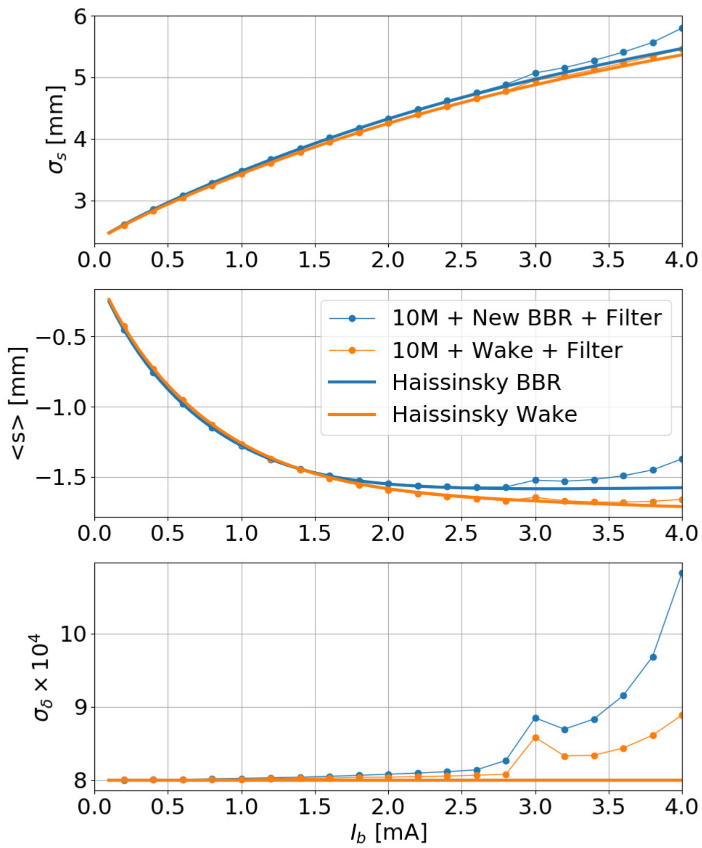

Figure 33 – Bunch length, synchrotron phase shift, and energy spread as function of the single bunch current for the BBR model and the real wake of the machine, calculated by tracking and using the Haissinski solver. Note that both impedance models agree very well and predict the threshold of the microwave instability at ≈ 2.7mA.

$\Delta z_L \approx 4\nu_z\sigma_z$. Consequently, for scales below or on the order of this length, the fluctuations of the particle distribution changes in a turn by turn basis.

Now, lets consider there is a wake function $W(z)$ that is constant in a small interval $\Delta z_W \approx \Delta z_L$ behind the source particle and zero outside this interval. Then, any particle inside the bunch would receive random kicks $K = eI_bT_0WN_l/N_p$. The average of this kick varies slowly in time, because it depends on the evolution of the density distribution, but the variance, given by

$$\mathrm{var}\,(K) = (qI_bT_0W)^2\,\frac{\mathrm{var}\,(N_l)}{N_p^2} \approx (qI_bT_0W)^2\,\frac{\Delta z_W}{\sqrt{2\pi e}N_p}, \tag{I.7}$$

varies from turn to turn, where in the last step it was assumed $z \approx \sigma_z$ and that the distribution is gaussian, $\rho(\sigma_z) = 1/\sqrt{2\pi e}\sigma_z$. Summarizing, this mechanism introduce a random variation of the energy of the particles in a turn by turn basis, similarly to the quantum excitation process due to radiation emission. This means that it should change

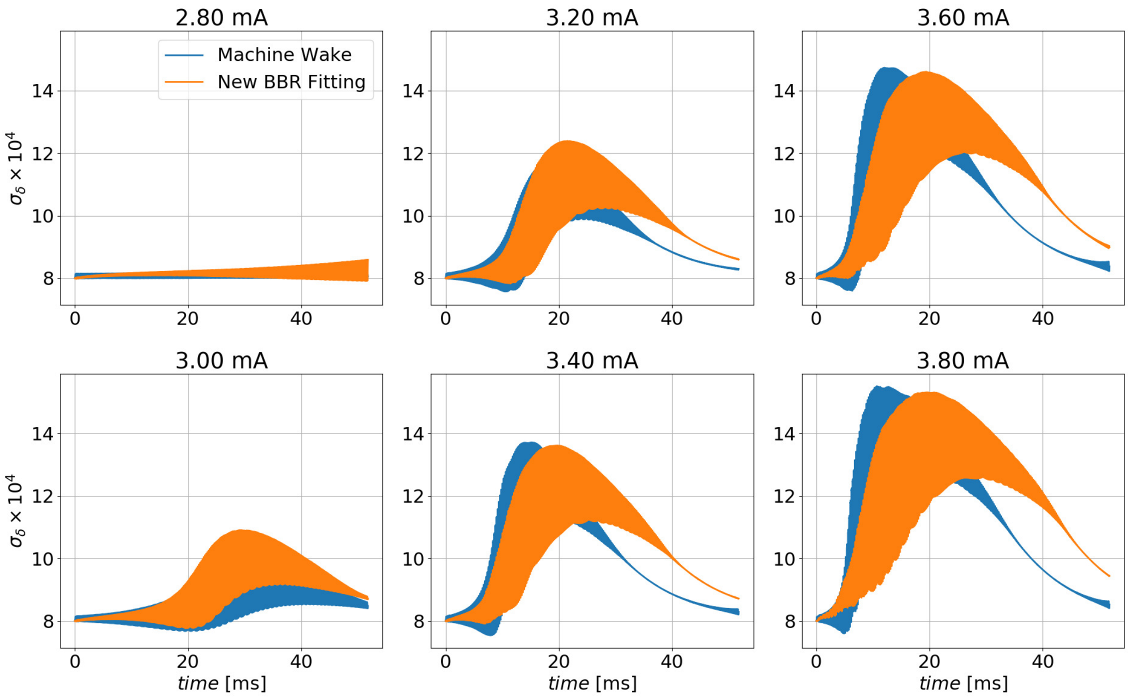

Figure 34 – Time evolution of the energy spread in tracking simulations for different currents above the threshold of the microwave instability, showing one cycle of instability growth, saturation and damping. This sawtooth–like behavior continues indefinitely and seriously compromises the quality of the radiation emitted. Note the good agreement between the behavior predicted by the BBR model and the detailed computed wake of the machine. It is interesting that the BBR have higher growth rates at lower currents, 2.8 and 3.0 mA, but for higher currents the other model predict faster growths. Such behavior should be investigated further.

the energy spread of the beam by

$$\Delta\sigma^2 = \sigma_\delta^2 - \sigma_{\delta 0}^2 \approx \frac{\mathrm{var}(K)/E_0^2}{\alpha_z T_0(2-\alpha_z T_0)} = \left(\frac{qI_bT_0W}{E_0}\right)^2 \frac{\Delta z_W}{\sqrt{2\pi e}N_p}\frac{1}{\alpha_z T_0(2-\alpha_z T_0)}. \tag{I.8}$$

Figure 37 shows the energy spread variation from Sirius tracking simulations multiplied by $N_p\sigma_s/I_b^2$. Note that according to Eq. (I.8) this quantity should depend only on the storage ring properties and on the wake characteristics, $(W, \Delta z_W)$, and, therefore should be an horizontal straigth line. Note that this is the behavior for the 100 k and 1 M particles curve and that the 10 M curve deviates from this behavior above 2 mA, but approaches the same baseline of the others for lower currents. This deviation is understood when the simulation with 50 M particles is analysed, where the real microwave instability dominates the scaling. Other two simulations with 1 M particles are also shown, one without the high frequency resonator, where we note the real instability also happens, with approximately the same characteristics of the 50 M particles curve, and another with a filtered wake. This filter consists in convolving the total wake function with a small gaussian bunch ($\sigma_z = 40\mu$m) and using this effective wake as input for the simulation, this approach changes the short range wake by filtering out high frequencies of the impedance spectrum. Even though this filtered model has a smaller baseline than the other curves,

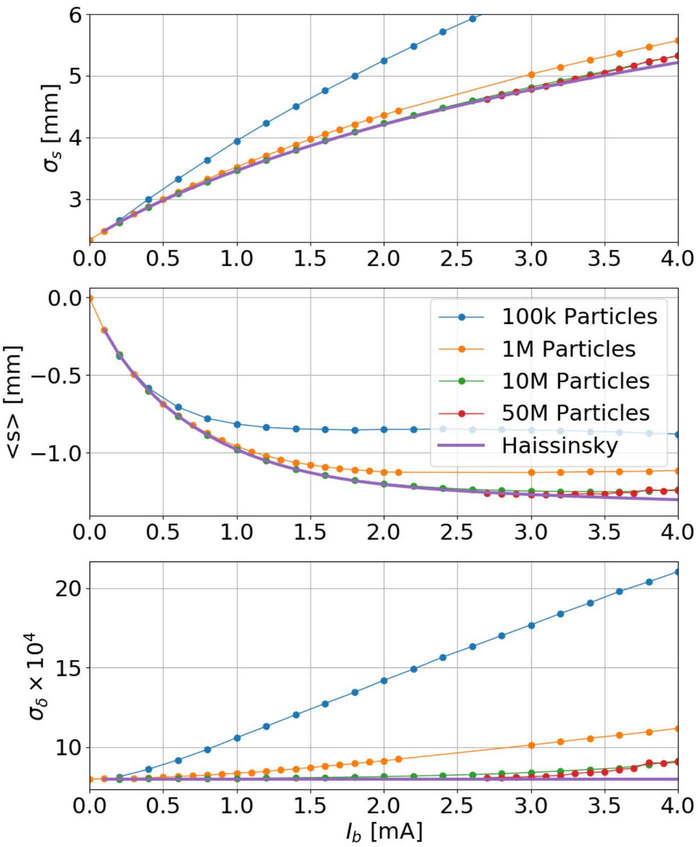

Figure 35 – Tracking results, showing the effect of noise as a function of the number of macroparticles used in the simulation.

it was not enough to predict the instability at ≈2.5 mA, due to the additional energy spread introduced by the noise, like the unfiltered simulations with 100 k and 1 M particles. While Fig. 37 shows that Eq. (I.8) qualitatively explains the energy spread increase induced by noise in simulations, Fig. 38 shows that, even though several approximations were performed in its deduction, it can be used to quantitatively estimate the number of particles needed to avoid such problems.

Even though all the simulations presented here were performed with the General Wakes mode of the tracking code, which uses the PIC method, the same results were also observed for tracking the pure Resonators. This indicates that the effect described above is not related to the PIC method, but is a limitation of the physical system used to replace the real one in the simulations. The reduced number of particles increase the fluctuations that already exist in the real beam and, as Eq. (I.8) suggests, would also induce energy spread increase in the physical system if the wake were ≈100 times stronger.

I.5 Conclusions

In this work it was shown that the longitudinal broad band resonator model explains well the behavior of the bunch in terms of energy loss, bunch–lengthening and time evolution above the microwave instability threshold, that is predicted to be approximately 2.7 mA for Sirius. Also, the difficult task of simulating very high frequency wakes

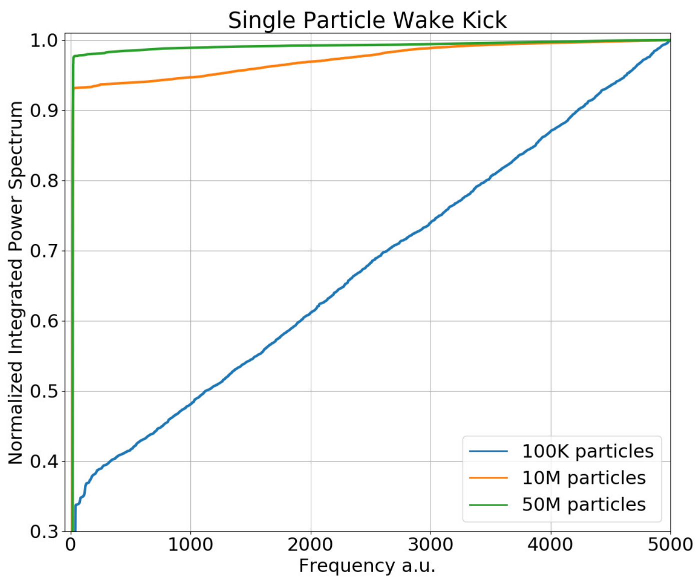

Figure 36 – During tracking simulations one particle is followed and its position in phase space and kick received by the wake are stored for each turn. The figure above shows the integrated power spectrum of the kick as a function of the frequency for simulations with 4 mA in the bunch. As the number of particles simulated increase, the energy is concentrated in the synchrotron frequency.

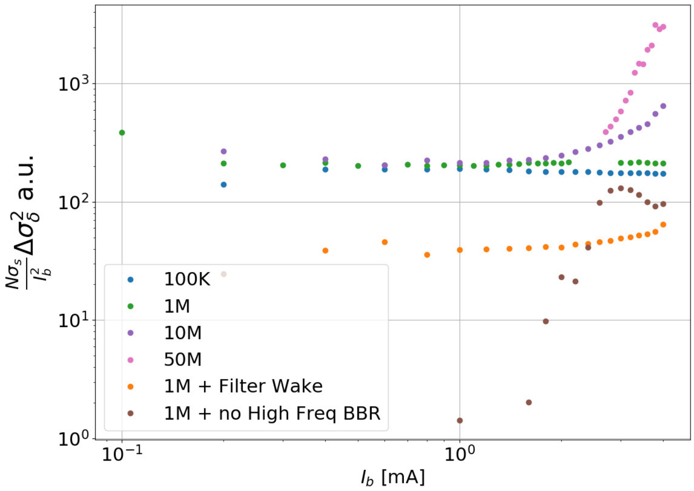

Figure 37 – Energy spread increase in simulations multiplied by $N_p\sigma_s/I_b^2$. The curves 100 k, 1 M, 10 M and 50 M were performed with the same wake function, while for curve 1 M + Filter Wake a convolution with a 40μm gaussian bunch was applied to the wake and for the other curve, the resonator with highest frequency presented in Tab. 7 was not used. Note how the baselines change depending of the wake function used.

was analyzed and a simple theory to explain the noise it introduce in the results were developed. Such a theory proved to be helpfull in estimating the tracking parameters for the simulations. In the next step of the work, the CSR wake will be introduced in the impedance model and the tracking simulations will be extended to the transverse planes.

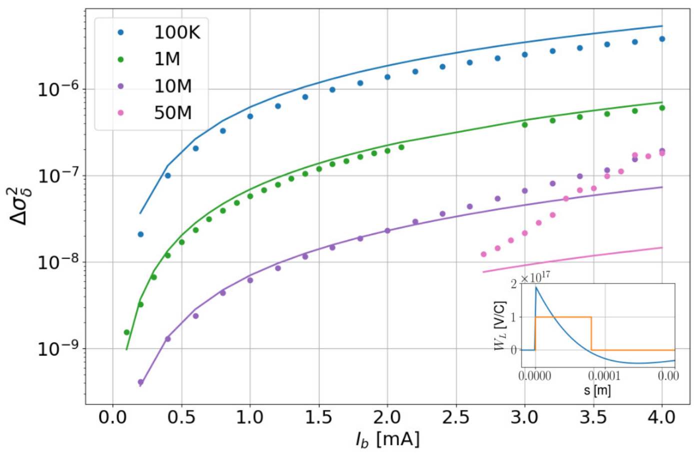

Figure 38 – Dots represents the energy spread increase in simulations with the same wake function (represented by the blue curve in the small graphic) and lines are the prediction of Eq. (I.8) using a constant model for the wake (orange line in the small graphic), with $W = 1 \times 10^7$V/C and $\Delta z_W = 80\mu$m.

Annex

ANNEX A – ANEXO 1

Sed mattis, erat sit amet gravida malesuada, elit augue egestas diam, tempus scelerisque nunc nisl vitae libero. Sed consequat feugiat massa. Nunc porta, eros in eleifend varius, erat leo rutrum dui, non convallis lectus orci ut nibh. Sed lorem massa, nonummy quis, egestas id, condimentum at, nisl. Maecenas at nibh. Aliquam et augue at nunc pellentesque ullamcorper. Duis nisl nibh, laoreet suscipit, convallis ut, rutrum id, enim. Phasellus odio. Nulla nulla elit, molestie non, scelerisque at, vestibulum eu, nulla. Ut odio nisl, facilisis id, mollis et, scelerisque nec, enim. Aenean sem leo, pellentesque sit amet, scelerisque sit amet, vehicula pellentesque, sapien.

ANNEX B – ANEXO 2

Sed consequat tellus et tortor. Ut tempor laoreet quam. Nullam id wisi a libero tristique semper. Nullam nisl massa, rutrum ut, egestas semper, mollis id, leo. Nulla ac massa eu risus blandit mattis. Mauris ut nunc. In hac habitasse platea dictumst. Aliquam eget tortor. Quisque dapibus pede in erat. Nunc enim. In dui nulla, commodo at, consectetuer nec, malesuada nec, elit. Aliquam ornare tellus eu urna. Sed nec metus. Cum sociis natoque penatibus et magnis dis parturient montes, nascetur ridiculus mus. Pellentesque habitant morbi tristique senectus et netus et malesuada fames ac turpis egestas.

ANNEX C – ANEXO 3

Phasellus id magna. Duis malesuada interdum arcu. Integer metus. Morbi pulvinar pellentesque mi. Suspendisse sed est eu magna molestie egestas. Quisque mi lorem, pulvinar eget, egestas quis, luctus at, ante. Proin auctor vehicula purus. Fusce ac nisl aliquam ante hendrerit pellentesque. Class aptent taciti sociosqu ad litora torquent per conubia nostra, per inceptos hymenaeos. Morbi wisi. Etiam arcu mauris, facilisis sed, eleifend non, nonummy ut, pede. Cras ut lacus tempor metus mollis placerat. Vivamus eu tortor vel metus interdum malesuada.